Mathematical Modelling of Wave-Structure Interactions with application to Wave Energy Conversion

by

Federica Buriani

A Doctoral Thesis

Submitted in partial fulfilment
of the requirements for the award of

Doctor of Philosophy
of
Loughborough University

9th June 2019

Summary

Energy conversion from ocean waves is one of the core themes of the energy global challenge research for the sustainability of the planet. New trends of wave energy technologies attempt to explore new paths and intend to bring new answers to the problem of the competitiveness of the produced energy for conventional devices. This thesis provides the reader with mathematical models of wave-structure interactions applied to novel concepts of wave energy converters: a flexible piezoelectric wave energy harvester and a floater blanket wave energy converter. In chapter 1 I present an overview of the field of wave energy, a brief history and descriptions of working principles and technologies of wave energy conversion along with a number of classification schemes. Classical systems as well as new trends in the form of flexible or deformable converters and hybrid systems are presented. In chapter 2 I define the hydrodynamic problem which provides the basis of the linearised wave theory used to derive the mathematical models in this thesis. In chapter 3 I apply the theory of elastic plates to develop a distributed-parameter model for bimorph piezoelectric plates which yields electro-mechanical equations for a piezoelectric wave energy converter. Then, the electro-mechanical problem will be coupled to the hydrodynamic problem in chapter 4, in which we also present numerical results of the power output of two possible real configurations of piezoelectric wave energy converters. In chapter 5 I investigate the radiation properties of a novel floater blanket wave energy converter whose numerical analysis is presented in chapter 6. Finally concluding remarks and future research directions are presented in chapter 7.

Acknowledgements

Above all, I would like to express my deepest gratitude to my supervisor, Emiliano Renzi, for his guidance, support and patience throughout these three years. I would like to thank the Department of Mathematical Sciences of Loughborough University for the financial support during my studies, but also all the academic and administrative staff of the department, for creating an ideal, friendly and well-organised environment for postgraduate studies. Thanks to Loughborough, to its beautiful and technical paths from The Outwoods to Bradgate Park, throughout Jubilee Wood, Buck Hill, Beacon Hill, Broombrigss Farm & Windmill Hill, Woodhouse Eaves, Swithland Wood and every hill in Charnwood forest, where I have been running for three years. For the first few months my runs were almost entirely about exploration. Every time I stepped outside to run, the sense of embracing the unknown returned. The flavour of the air was unfamiliar, the light was unfamiliar, the temperature was unfamiliar, the texture of the earth was unfamiliar. Above all, the context was new. But the thrill of discovering proved a great motivation, day by day and now, all this, became an important part of my life and this collection of running adventures is so large that I could write a book about them! Many thanks to all the amazing sports facilities around the University campus, to the boot-camp course and the squash league. To all the adventures and explorations which made special my UK life experience. Thanks to the LSU hiking club for the great moments we shared together. Thanks to Karl & Diane and all the international friends that have been part of this beautiful journey. Finally, words are not enough to express how grateful I am to my family; my parents, Franco and Luciana, for their patience, their support, their love, my brother Giacomo, my granny Mariannina and Francesco, 'mi punto fijo aunque cuando todo mi mundo cambia' since 2008.

Contents

List of Figures

List of Tables

Chapter 1

Introduction

Renewable energy sources, such as hydro, wind, solar, biomass and ocean energy forms such as wave, tidal, currents, thermal and salinity driven systems can help to overcome environmental issues, depletion of fossil fuels, security of supply and job creation [35]. The environmental issues relate to local effects such as pollution but also to global effects such as climate change, due to the production of CO_2, which is related to energy generation from fossil fuels [2]. The depletion of fossil fuels was already highlighted in publications in the 1950s [21] and it is well established that fossil fuels are finite and that the time horizon before they are depleted are counted in 10'ths, maybe 100'ths, of years. Thus, it is also obvious that the current level of energy consumption, which is mainly based on fossil fuels, cannot continue unless alternative sources are developed. And here the renewable energy sources are the most obvious answers, as these resources are regenerative and do not deplete over time [28]. But even if reasonable amounts of fossil fuels are currently available, the uneven distribution of the resource around the globe is giving rise to conflicts. It can only be expected that this tendency will be worsened as the fossil resources are getting more and more depleted. Thus, for most nations it is of great interest to decrease their dependency on fuel supply from other countries to maintain their sovereignty and political stability. As an answer to that, renewable energy sources are very diverse and to a much larger extent scattered and well distributed around the globe, when looking at the renewable energy resource as a whole. In the current market, energy from the less mature technologies utilising renewable energy sources is generally not cost competitive, but relies on political

support. However, it can be expected that this situation will turn in the near future due to both the expected (and experienced) increase in cost of fossil fuels and the reduction of cost of the technologies utilising renewable energy sources, due to further research, development and economics of scale [35]. Biomass, wind, solar, hydropower and geothermal are currently used at commercial scale around the world, while progress in the commercialisation of ocean energy is pretty slow because the technology for exploitation of ocean energy sources is still mostly under development and there are a number of challenges standing between the sector's current status and the aim of commercial utilisation [15].

Nevertheless, there is a great potential of renewable energy that is stored in oceans. In fact, oceans cover more than 70% of Earth's surface and act as the largest solar collectors capturing thermal energy from the sun. In addition, the gravitational pull of the moon drives tides and winds generate ocean waves. Ocean energy sources have a number of important advantages that include abundance, availability, high load factor, low environmental impact and source predictability [15], therefore it has the potential to play a significant role in the future world energy system. In Europe, under the right conditions for both technological development and project deployment, 100 GW of ocean energy capacity could be installed by 2050, feeding around 350 TWh of power to the grid. The potential contribution of ocean energy is estimated to be of around 10% of EU power demand by 2050, [18].

Continuous waves contain huge energy potential [28]. The wind blowing over the surface of the ocean creates waves, which can travel thousands of miles with virtually no loss of energy. A wave carries both kinetic and gravitational potential energy. The total energy of a wave depends roughly on two factors: its height and its period. The power carried by a wave is proportional to the square of its height and to its period and is usually given in Watt per metre of incident wave front [14, 28]. Fig. 1.1 by Gunn & Stock-Williams, shows a world map of wave energy resource with an average order of magnitude of few tens of kW/m which is mainly located in the north of the northern hemisphere and in the south of the southern hemisphere. The global ocean wave energy resource may be evaluated by integrating the mean wave power on all coasts of the world. Thus, in [19], it

is estimated at 18500 TWh per year, or a mean power of about 2.1 TW = 2,100 GW, [6]. This could cover only a fraction of the world's energy needs, therefore ocean wave energy cannot be a single solution to the global challenge of energy source decarbonisation. Nevertheless, for certain coastal territories, it can appear as a very significant resource, [6].

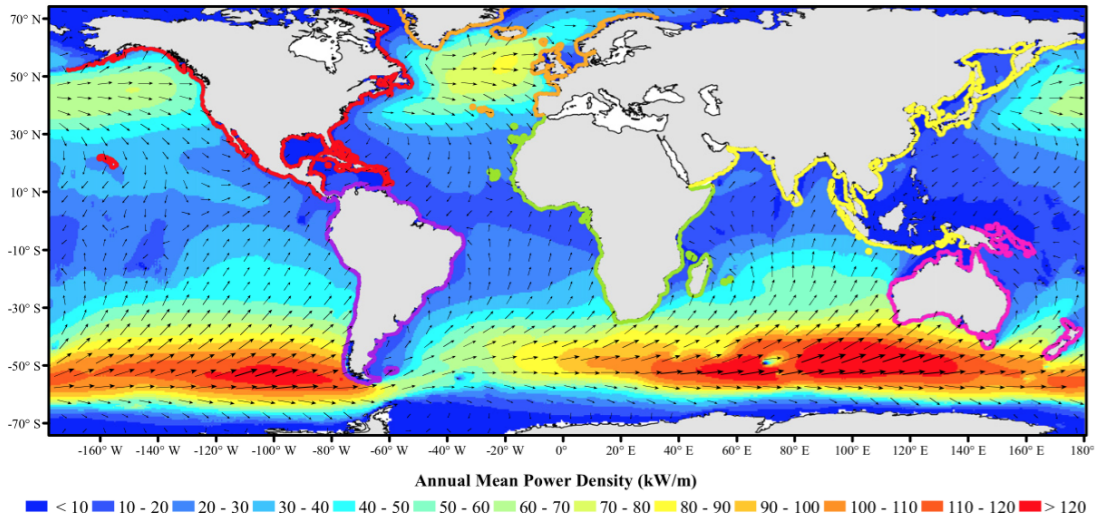

Figure 1.1: Map of worldwide wave resource. The figure is taken from [19].

1.1 Ocean wave energy: brief history

The history of wave energy is rich and diverse. The oldest patent for a wave energy converter (WEC) dates back to the year 1799 and describes the working principle to extract wave energy from wave-activated bodies [6]. History does not say if a device was built, anyway first recorded attempts to develop wave energy harvesters took place in the 1800s, when, in California, the Wave-Power Air-Compressing Company was created to commercialise a *Wave motor*. The device consisted of an oscillating water column which allowed sea water to be pumped and then used to moisten roads in order to avoid dust clouds, see Fig. 1.2 [6, 35]. Another example of early prototypes to harvest wave energy, is the hydraulic ram developed by Coyne in France, in 1926. The device was destroyed by a storm.

Figure 1.2: Postcard of the Armstrong brothers' Wave motor. It functioned from 1898 to 1910 in Santa Cruz, CA. [35].

By the end of the 1950s, all the main principles of wave energy conversion (overtopping devices, oscillating water columns, heaving buoys and OWSCs) had already been identified [6]. Different solutions were proposed and improved year by year but none of them seemed likely to be the basis for a valid industrial system, according to economic studies of the devices. For example, a summary of studies carried out on an overtopping device yielded the conclusion that the price of energy was 10 times greater than other energy sources at the time [6]. However, despite the interest in the field was not continuous over time, a large number of wave energy converters have been deployed and tested over significant periods of time, electric energy has been produced and a great number of activities were carried out in a number of countries around the world, with most efforts seen in the coastal European countries. Among them, over the past decade the UK has put enormous efforts into the development of marine renewable energies, including wave energy, and must today be seen as the world leader in the field [35].

In the next section, we describe some of the most popular wave energy devices. The technical descriptions are based on reference [6].

1.2 Categorisation of wave energy converters

There is a large number of different ideas and concepts for how to utilise the wave energy resource. However, wave technologies can be classified into a limited number of families. In literature there are three different ways of WEC's categorisations: distance to the coast (Fig. 1.3), ratio between their general dimensions and the wavelength of waves as well as on the relationship between their orientation and the direction of propagation (Fig. 1.4), working principles (Fig. 1.5).

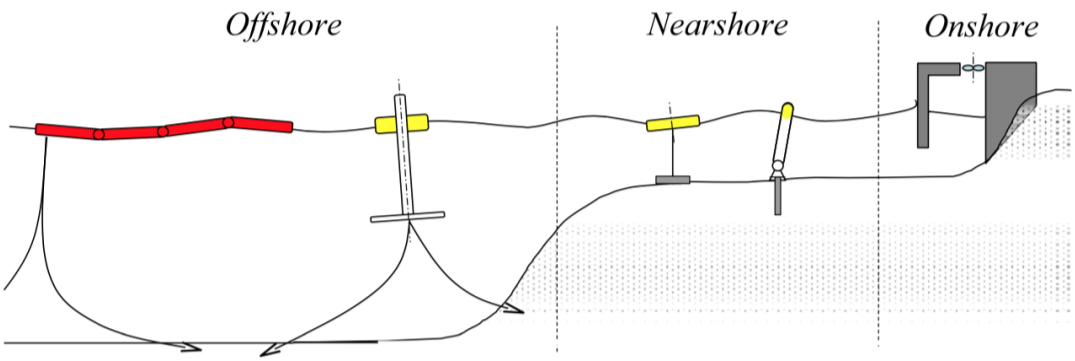

Figure 1.3: Classification of wave energy converters with regard to the distance to the coast [6].

Fig. 1.3 shows a classification of WEC's according to their location - *onshore*, *nearshore* and *offshore*. Onshore devices are rigidly installed on the coast such as oscillating water columns and overtopping devices, see further explanation below. Near shore devices are situated at water depths where the available waves are influenced by the water depth, and most often their working principle exploits the seabed as a fixed point. And thus, at last, offshore WECs will generally be floating and can operate in very deep waters (even more than 100 m) [6, 35].

WECs can also be categorised using the terms *terminator* when considering systems facing waves and with dimensions greater than or equal to the order of magnitude of the wavelength; *attenuator* which have large horizontal extensions orthogonal to the direction of wave propagation; finally, when the device is small compared to the waves, it is known as a *point absorber* [14], see again Fig. 1.4.

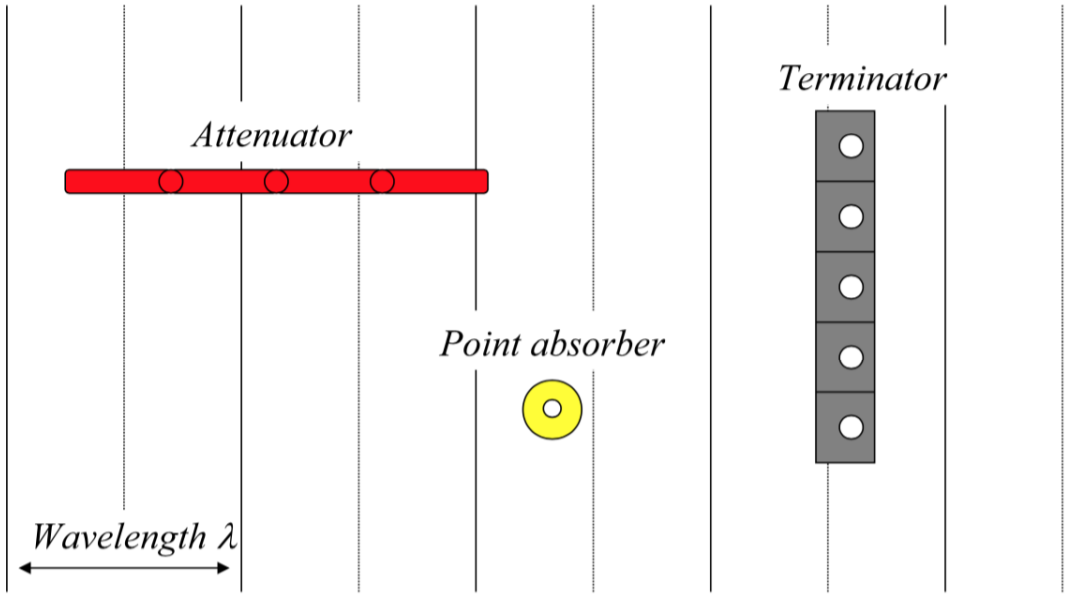

Figure 1.4: Schematic showing scale and orientation of a *terminator*, *attenuator* and *point absorber* [6].

A third classification of wave energy devices is based on their working principles. Within this approach, WECs are grouped into three main families: *oscillating water columns (OWCs), wave-activated bodies (WAB) and overtopping devices (ODs)* as shown in Fig 1.5. Below we explain the different working principles with some examples of the main devices. Let us start with the oscillating water column wave energy converter. It consists mainly of a chamber partially filled with water and presenting an internal water surface. This chamber communicates both with the ocean, through a submarine opening, and with the outside air, through a opening in the upper part where an air turbine is placed. When waves enter the chamber, they raise the average water level. The air in the upper part of the cavity is compressed and then escapes through the orifice. When waves recede, the average level in the chamber decreases. This creates a depression in the upper part of the chamber, so that the external air is sucked inwards. The inner free surface therefore behaves like a liquid piston, oscillating up and down, which gives the name to the device. At the orifice, an alternative air flow is converted into electricity through an air turbine [6, 35]. An example of an archetype of an oscillator water column is the *OWC Pico power plant* in the Azores (Fig. 1.6).

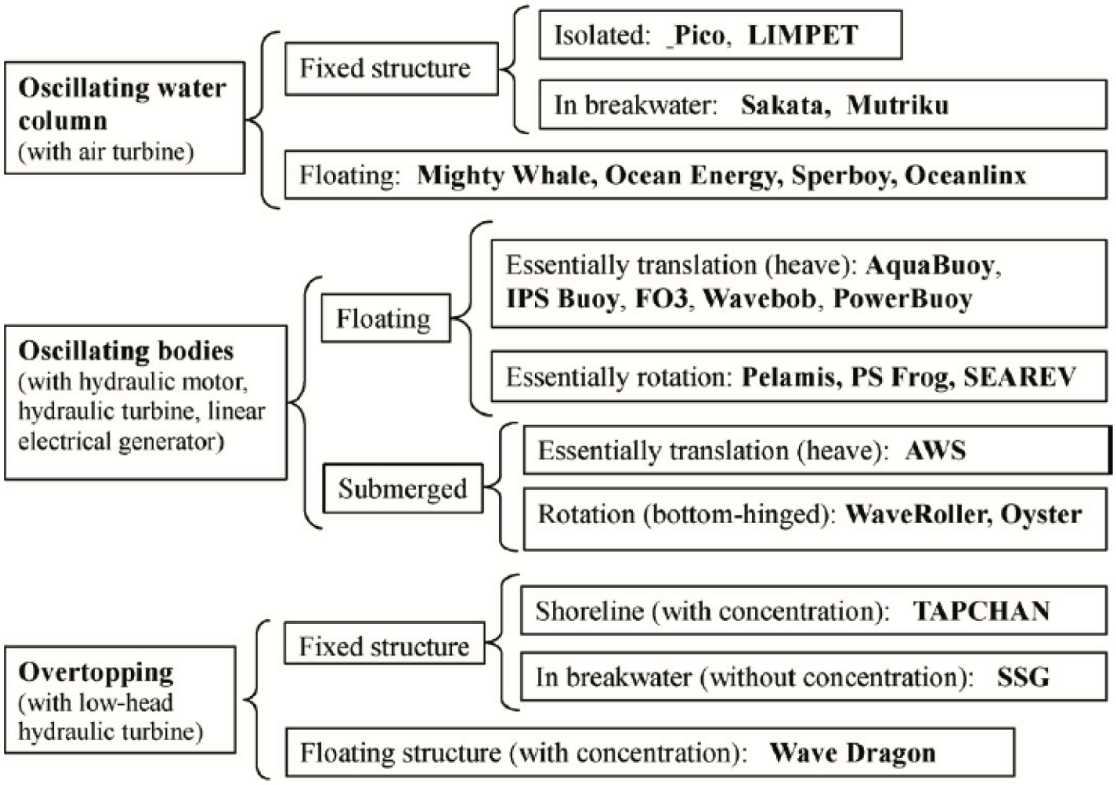

Figure 1.5: Classification of wave energy converters based on their working principle [6].

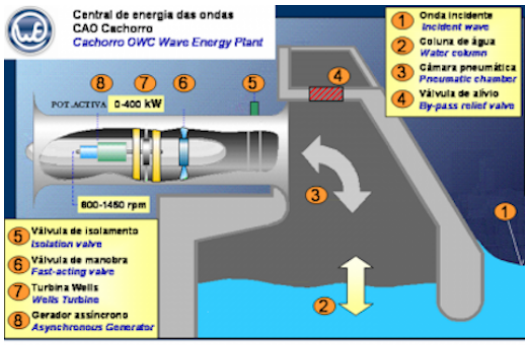

(a) Schematics and working principle.

(b) In action in a normal Autumn day.

Figure 1.6: The OWC Pico power plant [4], built in 1995 - 1998. The power plant worked for only a short period in October 1999, then was put on standby until 2004. From 2006 the Pico plant was used as a demonstrator and research pilot, with the objective of improving its reliability. In 2010, the plant produced 45 MWh for an operating time of approximately 1,400 h. In 2016, it produced 39 MWh. Nowadays its structure has become weakened and the decision has been made to decommission it [6].

Overtopping devices work exploiting the runup generated from breaking waves

to fill a reservoir located above the sea level. Kinetic wave energy is thus converted into gravity potential energy. The difference in water level between the tank and the average sea level is transformed into electrical energy by means of low-head turbines. The *Wave Dragon* is an archetype of a slack moored WEC which utilises the overtopping principle. The structure consists of a floating platform with an integrated reservoir and a ramp (Fig. 1.7). The waves overtop the ramp and fill the reservoir where the water is temporarily stored before it is led back to the sea via hydro turbines generating power to the grid. Other overtopping devices may be fixed to the sea bed acting as a combination of a WEC and a breakwater, as the *Sea Slot-cone Generator (SSG)* (Fig. 1.8). The latter consists of several reservoirs placed on top of each other above the mean water level in which the water of incoming waves is stored temporary.

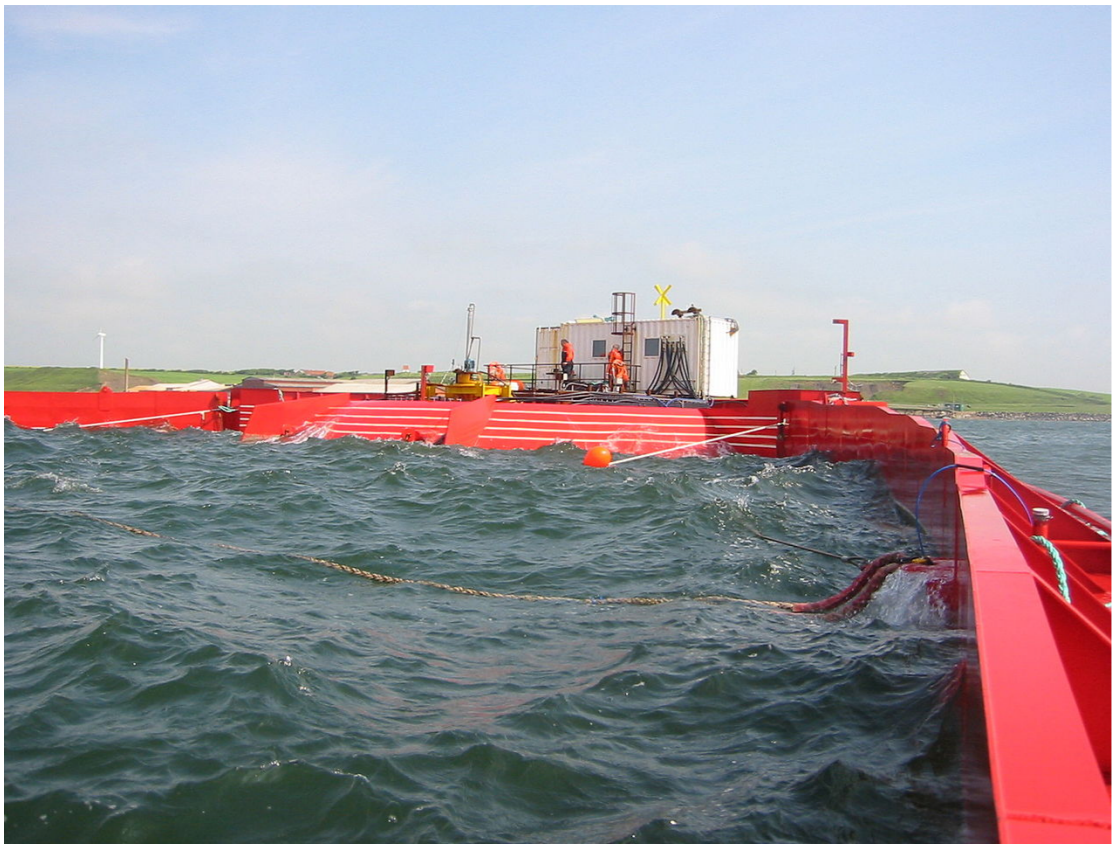

Figure 1.7: The 1:4.5 scale Wave Dragon prototype that was deployed in Denmark. Two large curved reflectors intend to focus waves into a narrowing channel to increase wave heights and thus overtopping volume. The width of the prototype was 57 m. At full scale, the size of the machine was thus 300 m for a total displacement of 33,000 tons [35].

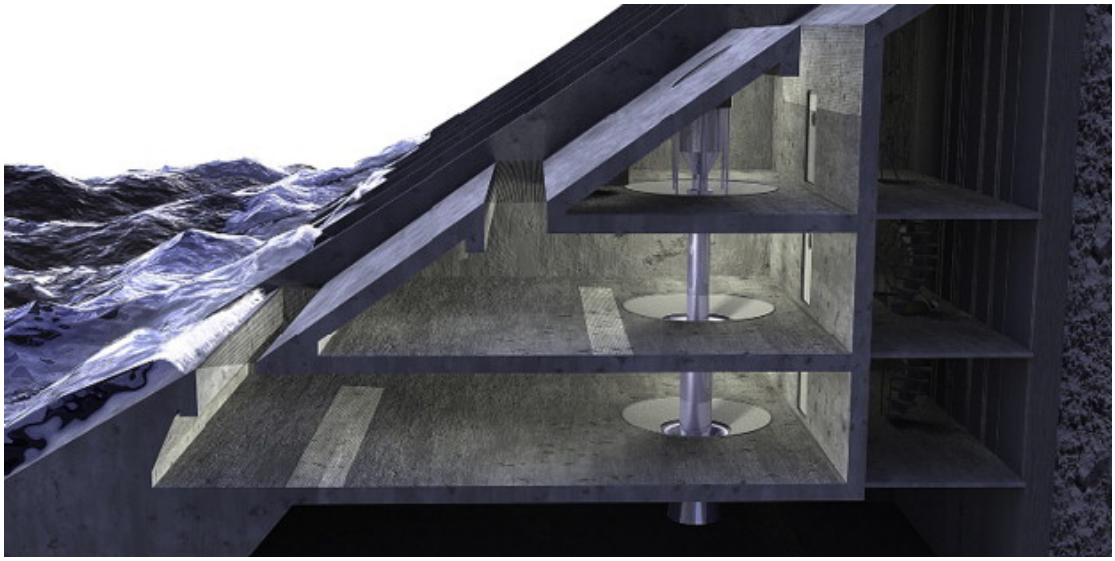

Figure 1.8: Lateral section of a three-levels SSG device with multi-stage turbine [26].

Wave-activated bodies represent a very large family of WECs. However, all of them are characterised by the same basic working principle: one or more floats are set in motion by waves. The relative motion between the floats and the sea bed (bottom-fixed wave energy converters), or between the floats themselves (self-referenced wave energy converters), is transformed into electrical power by a conversion system. This system is referred to as *power take-off (PTO)* [6]. In the framework of this thesis, we give just a number of examples to distinguish between wave energy converters using the heaving buoy principle and those using the oscillating wave surge converter (OWSC) principle.

1.2.1 Wave energy converters primarily based on vertical motion (*heave*)

In the context of naval architecture, the vertical motion is called *heave*. A heaving buoy is usually symmetric about a vertical axis. It floats on the surface of the water and is connected to a fixed mooring point at the bottom of the sea with a cable. The conversion system that transforms the kinetic energy of the buoy into electrical energy (i.e. the power take-off) is placed between the cable and the mooring system, or between the cable and the buoy. The power take-off is often a direct-drive linear electrical generator. For example, this is the case of the *Seabased* wave energy converter (Fig. 1.9) of which several prototypes are being

demonstrated in Sweden [6]. Alternatively, the power take-off can be in the form of a hydraulic cylinder. This is the solution that was chosen for the *CETO* wave energy converter (Fig. 1.10), of which three 240-kW prototypes have been tested in Australia. The CETO differs from the archetype of the heaving buoy due to the fact that the buoy is not floating but submerged.

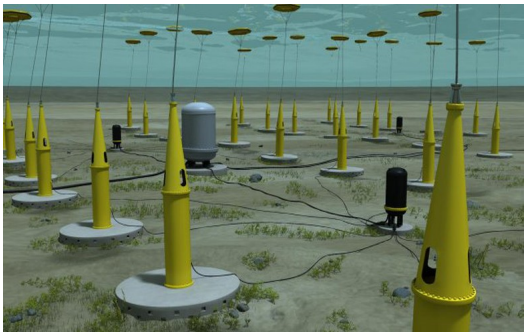

(a) Artist impression of the Seabased power plant [5].

(b) Seabased at the Maren test site off the Island of Runde, Norway.

Figure 1.9: Seabased wave energy converter developed in Sweden since 2002. Its working principle is based on vertical motion (heave) and it installed in shallow waters. The diameter of the buoys is of the order of 5 m [5, 6].

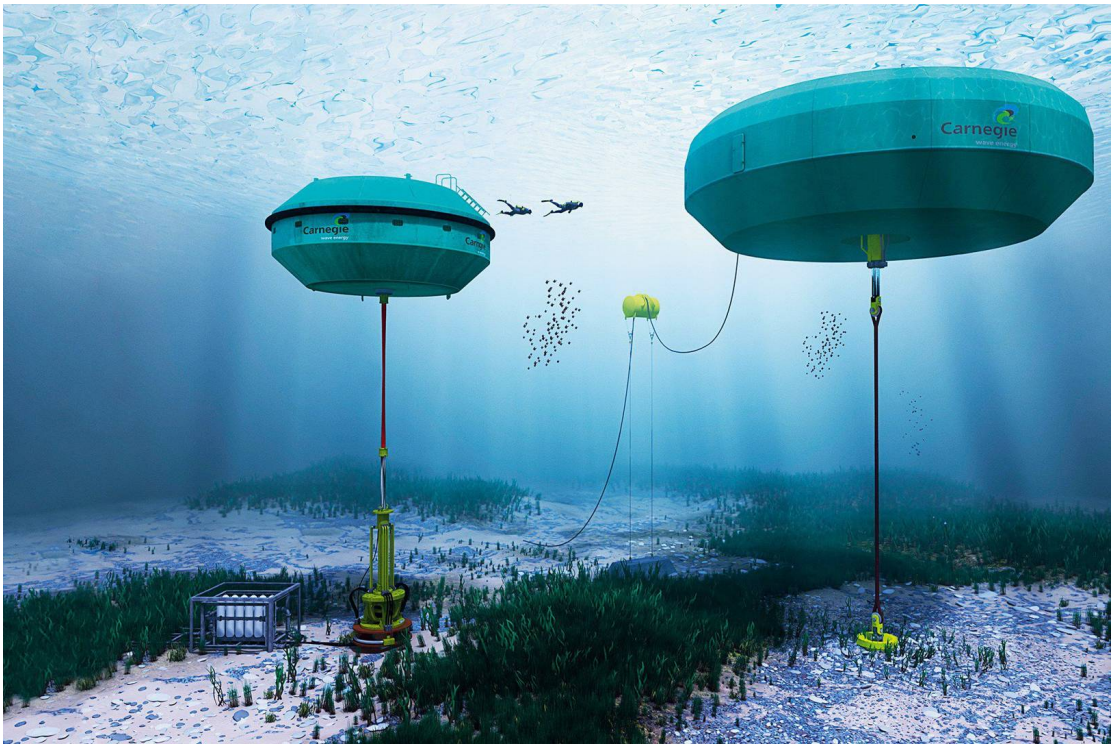

Figure 1.10: Carnegie's CETO. A submerged tether moored point absorber [1].

Figure 1.11: The prototype of the PB40 converter by Ocean Power Technologies in October 2010 in Hawaii [6].

Both CETO and Seabased WECs operate in shallow water therefore is economically feasible to use the seabed as a fixed point. To reduce manufacturing costs, in deep waters, wave energy converters must be self-referenced. The American *PowerBuoy* wave energy converters (Fig. 1.11), the Irish WEC *Wavebob* and the Spanish WEC *W1* are examples of self-referenced heaving buoys. Still in deep water, articulated-float wave energy converters, such as the *Cockerell Raft* or the *SeaPower Platform* technologies (Fig. 1.12), could be classified into the category of arrays of heaving buoys [6]. In fact, despite in most scenarios the motions that are exploited are often relative rotation motions and the geometrical configuration significantly differs from the archetype of the heaving buoy, these wave energy converters essentially consist of large-sized horizontal floats exposed to vertical forces, thus the motion of the centre of gravity is, at first order, also vertical. However, there is still a significant difference between arrays of heaving buoys and heaving buoys. These latter are known as omnidirectional i.e. they are indifferent to the direction of the waves, while wave energy converters with articulated floats perform better when they are aligned with the direction of propagation of waves (unidirectional) [6].

Figure 1.12: The 1/4-scale SeaPower Platform prototype in Ireland [6].

Another well-known example of a wave energy converter similar in its working principle to an array of heaving buoys is the *Pelamis* (Fig. 1.13). It is a floating device, made up of five tube sections linked by universal joints which allow flexing

in two directions. The WEC floats semi-submerged on the surface of the water and inherently faces into the direction of the waves, kept in place by a mooring system. As waves pass down the length of the machine and the sections bend in the water, the movement is converted into electricity via hydraulic power take-off systems housed inside each joint of the machine tubes, and power is transmitted to shore using standard subsea cables and equipment [35].

Figure 1.13: The Pelamis P2 operating in Scotland in 2012 [6].

1.2.2 Wave energy converters primarily based on horizontal motion (*surge*)

Horizontal flow velocities associated with waves are of the same order as vertical velocities, or even greater in shallow waters. Therefore, it is possible to absorb wave energy exploiting a horizontal principle of operation. In the context of naval architecture, the horizontal motion is referred to as *surge*. Wave energy converters that are part of this family operate based on the OWSC principle. They can be either fixed or floating depending on whether they are mounted on a fixed or floating reference as explained below. A famous example illustrating this principle was the *Oyster* wave energy converter developed by the company Aquamarine Power (Fig. 1.14). It is moored to the seafloor and has the form of a vertical flap. The wave action makes the flap oscillate back and forth (pitch). For all bottom-fixed wave energy converters, it should be noted that the variation of the mean water level due to tidal range can be disadvantageous for production. Designing a floating system is one way to avoid this difficulty. This is then referred to as floating OWSC. An example of this class of wave energy converters is the *Langlee* WEC. In the same family, we can include also *Salter's Duck*, *WEPTOS* WEC

(Fig. 1.15), *ISWEC*, *Azura wave* and others, which can be seen as variations on the principle of the OWSC making use of thick flaps or floats [6].

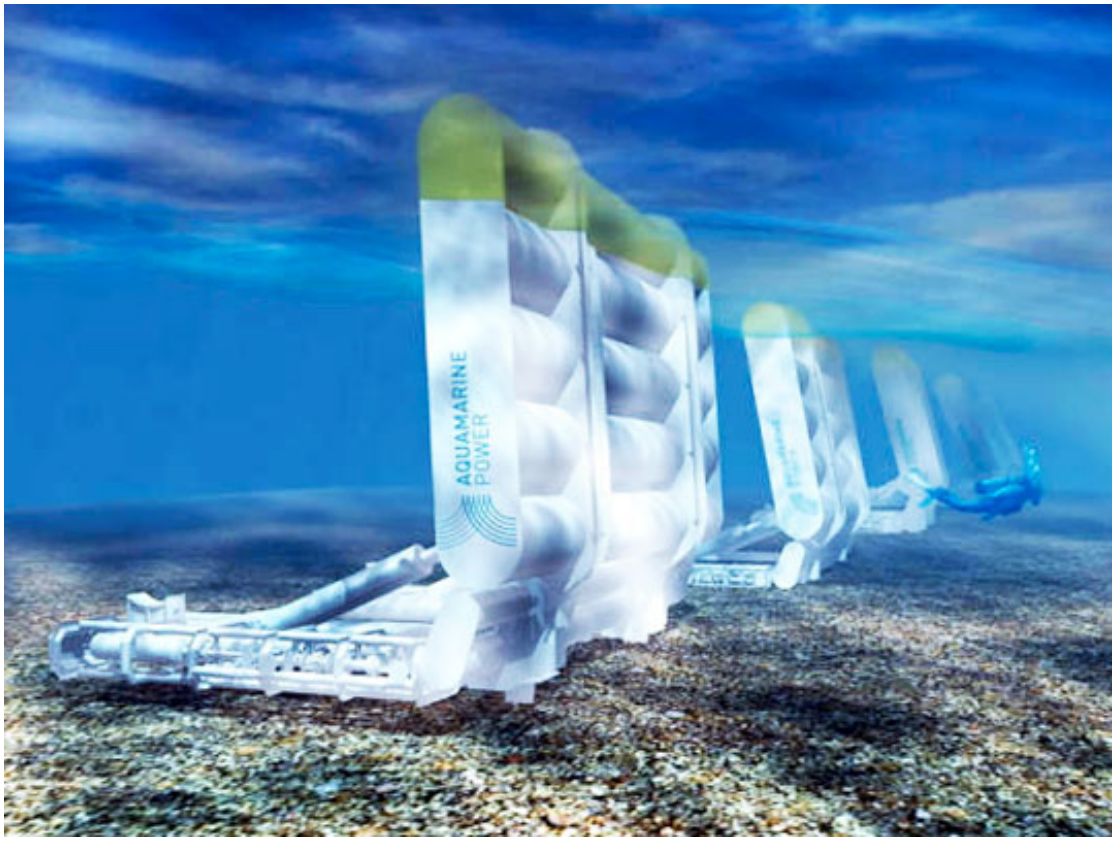

Figure 1.14: Artist view of an array of Aquamarine Power Oyster OWSC.

Figure 1.15: WEPTOS wave energy converter is made up of a structure consisting of two adjustable V-shaped arms. Wave energy absorbers of the Salter's Duck type are mounted on each arm [6].

1.3 Research gap

Wave energy converters implementing flexible or deformable structures and hybrid multi-energy or multipurpose systems seem to be part of a new trends in the ocean wave energy sector [6]. Innovative concepts intend to explore new paths in order to bring new answers to the issue of energy costs.

Flexible WECs employ materials or deformable structures instead of rigid bodies for wave energy harvesting. The concept has been already addressed in 2006 in the United Kingdom by Francis Farley who conceived the *Anaconda* which consists of a long elastic tube filled with water, submerged under the free surface and aligned in the direction of incoming waves. The waves, the elastic structure and the water inside the tube interact to create a bulge wave that propagates along the tube. The hydrodynamic performance of the Anaconda was probably something that prompted the developers of the *S3* WEC, whose main difference with the Anaconda was the power take-off system: instead of a turbine, for the S3, the energy conversion was made through rings of electro-active polymers (EAPs) evenly distributed along the tube. The S3 was, to our knowledge, the first wave energy converter to implement EAPs [6]. Other smart materials could be used for ocean engineering applications, among them we restrict our attention to piezoelectric materials which are still at a developing stage, see 1.4.1. In the view of the above, in the first part of this thesis, we propose a novel wave energy converter for low power applications making use of sleek design (i.e. flexible plate) and smart material (i.e. piezoelectric material).

On the other hand, at the beginning of this section, we mentioned hybrid multi-energy or multipurpose systems which can have a significant value with respect to the minimisation of usage conflicts and visual impact. In fact hybrid systems designate systems in which multiple functions are grouped on a single platform. The idea is that the pooling of functions makes it possible to divide the cost of the infrastructure [6]. Examples of hybrid systems involve combination of wind power and wave energy converters such as *P80 wind-wave energy converter* (Fig. 1.16), but also energy production through the harvesting of wave energy and the protection of the coastline or a harbour basin such as the *U-OWC (REWEC3)* breakwater designed in Italy, for the harbour of Civitavecchia.

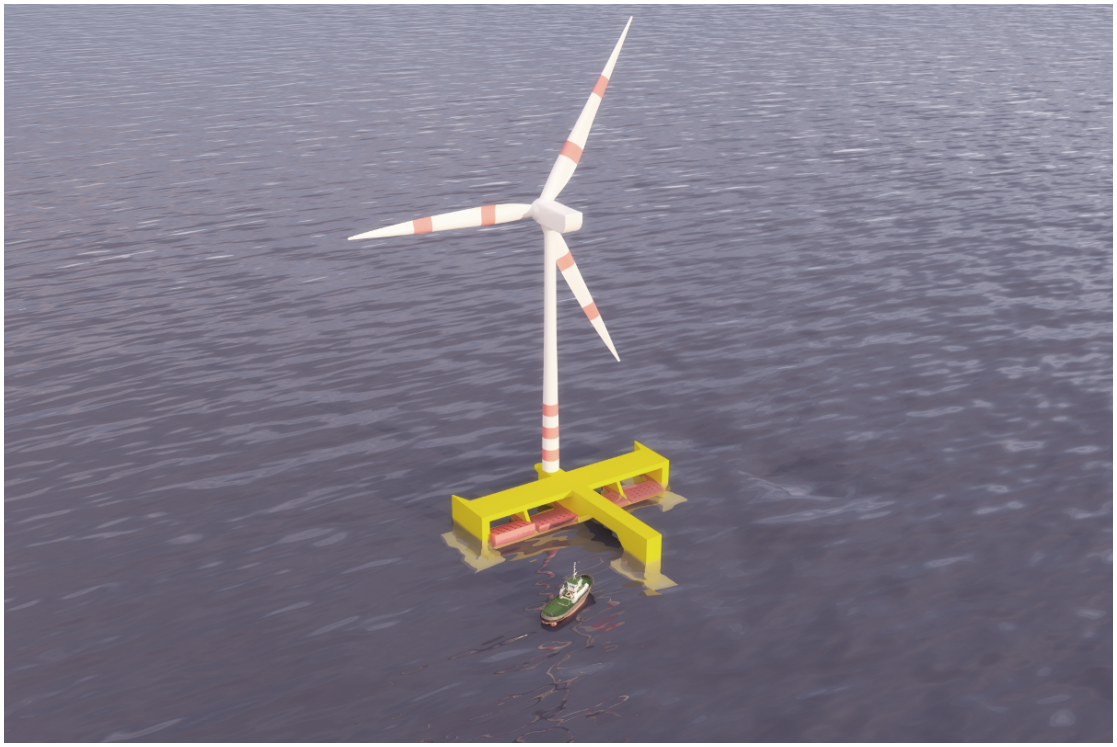

Figure 1.16: Artist view of the P80 wind-wave energy converter [6].

Considering the benefit that the ocean energy sector can get from the development of hybrid systems, in the second part of this thesis, we investigate the hydrodynamic behaviour of a *floater blanket wave energy converter (FBWEC)* which consists of a blanket made of a grid of interconnected floater elements. This device can be easily integrated in a multi-energy hybrid platform such as Ocean Grazer, a novel conceptual energy collection platform, projected to harvest renewable energy from sea waves combining wind, wave and energy storage on site, see 1.4.2.

1.4 In this thesis

1.4.1 Piezoelectric harvesters

Piezoelectric materials are attractive because of their ability to generate an electric potential when deformed due to vibrations (sensor effect). Conversely, they deform when subjected to an externally applied electric voltage (actuator effect) [32]. Since early 2000, an amount of energy generators and harvesters by using piezoelectric effects, such as piezoelectric coupled cantilevers, shells, cymbals and stacks,

with various designs of electrical circuits have been developed and many research works were conducted on optimising designs of piezoelectric coupled structures for more effective energy harvesting. These devices aimed to achieve practical portable micro-electromechanical systems via collecting energy of human activities, such as men's working and the bikes' motions. Recently, many research studies were conducted on piezoelectric energy harvesting from ambient vibrations by natural energies such as solar, wind, and ocean-wave energy [49].

Piezoelectric wave energy converters (PWECs) are an innovative concept of electromechanical ocean energy converters for low-power applications such as LEDs, wireless routers, PCs, ocean buoys and sensors. The working principle of a piezoelectric WEC is to harvest electrical energy from flexible deformations and vibrations induced by waves. Despite being less powerful than other WECs (the estimated power potential of a typical PWEC is in the order of watts to kilowatts [17, 40]), PWECs are environment-friendly, reliable, low-cost and have no limitation of shape and size. Therefore, they can also be buoy-mounted, employed to increase wave damping around offshore oil platforms and integrated into a system in combination with wind turbine farms and other wave energy harvesters. Also they have no moving parts, thus do not require frequent maintenance. Novel PWECs include cantilevered beams [17, 49, 50] and piezoelectric buoys [48], see Fig. 1.17.

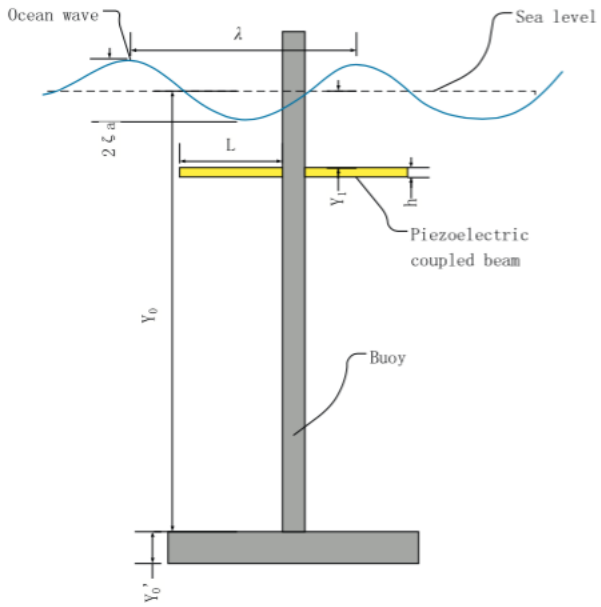

Figure 1.17: Energy harvesting buoy structure attached by piezoelectric coupled cantilevers floating on the ocean surface [48].

So far, such devices have been studied with rather simplified mathematical models, in which the effect of the piezoelectric layers on the dynamic response of the system was neglected. The bending force resulting from the action of the waves on the structure was plugged separately into the electric circuit equations to estimate the voltage on the piezoelectric layers. With that simplified approach, the hydro-electromechanical problem was in fact uncoupled into two separate wave-structure and electric problems. Such an approximate analysis is useful to obtain a preliminary estimate of the extracted power, but cannot be trusted to provide accurate results. Indeed, in reality the dynamics of waves, structural elasticity and piezoelectricity are inherently coupled in a PWEC, and so the development of a coupled hydro-electromechanical model is fundamental to provide an accurate analysis of the system [40]. In the framework of this thesis, our aim is to analyse mathematically a new fully coupled boundary-value problem based on the complex interactions between wave action, the flexible device and the piezoelectric effect. We consider possible practical configurations, such as a double-clamped plate, or a plate fixed at a vertical wall (e.g. a breakwater). These configurations reproduce possible real applications of piezoelectric WECs, where a superimposition of incident, radiated and reflected wave components interact dynamically with the

converter [51]. Results of this study have been published in a journal paper by Renzi [40] and in a conference paper by Buriani and Renzi [11].

1.4.2 Floater Blanket Wave Energy Converter

The University of Groningen is developing the Ocean Grazer, a novel ocean energy collection and storage device, designed to extract and store multiple forms of ocean energy. It is a massive platform housing various renewable energy generator modules including wave, wind and solar that will be deployed in deep ocean waters. Its core technology is a novel wave energy harvesting and storage device termed the multi-pump, multi-piston power take-off system. It comprises a grid of hinged floater elements (a floater blanket), with each floater being connected to a piston-type hydraulic pumping system (a multi-piston pump), see Fig 1.18. The Ocean Grazer structure itself will be made of concrete, protecting the system against ocean water and wind, while its massiveness will ensure stability even in the most extreme weather conditions. Similar to an iceberg, the core part of the Ocean Grazer structure will be situated well below the ocean surface such that the influence of ocean waves is minimised and the survivability of the structure is increased [3]. Loughborough University is now part of an international consortium that already includes Groningen University, Imperial College London and several industrial partners.

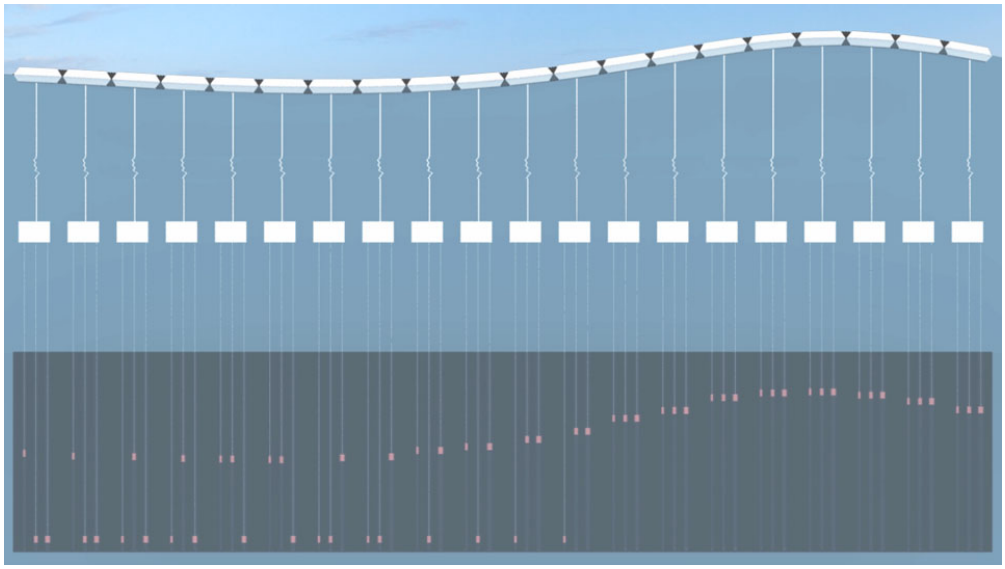

Figure 1.18: The grid of interconnected floater elements designed by the University of Groningen with each floater being connected to a multi-piston power take-off system [3].

Taking inspiration from the above concept, our aim is to develop a mathematical model of a floater blanket wave energy converter (FBWEC) which could be integrated by Ocean Grazer. In particular we want to analyse the wave-structure interaction problem for a specific configuration in which the blanket is floating on the ocean surface in correspondence of an ocean step.

1.4.3 Methodology

In this subsection we present a concise overview of the methodology that will be used to derive two separate mathematical models: the first is a coupled hydro-electromechanical model of a piezoelectric wave energy harvester, the second concerns a hydrodynamic analysis of a floater blanket wave energy converter.

PWEC

1. Derive a linearised potential-flow model for the ocean surface waves (chapter 2).

2. Derive a distributed-parameter model for the piezoelectric plate (chapter 3).

3. Develop a new fully coupled hydro-electromechanical boundary-value problem (chapter 4).

4. Solve the problem by using the method of matching potentials and appropriate conditions at the physical boundaries of the system (chapter 4).

5. Identify numerical solutions of the coupled system and determine all the quantities of engineering interest (spatial displacement of the flexible plate, spatial component of the free-surface elevation and average electric power in the output system per unit width) (chapter 4).

6. Compare the power generated by two practical configurations of PWECs, such as a doubled-clamped plate and a plate fixed at a breakwater (chapter 4).

FBWEC

Due to the complexity of the problem here we focus our analysis on the vertical radiation by one floater in a two-dimensional configuration.

1. Decompose the frequency-domain problem in the diffraction and radiation problems (chapter 5).

2. Derive and solve the radiation problem using the matching of potentials and a method based on the integral equations (chapter 5).

3. Derive expressions for all the amplitude coefficients and useful identities to build up a well-posed boundary-value radiation problem (chapter 5).

4. Identify an appropriate integral equation and apply a regularisation method, so that the equation can be solved adopting a Galerkin approach (chapter 5).

5. Implement a Matlab code to identify the behaviour of radiated-wave amplitudes when the body executes only one mode of oscillation (chapter 6).

6. Explore other mathematical approaches and physical considerations to describe the system (appendices B, D).

Chapter 2

Wave motion

This chapter is an introduction to the dynamics of ocean surface waves according to a linear theory, which will form the basis of the mathematical models developed in this thesis. We first derive the basic equations of fluid motion considering time scales such that compressibility, surface tension and earth rotation are of little importance. Notions of propagating waves are presented assuming the vertical stratification of sea water to be small enough with the depth of interest. The case of inviscid fluid and irrotational flow is considered. Finally, we solve a boundary-value problem of linearised equations considering the properties of simple harmonic progressive waves on constant depth. Letters in bold denote vectors. Variables with primes denote physical quantities.

2.1 Governing equations

The gravity-wave motion problem is adequately described by mass and momentum conservation laws and by appropriate boundary conditions.

The law of conservation of mass can be written as [10]

$$0 = \frac{\mathrm{d}M'}{\mathrm{d}t'} = \frac{\mathrm{d}}{\mathrm{d}t'} \iiint_{V'} \rho \, \mathrm{d}V', \tag{2.1}$$

where $M'(\mathbf{x}', t')$ is the fluid mass, $\rho(\mathbf{x}', t')$ the density, $V'(t')$ a material volume containing the same moving fluid particles (there are no mass sources or sinks) and $\mathbf{x}' = (x', y', z')$ with the z'-axis pointing vertically upward. Now, by using the kinematic transport theorem: $\frac{\mathrm{d}}{\mathrm{d}t'} \iiint_{V'} G' \, \mathrm{d}V' = \iiint_{V'} \frac{\partial G'}{\partial t'} \, \mathrm{d}V' + \iint_{S'} G' \mathbf{v}' \cdot$

$\mathbf{n}'\,\mathrm{d}S'$, where $G'(\mathbf{x}', t')$ is some fluid property per unit volume, $S'(t')$ is the surface which bounds $V'(t')$, $\mathbf{v}'(\mathbf{x}', t')$ is the velocity vector (u', v', w') and $\mathbf{n}'$ is the normal velocity of a point on S', we get

$$0 = \frac{\mathrm{d}}{\mathrm{d}t'} \iiint_{V'} \rho \,\mathrm{d}V' = \iiint_{V'} \frac{\partial \rho}{\partial t'} \,\mathrm{d}V' + \iint_{S'} \rho \mathbf{v}' \cdot \mathbf{n}' \,\mathrm{d}S' \\ = \iiint_{V'} \left(\frac{\partial \rho}{\partial t'} + \nabla \cdot (\rho \mathbf{v}') \right) \mathrm{d}V'. \tag{2.2}$$

In the latter identity we applied the divergence theorem. Because V' is arbitrary the integrand must vanish identically:

$$\frac{\partial \rho}{\partial t'} + \nabla \cdot (\rho \mathbf{v}') = 0. \tag{2.3}$$

This is the differential form of mass conservation law, valid at any point inside the fluid. As an alternate form we may write

$$\frac{\partial \rho}{\partial t'} + \mathbf{v}' \cdot \nabla \rho + \rho \nabla \cdot \mathbf{v}' = \frac{\mathrm{d}\rho}{\mathrm{d}t'} + \rho \nabla \cdot \mathbf{v}' = 0. \tag{2.4}$$

For the special case of an incompressible but non homogeneous fluid:

$$\frac{\mathrm{d}\rho}{\mathrm{d}t'} = \frac{\partial \rho}{\partial t'} + \mathbf{v}' \cdot \nabla \rho = 0. \tag{2.5}$$

It follows that

$$\nabla \cdot \mathbf{v}' = 0, \tag{2.6}$$

which is also known as the continuity equation. If the incompressible fluid is also homogeneous, then (2.6) holds and $\rho = \textit{constant}$ replaces (2.5). Also if we consider an inviscid irrotational flow, the velocity $\mathbf{v}'$ can be expressed as the gradient of a scalar potential Φ', i.e. $\mathbf{v}' = \nabla \Phi'$. Continuity equation (2.6) requires that the potential satisfies Laplace's equation

$$\nabla^2 \Phi' = 0. \tag{2.7}$$

The law of conservation of momentum can be written as

$$\frac{\mathrm{d}}{\mathrm{d}t'}\iiint_{V'}\rho\mathbf{v}'\,\mathrm{d}V' = \iiint_{V'}\rho\mathbf{f}'\,\mathrm{d}V' + \iint_{S'}\mathbf{t}'\,\mathrm{d}S', \tag{2.8}$$

where $\mathbf{f}'(\mathbf{x}', t')$ and $\mathbf{t}'(\mathbf{x}', \mathbf{n}', t')$ are respectively resulting volume and surface forces on the fluid. Physically, the preceding equation means that the time variation of momentum is caused by the resultant of all external forces (volume and surface forces) which act on the fluid volume. In particular, for gravity-wave problems, we assume $\mathbf{f}' = \mathbf{g}$, where $\mathbf{g}$ is the gravitational acceleration. Also let us consider the case in which (2.8) satisfies the constitutive relation for a newtonian fluid and Stokes's axioms [10], then we can rewrite (2.8) as the Navier-Stokes equation:

$$\left(\frac{\partial}{\partial t'} + \mathbf{v}'\cdot\nabla\right)\mathbf{v}' = -\nabla\left(\frac{P'}{\rho'} + gz'\right) + \nu'\nabla^2\mathbf{v}', \tag{2.9}$$

where $P'(\mathbf{x}', t')$ is the total pressure and ν' the constant kinematic viscosity. By using the vector identity $\mathbf{v}'\cdot\nabla\mathbf{v}' = \nabla\frac{\mathbf{v}'^2}{2} - \mathbf{v}'\times(\nabla\times\mathbf{v}')$, the irrotational condition ($\nabla\times\mathbf{v}' = 0$) and by assuming the fluid to be inviscid ($\nu' = 0$), the Navier-Stokes equation leads to

$$-\frac{P'}{\rho} = gz' + \frac{1}{2}|\nabla\Phi'|^2 + \frac{\partial\Phi'}{\partial t'} + C'(t), \tag{2.10}$$

where $C'(t)$ is an arbitrary function of t' and can usually be omitted by redefining Φ' without affecting the velocity field. Equation (2.10) is called the Bernoulli equation which can be used to find the pressure field, if the velocity potential is known. Physically, the total pressure P' is the sum of hydrostatic and hydrodynamic contributions expressed respectively by gz' and $\frac{1}{2}|\nabla\Phi'|^2 + \frac{\partial\Phi'}{\partial t'}$ on the right-hand side of (2.10).

2.2 Boundary conditions

In a wide variety of gravity-wave problems, two types of boundaries are of engineering interest: the water-air interface known also as the free surface and the wetted surface of an impenetrable stationary solid which can be for example the

sea bottom, see Fig. 2.1.

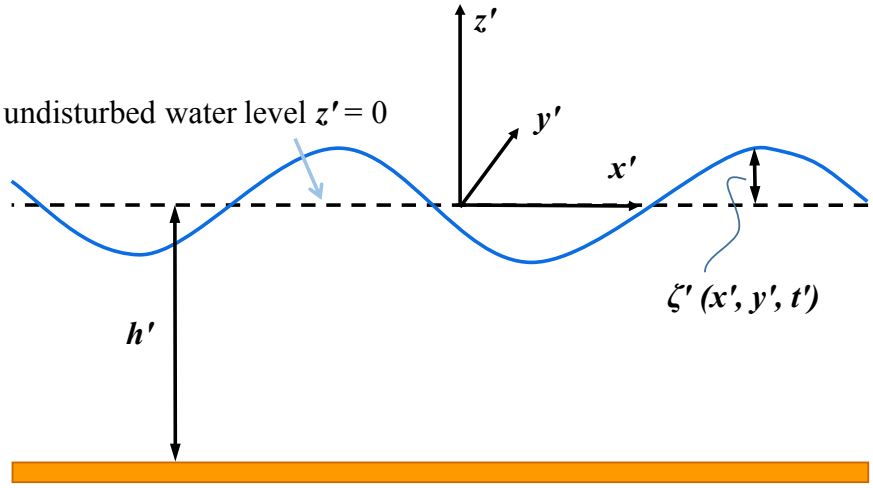

Figure 2.1: Geometry of the fluid domain.

The fluid is assumed to move only tangentially along these two boundaries [27]. Let the instantaneous equation of the boundary be

$$F'(\mathbf{x}', t') = z' - \zeta'(x', y', t') = 0, \tag{2.11}$$

where ζ' identifies the free surface, see again Fig. 2.1. and let the velocity of a geometrical point $\mathbf{x}'$ on it be $\mathbf{q}'$. After a short time dt', the free surface is described by

$$F'(\mathbf{x}' + \mathbf{q}'dt', t' + dt') = 0 = F'(\mathbf{x}', t') + \frac{\partial F'}{\partial t'} + \mathbf{q}' \cdot \nabla F' + O(dt'^2).$$

In view of equation (2.11) and neglecting second-order contributions,

$$\frac{\partial F'}{\partial t'} + \mathbf{q}' \cdot \nabla F' = 0.$$

The assumption of tangential motion requires $\mathbf{q}' \cdot \nabla F' = \mathbf{v}' \cdot \nabla F'$ which implies that

$$\frac{\partial F'}{\partial t'} + \mathbf{v}' \cdot \nabla F' = 0 \qquad \text{on} \qquad z' = \zeta', \tag{2.12}$$

or, equivalently,

$$\frac{\partial \zeta'}{\partial t'} + \frac{\partial \Phi'}{\partial x'}\frac{\partial \zeta'}{\partial x'} + \frac{\partial \Phi'}{\partial y'}\frac{\partial \zeta'}{\partial y'} - \frac{\partial \Phi'}{\partial z'} = 0 \qquad \text{on} \qquad z' = \zeta'. \tag{2.13}$$

Equation (2.12) or (2.13) is the *kinematic* boundary condition on the free surface. In the special case where the boundary is the sea bottom located at a depth $h'(x', y')$, we can consider it as a wetted surface of a stationary solid, therefore equation (2.11) becomes $z' + h'(x', y') = 0$ and $\frac{\partial h'}{\partial t'} = 0$. Then, the *kinematic* boundary condition on the sea bottom is

$$\frac{\partial \Phi'}{\partial n'} = 0 \qquad \text{on} \qquad z' = -h'. \tag{2.14}$$

Since both Φ' and ζ' are unknown, let us derive an additional boundary condition concerning forces. For the topics of interest of this thesis, the wavelength is so long that surface tension is unimportant [27]. If we apply (2.10) on the free surface, we have

$$-\frac{P'_a}{\rho} = g\zeta' + \frac{1}{2}|\nabla\Phi'|^2 + \frac{\partial \Phi'}{\partial t'} \qquad \text{on} \qquad z' = \zeta', \tag{2.15}$$

where we considered the pressure just beneath the free surface equal the atmospheric pressure P'_a above. Equation (2.15) represents a *dynamical* boundary condition on the free surface.

2.3 Linearised approximation for small-amplitude waves

Let us use physical scales of motion as in [27] to characterise the wave problem. In particular, we introduce dimensionless variables and denote them without primes, therefore we have

$$\begin{pmatrix} \Phi' \\ x', y', z', h' \\ t' \\ \zeta' \end{pmatrix} = \begin{pmatrix} A'\omega'\lambda'\ \Phi/2\pi \\ \lambda'(x, y, z, h)/2\pi \\ t/\omega' \\ A'\zeta \end{pmatrix}, \tag{2.16}$$

where λ', ω' and A' are the typical values of wavelength, frequency and free-surface amplitude respectively. Now we substitute the dimensionless variables into

equations (2.7), (2.13), (2.14) and (2.15), to get:

$$\nabla^2\Phi = 0 \qquad \text{on} \qquad h < z < \varepsilon\zeta, \tag{2.17}$$

$$\frac{\partial\zeta}{\partial t} + \varepsilon\left(\frac{\partial\Phi}{\partial x}\frac{\partial\zeta}{\partial x} + \frac{\partial\Phi}{\partial y}\frac{\partial\zeta}{\partial y}\right) - \frac{\partial\Phi}{\partial z} = 0 \qquad \text{on} \qquad z = \varepsilon\zeta, \tag{2.18}$$

$$\frac{\partial\Phi}{\partial n} = 0 \qquad \text{on} \qquad z = -h, \tag{2.19}$$

$$\frac{\partial\Phi}{\partial t} + \varepsilon\frac{1}{2}|\nabla\Phi|^2 + \frac{2\pi g}{\omega^2\lambda}\zeta = -P_a \qquad \text{on} \qquad z = \varepsilon\zeta, \tag{2.20}$$

where $\varepsilon = 2\pi A'/\lambda'$ is the wave slope and the sea bottom is assumed to be horizontal. The scales are supposed to reflect the physics properly, so the normalised variables and their derivatives must all be of order unity, that means that the relative importance of each term is entirely indicated by the dimensionless coefficient in front. Let us consider now the following conditions:

- Small-amplitude waves: $\varepsilon \ll 1$.
- Unknown free surface differs by an amount of $\mathrm{O}(\varepsilon)$ from the horizontal plane $z = 0$.

In this situation we obtain a completely linearised approximate problem for small-amplitude waves. Returning to physical variables, we have

$$\nabla^2\Phi' = 0, \qquad -h' < z' < 0, \tag{2.21}$$

$$\frac{\partial\Phi'}{\partial z'} = 0, \qquad z' = -h', \tag{2.22}$$

$$\frac{\partial\zeta'}{\partial t'} = \frac{\partial\Phi'}{\partial z'}, \qquad z' = 0, \tag{2.23}$$

$$\frac{\partial\Phi'}{\partial t'} + g\zeta' = -\frac{P'_a}{\rho}, \qquad z' = 0. \tag{2.24}$$

Furthermore, equations (2.23) and (2.24) may be combined to give

$$\frac{\partial^2 \Phi'}{\partial t'^2} + g\frac{\partial \Phi'}{\partial z'} = -\frac{1}{\rho'}\frac{\partial P'_a}{\partial t'}, \qquad z' = 0. \tag{2.25}$$

2.4 Progressive water waves on constant depth

Due to the linearity of the problem and considering a simple harmonic motion with frequency ω', see [27], we can separate the time factor $e^{-i\omega' t'}$ as follows:

$$\left.\begin{aligned} \zeta'(x', y', t') &= \eta'(x', y') \\ \Phi'(x', y', z', t') &= \phi(x', y', z') \\ \mathbf{v}'(x', y', z', t') &\to \mathbf{v}'(x', y', z') \\ P'(x', y', z', t') + \rho' g' z' &= p'(x', y', z') \end{aligned}\right\} e^{-i\omega' t'},$$

where i is the imaginary unit $(-1)^{1/2}$. Now the linearised governing equations (2.21) - (2.24) can be simplified to

$$\nabla'^2 \phi' = 0, \qquad -h' < z' < 0, \tag{2.26}$$

$$\frac{\partial \phi'}{\partial z'} = 0, \qquad z' = -h', \tag{2.27}$$

$$\frac{\partial \phi'}{\partial z'} + i\omega' \eta' = 0, \qquad z' = 0, \tag{2.28}$$

$$g\eta' - i\omega'\phi' = -\frac{p'_a}{\rho'}, \qquad z' = 0. \tag{2.29}$$

Here we consider two-dimensional propagation along x, so the solution will not depend on y. The boundary-value problem (2.26)-(2.29) can be solved in terms of the spatial potential ϕ'. First we use the method of separation of variables in equation (2.26), so that $\phi'(x', z') = X'(x')Z'(z')$ and equation (2.26) becomes $\nabla'^2 \phi' = \phi'_{xx} + \phi'_{zz} = X'_{xx} Z' + Z'_{zz} X'$. Solving the separated equations we obtain $X'(x') = ae^{ikx'} + be^{-ikx'}$ and $Z'(z') = \alpha \cosh[k(z' + h')] + \beta \sinh[k(z' + h')]$, where k

is the wavenumber, a, b, α, β are amplitude coefficients to be determined. Then,

$$\phi'(x', z') = (ae^{ikx'} + be^{-ikx'})\{\alpha \cosh[k(z' + h')] + \beta \sinh[k(z' + h')]\}. \tag{2.30}$$

In the latter we can simplify $be^{-ikx'}$ because physically we consider only incoming waves propagating in one direction ($x' > 0$). The boundary condition on the sea bottom, (2.27) yields $\beta = 0$, so that

$$\phi'(x', z') = a \cosh[k(z' + h')]e^{ikx'}, \tag{2.31}$$

where the coefficient α has been embedded in a. Let us seek a two-dimensional solution which represent a progressive wave without direct atmospheric forces, that is, $p'_a = 0$ and $\eta = Ae^{ikx'}$. Substitution of the latter expression for ϕ' (2.31) in the dynamic boundary condition on the free surface (2.29) yields

$$a = -\frac{igA'}{\omega'} \frac{1}{\cosh(kh')}, \tag{2.32}$$

therefore

$$\phi'(x', z') = -\frac{igA'}{\omega} \frac{\cosh[k(z' + h')]}{\cosh(kh')} e^{ikx'}. \tag{2.33}$$

Thus we derived the expression for the spatial potential $\phi'(x', z')$ which describes the motion of progressive water waves on constant depth. Finally we require that this expression must satisfy the kinematic boundary condition on the free-surface (2.28), from which we obtain the following well-known *dispersion relation*:

$$\omega'^2 = gk \tanh(kh'). \tag{2.34}$$

The latter equation relates the wavenumber k to the (given) frequency ω of the incident waves.

Chapter 3

Modelling of piezoelectric plates

The term piezoelectric harvester is defined in this thesis as the generator device undergoing vibrations due to a specific form of excitation which in this case, is induced by the wave motion. As stated by Williams and Yates [47], the three basic vibration-to-electric energy conversion mechanisms are the electromagnetic, electrostatic and piezoelectric transductions. Among them, piezoelectric materials in energy harvesting are characterised by large power densities (defined as power output divided by the device volume for a given input) and ease of application. Also, unlike electrostatic energy harvesting, usable voltage outputs in piezoelectric devices can be obtained directly from the constitutive behaviour of the piezoelectric material itself which eliminates the requirement of an external voltage input. As another advantage, unlike electromagnetic devices, piezoelectric ones can be fabricated both in macro-scale and micro-scale due to well-established fabrication techniques [13, 17, 23]. All these characteristics align perfectly with the evolution of low-power-consuming electronics and the need to provide wireless solutions to sensing problems. The goal of this technology is to provide remote sources of electric power and/or to recharge storage devices, such as batteries and capacitors.

Piezoelectricity is a form of coupling between the mechanical and the electrical behaviours of ceramics and crystals belonging to certain classes. These materials exhibit the piezoelectric effect, which can be divided into two phenomena known as the *direct* and the *inverse* piezoelectric effects. When a piezoelectric material is mechanically strained, electric polarization that is proportional to the

applied strain is produced. This is called the direct piezoelectric effect. When the same material is subjected to an electric polarization, it becomes strained and the amount of strain is proportional to the polarization field. This is called the inverse (or converse) piezoelectric effect, [17].

To develop a mathematical model for a piezoelectric energy harvester, first we need to consider the behaviour of the structure to analyse which in this thesis is assumed to be a thin plate (i.e. Kirchhoff plate). The object of this chapter is to develop a model for piezoelectric plates which will be coupled with the potential-flow model for ocean surface waves (see chapter 4) to investigate the power output of piezoelectric WECs. Let us start our review considering an isotropic body made of homogeneous and elastic material. This simplifies the reality of the object to analyse since in this case, all the properties are the same throughout the body and in all directions. Also, under isothermal conditions, the body recovers its original form completely upon removal of the forces causing deformation, and there is a one-to-one relationship between the state of stress and the state of strain. First we study the kinematics of the body in order to define strain-displacement equations. We analyse the constitutive equations, which describe the constitutive behaviour of the body and the relations between stresses and strains. Then, we use the classical theory of plates or Kirchhoff plate theory and in particular we consider the cylindrical bending of plate strips, [38]. After that, we add the influence of an electric field in order to derive the constitutive behaviour of piezoelectric plates. Finally, we select a bimorph configuration in which piezoelectric layers are bonded at both faces of a flexible substrate and we derive a paired system which consists of a coupled mechanical equation and an electrical circuit equation [17].

3.1 Theory and analysis of elastic plates

Given a generic displacement field $\mathbf{u}(x, y, z)$, the deformation of a body can be measured in terms of the Green-Lagrange strain tensor

$$\mathbf{G} = \frac{1}{2}\left(\nabla\mathbf{u} + (\nabla\mathbf{u})^T + \nabla\mathbf{u}\cdot(\nabla\mathbf{u})^T\right). \tag{3.1}$$

If the displacement gradients are so small, $|u_{ij}| \ll 1$, then (3.1) reduces to the

infinitesimal strain tensor

$$\boldsymbol{\varepsilon} = \frac{1}{2}\left(\nabla \mathbf{u} + \nabla \mathbf{u}^T\right), \tag{3.2}$$

or, equivalently,

$$\varepsilon_{ij} = \frac{1}{2}\left(\frac{\partial u_i}{\partial x_j} + \frac{\partial u_j}{\partial x_i}\right). \tag{3.3}$$

Now, let us consider an isotropic plate made of a homogeneous and elastic material. A plate is a structural element with planform dimensions that are larger compared to its thickness and is subjected to loads that cause bending deformation in addition to stretching. Because of the smallness of thickness dimension, it is often not necessary to model them using 3D elasticity equations, therefore simple 2D plate theories can be developed. Under deformation, the plate is subjected to a stress state and we assume that transverse stresses are negligible, so that the constitutive relations between strains and stresses under a plane stress state can be written as follows, see [38]:

$$\begin{pmatrix} \varepsilon_{11} \\ \varepsilon_{22} \\ \varepsilon_{12} \end{pmatrix} = \begin{vmatrix} \frac{1}{E} & \frac{-\nu_p}{E} & 0 \\ \frac{-\nu_p}{E} & \frac{1}{E} & 0 \\ 0 & 0 & \frac{1}{G} \end{vmatrix} \begin{pmatrix} \sigma_{11} \\ \sigma_{22} \\ \sigma_{12} \end{pmatrix}, \tag{3.4}$$

or, equivalently,

$$\begin{pmatrix} \sigma_{11} \\ \sigma_{22} \\ \sigma_{12} \end{pmatrix} = \begin{vmatrix} \frac{E}{1-\nu_p^2} & \frac{\nu_p E}{1-\nu_p^2} & 0 \\ \frac{\nu_p E}{1-\nu_p^2} & \frac{E}{1-\nu_p^2} & 0 \\ 0 & 0 & G \end{vmatrix} \begin{pmatrix} \varepsilon_{11} \\ \varepsilon_{22} \\ \varepsilon_{12} \end{pmatrix}, \tag{3.5}$$

where we use the notation $x = 1$, $y = 2$, $z = 3$ to define material directions and ν_p is the Poisson's ration, E is the Young's modulus, $G = \frac{E}{2(1+\nu_p)}$ is the shear modulus and σ_{ij} are the stress components. Note that σ_{ij} can be interpreted as the jth component of the force per unit area in the current configuration acting on a surface segment whose outward normal at $\mathbf{x}$ is in the ith direction.

3.1.1 Kirchhoff plates

According to the two-dimensional mathematical model proposed by Kirchhoff theory, we assume the following three points, see Fig. 3.1:

(i) Straight lines perpendicular to the mid-surface $z = 0$ before deformation remain straight after deformation.

(ii) Transverse normal are inextensible.

(iii) Transverse normal remains perpendicular to the middle surface after deformation.

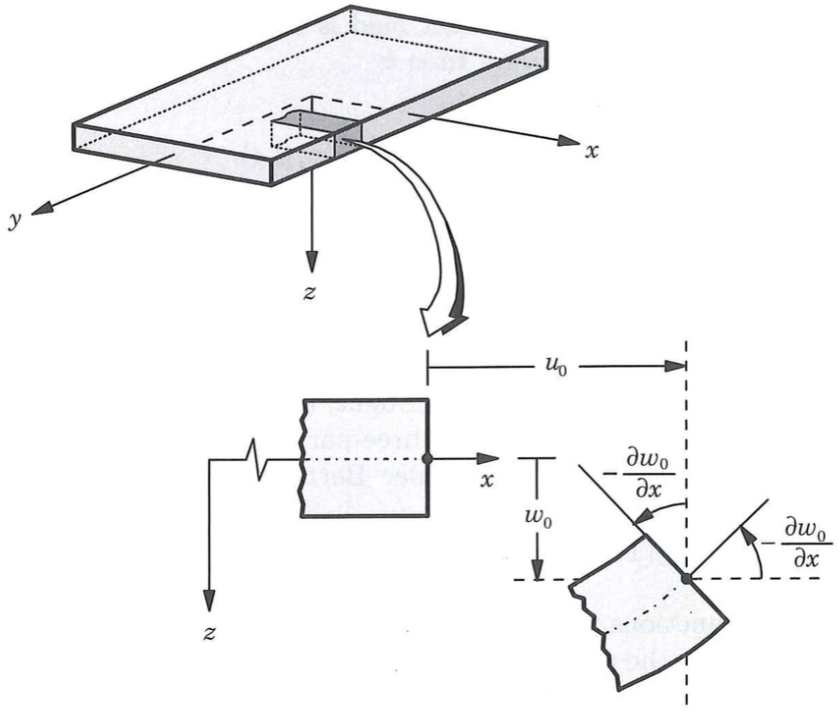

Figure 3.1: Undeformed and deformed geometries of an edge of a plate under the Kirchhoff assumptions, see [38].

Hence the displacement field for time-dependent deformations

$$\begin{cases} u(x,y,z,t) = u_0(x,y,z,t) - z\frac{\partial w}{\partial x} \\ v(x,y,z,t) = v_0(x,y,z,t) - z\frac{\partial w}{\partial y} \\ w(x,y,z,t) = w_0(x,y,z,t) \end{cases}, \tag{3.6}$$

where u_0, v_0, w_0 denote the displacement of a point on the mid-surface $z = 0$. Using the strain tensor components given by equation (3.3) and the displacement field (3.6) we have

$$\begin{cases} \varepsilon_{xx} = \frac{\partial u}{\partial x} = \frac{\partial u_0}{\partial x} - z\frac{\partial^2 w}{\partial x^2} \\ \varepsilon_{yy} = \frac{\partial v}{\partial y} = \frac{\partial v_0}{\partial y} - z\frac{\partial^2 w}{\partial y^2} \\ \varepsilon_{xy} = \frac{1}{2}\left(\frac{\partial u}{\partial y} + \frac{\partial v}{\partial x}\right) = \frac{1}{2}\left(\frac{\partial u_0}{\partial x}\right) - z\frac{\partial^2 w}{\partial xy} \\ \varepsilon_{xz} = \varepsilon_{yz} = \varepsilon_{zz} = 0 \end{cases}, \tag{3.7}$$

which represent linearised strains as a sum of membrane and flexural strains, respectively first and second term of the right-hand side of equations (3.7). Next we introduce thickness-integrated forces (N_{xx}, N_{yy}, N_{xy}) and moments (M_{xx}, M_{yy}, M_{xy}), known as stress resultants:

$$\begin{pmatrix} N_{xx} \\ N_{yy} \\ N_{xy} \end{pmatrix} = \int_{-h/2}^{h/2} \begin{pmatrix} \sigma_{xx} \\ \sigma_{yy} \\ \sigma_{xy} \end{pmatrix} \mathrm{d}z, \qquad \begin{pmatrix} M_{xx} \\ M_{yy} \\ M_{xy} \end{pmatrix} = \int_{-h/2}^{h/2} \begin{pmatrix} \sigma_{xx} \\ \sigma_{yy} \\ \sigma_{xy} \end{pmatrix} z\,\mathrm{d}z. \tag{3.8}$$

Note that since the transverse strains are identically zero, see (3.7), then the transverse stresses do not enter the formulation, but they are present to keep the body in equilibrium, [38].

The governing equation of motion is derived using the principle of virtual displacements and can be simplified in the flexural mode as

$$\frac{\partial^2 M_{xx}}{\partial x^2} + \frac{\partial^2 M_{yy}}{\partial y^2} + \frac{\partial^2 M_{xy}}{\partial x \partial y} + q = I_0 \frac{\partial^2 w}{\partial t^2}, \tag{3.9}$$

where $q(x, y)$ is the distributed transverse load and $I_0 = \int_{-h/2}^{h/2} \rho\,\mathrm{d}z$ is the 0-th order mass moment of inertia (i.e. surface mass).

3.1.2 Analysis of plate strips

Let us now consider the cylindrical bending of a plate strip, where the plate is very long along the y axis and has a finite length Δx along the x axis. The transverse

load q is assumed to be uniform along y, i.e. $q = q(x,t)$. This implies that the rectangular plate can be treated as one-dimensional problem and the derivatives with respect to y are zero for all the quantities. Then, the equation of motion becomes

$$\frac{\partial^2 M_{xx}}{\partial x^2} - I_0 \frac{\partial^2 w}{\partial t^2} = -q. \tag{3.10}$$

Now, using equations (3.8), (3.5) and (3.7) in this order, we have

$$\begin{aligned} M_{xx} &= \int_{-h/2}^{h/2} \sigma_{xx} z \, \mathrm{d}z = \frac{E}{1-\nu^2} \int_{-h/2}^{h/2} \varepsilon_{xx} z \, \mathrm{d}z = \frac{E}{1-\nu^2} \int_{-h/2}^{h/2} -\frac{\partial^2 w}{\partial x^2} z^2 \, \mathrm{d}z \\ &= -\frac{E}{1-\nu^2} \frac{\partial^2 w}{\partial x^2} \left[\frac{z^3}{3} \right]_{-h/2}^{h/2} = -\frac{Eh^3}{12(1-\nu^2)} \frac{\partial^2 w}{\partial x^2} = -D \frac{\partial^2 w}{\partial x^2}, \end{aligned} \tag{3.11}$$

where $D = \frac{Eh^3}{12(1-\nu^2)}$ is the bending stiffness coefficient. Also we assumed $\frac{\partial u_0}{\partial x} = 0$ because it represents membrane strains while we are considering just the flexural mode. Then equation (3.10) becomes

$$D \frac{\partial^4 w}{\partial x^4} + I_0 \frac{\partial^2 w}{\partial t^2} = q, \tag{3.12}$$

which is the equation of motion for a plate strip subject to a cylindrical bending.

3.2 Theory of piezoelectric materials

In general, poled piezoelectric materials are transversely isotropic and here we define the plane of isotropy as the 12-plane (or the xy-plane) to be in agreement with the IEEE Standard on Piezoelectricity [34]. The piezoelectric material therefore exhibits symmetry about the 3-axis (or the z-axis), which is the poling axis of the material. The field variables are not only the stress components (σ_{ij}) and strain components (ε_{ij}), but we need to consider also the influence of the electric field components(E_k) and the electric displacement components (D_k). The constitutive relations can be given using the tensorial representation of the strain-electric displacement form [17]:

$$\varepsilon_{ij} = s_{ijkl} \sigma_{kl} + d_{kij} E_k \tag{3.13}$$

and

$$D_i = d_{ikl}\sigma_{kl} + \varepsilon_{ik}^T E_k, \tag{3.14}$$

where s_{ijkl} are the elastic compliances at constant electric field, d_{kij} are the piezoelectric constants and ε_{ik}^T are the permittivity constants at constant stress. Equations (3.13) and (3.14) can be given in matrix form as

$$\begin{pmatrix} \boldsymbol{\varepsilon} \\ \mathbf{D} \end{pmatrix} = \left| \begin{matrix} \mathbf{s} & \mathbf{d^t} \\ \mathbf{d} & \boldsymbol{\varepsilon^T} \end{matrix} \right| \begin{pmatrix} \boldsymbol{\sigma} \\ \mathbf{E} \end{pmatrix}, \tag{3.15}$$

where the superscript t stands for the transpose. Since the piezoelectric harvester to be modelled in this thesis is assumed to behave as a thin plate (i.e. Kirchoff plate) due to two-dimensional strain fluctuations, the normal stress in the thickness direction and the respective transverse shear components are negligible. The constitutive relations become

$$\begin{pmatrix} \varepsilon_{11} \\ \varepsilon_{22} \\ \varepsilon_{12} \\ D_3 \end{pmatrix} = \left| \begin{matrix} s_{11} & s_{12} & 0 & d_{31} \\ s_{12} & s_{22} & 0 & d_{31} \\ 0 & 0 & s_{33} & 0 \\ d_{31} & d_{31} & 0 & \varepsilon^T \end{matrix} \right| \begin{pmatrix} \sigma_{11} \\ \sigma_{22} \\ \sigma_{12} \\ E_3 \end{pmatrix}, \tag{3.16}$$

where $s_{11} = s_{22} = 1/E$, $s_{12} = -\nu/E$ and $s_{33} = 1/G$. The stress-electric displacement form of the reduced constitutive becomes

$$\begin{pmatrix} \sigma_{11} \\ \sigma_{22} \\ \sigma_{12} \\ D_3 \end{pmatrix} = \left| \begin{matrix} c_{11} & c_{12} & 0 & -e_{31} \\ c_{12} & c_{22} & 0 & -e_{31} \\ 0 & 0 & c_{33} & 0 \\ e_{31} & e_{31} & 0 & \varepsilon^S \end{matrix} \right| \begin{pmatrix} \varepsilon_{11} \\ \varepsilon_{22} \\ \varepsilon_{12} \\ E_3 \end{pmatrix}, \tag{3.17}$$

where c_{ij} the elastic constants at constant electric field, e_{31} is an alternative form of piezoelectric constant and ε^S is a permittivity constant at constant stress.

In particular we have:

$$\begin{vmatrix} c_{11} & c_{12} & 0 & -e_{31} \\ c_{12} & c_{22} & 0 & -e_{31} \\ 0 & 0 & c_{33} & 0 \\ e_{31} & e_{31} & 0 & \varepsilon^S \end{vmatrix} = \begin{vmatrix} s_{11} & s_{12} & 0 & 0 \\ s_{12} & s_{22} & 0 & 0 \\ 0 & 0 & s_{33} & 0 \\ -d_{31} & -d_{31} & 0 & 1 \end{vmatrix}^{-1} \begin{vmatrix} 1 & 0 & 0 & -d_{31} \\ 0 & 1 & 0 & -d_{31} \\ 0 & 0 & 1 & 0 \\ 0 & 0 & 0 & \varepsilon^T \end{vmatrix}. \tag{3.18}$$

Here, the reduced elastic, piezoelectric and permittivity constants are

$$c_{11} = \frac{s_{11}}{(s_{11}+s_{12})(s_{11}-s_{12})} = \frac{E}{1-\nu^2}, \tag{3.19}$$

$$c_{22} = \frac{s_{22}}{(s_{11}+s_{12})(s_{11}-s_{12})} = \frac{E}{1-\nu^2}, \tag{3.20}$$

$$c_{12} = \frac{-s_{12}}{(s_{11}+s_{12})(s_{11}-s_{12})} = \frac{\nu E}{1-\nu^2}, \tag{3.21}$$

$$c_{33} = \frac{1}{s_{33}} = G, \tag{3.22}$$

$$e_{31} = \frac{d_{31}}{s_{11}+s_{12}} = \frac{E d_{31}}{1-\nu}, \tag{3.23}$$

$$\varepsilon^S = \varepsilon^T - \frac{2d_{31}^2}{s_{11}+s_{12}} = \varepsilon^T - \frac{2E d_{31}^2}{1-\nu}. \tag{3.24}$$

In the case of strip plates ($\partial/\partial y = 0$), the constitutive relations reduce to

$$\sigma_{XX} = \frac{E}{1-\nu^2}\varepsilon_{XX} - \frac{E d_{31}}{1-\nu}E_3 \tag{3.25}$$

and

$$D_3 = \frac{E d_{31}}{1-\nu}\varepsilon_{XX} + \varepsilon^S E_3. \tag{3.26}$$

3.3 Distributed-parameter modelling for bimorph piezoelectric plates

Following the analysis of elastic plates in section 3.1, we are now ready to apply the above theories to piezoelectric plates, in which we need to consider the influence of the electric displacement $\mathbf{D}$ and the electric field $\mathbf{E}$. We derive a distributed-parameter model for the governing equations of the piezoelectric plate respect to the local reference system on the plate (X', Y', Z'). We consider that the flexible plate width in the transverse Y' direction is much greater than its length L' along the X' axis. Hence, the deformations of the plate will be modelled as purely two-dimensional, i.e. $\partial/\partial Y' = 0$, see [40]. Variables with primes denote again physical quantities.

In particular, let us assume a bimorph configuration of the piezoelectric material, in which piezoelectric layers are made of discrete piezoelectric patches, each of length $\mathrm{d}X' \ll L'$. These are connected in series and bonded at both faces of the flexible substrate, see [16, 17] with reversed polarities in the Z' direction, as shown in Fig. 3.2. Electrodes of negligible thickness cover the top and the bottom faces of each piezoelectric layer and ensure that a potential difference is established across them.

We model the converter as a uniform composite plate based on the Kirchhoff plate theory [38]. The following assumptions are made:

- Small deformations.
- Linear elastic behaviour of the structure.
- Isotropic material.
- Homogeneous piezoelectric layers characterised by thickness d'_p, Young's modulus E'_p (in N m^{-2}) and Poisson's ratio ν'_p.
- Homogeneous substrate characterised by thickness d'_0, Young's modulus E'_0 and Poisson's ratio ν'_0.

Since the system is homogeneous, the vertical displacement $W'(X', t')$, the stresses $\sigma'_{ij}(X', Z', t')$, with $i, j = X', Y', Z'$, the strains $\epsilon'_{ij}(X', Z', t')$ and the voltage

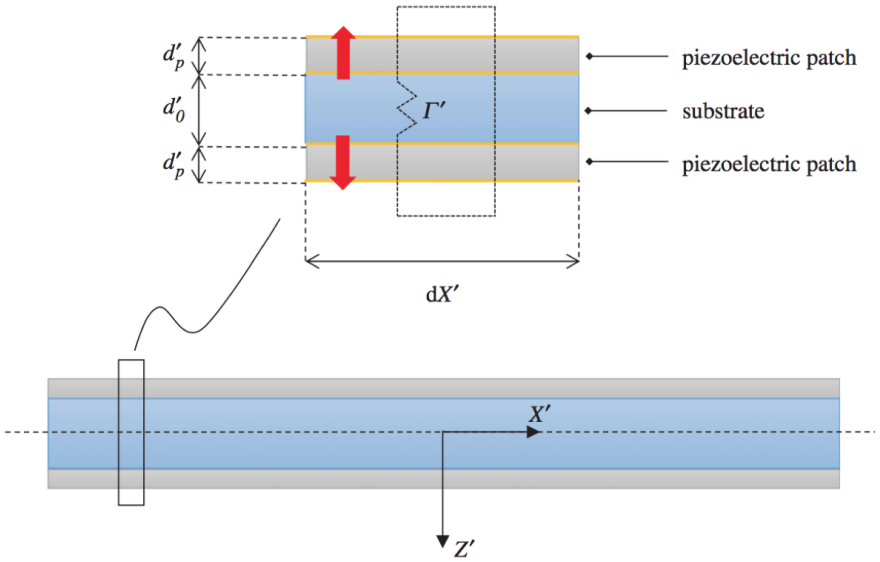

Figure 3.2: Geometry of the piezoelectric plate and detail of the bimorph configuration for an element of length dX'. The bold vertical arrows indicate the poling direction of the piezoelectric layers (from negative to positive pole). Electrodes of negligible thickness cover both faces of each piezoelectric patch. Each pair of piezoelectric patches are shunted with an external resistance $1/\Gamma'$, thus powering a resistive circuit, see [40].

$V'(X', t')$ are continuous along the plate. From now on, primes will be dropped for simplicity in this section.

Let us examine the effect of a vertical surface load $\tilde{q}(X, t)$ (in N m^{-2}) on a plate element of unit width and length $dX \ll L$. Considering a cylindrical bending, the motion of the plate element in the local coordinate system of Fig. 3.2 is described by

$$\frac{\partial^2 M_{XX}}{\partial X^2} - I_b \frac{\partial^2 W}{\partial t^2} = -\tilde{q}, \tag{3.27}$$

see section 3.1.2, where

$$M_{XX} = \int_{-d_0/2-d_p}^{d_0/2+d_p} \sigma_{XX} Z \, dZ \tag{3.28}$$

is the bending moment per unit width (in N) and

$$I_b = \int_{-d_0/2-d_p}^{-d_0/2} \rho_p \, dZ + \int_{-d_0/2}^{d_0/2} \rho_0 \, dZ + \int_{d_0/2}^{d_0/2+d_p} \rho_p \, dZ = 2\rho_p d_p + \rho_0 d_0 \tag{3.29}$$

is the surface density of the bimorph (in Kg m^{-2}). In (3.29), ρ_p is the density of the piezoelectric layers and ρ_0 is the density of the substrate, while the constitutive linear elastic relations are given by:

$$\sigma_{XX} = \frac{E_0}{1-\nu_0^2}\epsilon_{XX} \tag{3.30}$$

for the substrate and

$$\sigma_{XX} = \frac{E_p}{1-\nu_p^2}\epsilon_{XX} - \frac{E_p d_{31}}{1-\nu_p}E_3, \tag{3.31}$$

$$D_3 = \frac{E_p d_{31}}{1-\nu_p}\epsilon_{XX} + \epsilon^S E_3 \tag{3.32}$$

for the patches. In (3.31) and (3.32), we coupled the 1-, 2- and 3-axes of piezoelectricity with the X-, Y-, Z-directions of the material, respectively; $E_3(X,t)$ is the vertical component of the electric field $\mathbf{E}$ (in V m^{-1}); $D_3(X,t)$ is the vertical component of the electric displacement $\mathbf{D}$ (in C m^{-2}); ϵ^S is the permittivity of the piezoceramic at constant strain (in F m^{-1}); d_{31} is the piezoelectric strain constant (in m V^{-1}), see [17,40]. Note that the sign of d_{31} depends on the poling direction of the piezoceramic layers with respect to the orientation of the local Z axis i.e. negative for the upper layer and positive for the lower one (see again Fig. 3.2). Also, because the electrodes are aligned along the horizontal X-direction, the electric field and electric displacement are both aligned along the vertical Z-direction.

We consider that the expression for the linearised strain ϵ_{XX} in absence of axial deformations is given by:

$$\epsilon_{XX} = -Z\frac{\partial^2 W}{\partial X^2}, \tag{3.33}$$

see (3.7). Therefore if we substitute equations (3.30), (3.31) and (3.33) in (3.28) and integrate over the thickness of the plate, we get:

$$M_{XX} = -B\frac{\partial^2 W}{\partial X^2} - \frac{E_p\,|d_{31}|}{1-\nu_p}E_3 d_p(d_0+d_p), \tag{3.34}$$

where

$$B = \frac{E_0 d_0^3}{12(1-\nu_0^2)} + \frac{2E_p d_p}{(1-\nu_p^2)}\left(\frac{d_0^2}{4} + \frac{d_0 d_p}{2} + \frac{d_p^2}{3}\right) \tag{3.35}$$

is the flexural rigidity of the bimorph.

Let us consider the electrical term proportional to E_3. A positive bending of the plate ($\oplus$) generates negative (compression) strains in the upper piezoelectric layer and positive (tension) strains in the lower piezoelectric layer, see [22]. Due to the opposite poling of the two layers, the orientation of the electric displacement vector is the same in both layers. Now let us evaluate the voltage across the plate. Because the piezoelectric layers are connected in series (see again Fig. 3.2), the voltage across the electrodes of each piezoceramic layer is the same. For the bottom layer, $V_b = \int_+^- \mathbf{E} \cdot \mathrm{d}\mathbf{X} = -E_3 d_p$, so that the total voltage is $V(X,t) = 2V_b = -2E_3 d_p$, see [40]. Substituting the latter into (3.34) we get the coupled electromechanical equation:

$$M_{XX} = -B\frac{\partial^2 W}{\partial X^2} + \theta V, \tag{3.36}$$

where

$$\theta = \frac{E_p\,|d_{31}|}{1-\nu_p}\frac{d_0 + d_p}{2} \tag{3.37}$$

is a piezoelectric coupling factor (in N V^{-1} or, equally, in C m^{-1}).

To describe the power take-off (PTO) mechanism of the converter, we couple the electromechanical equation (3.36) with the electrical circuit equations following a common practice in modelling vibration-based energy harvesters, see [17,40]. We consider a resistive electrical load R for each unit element $\mathrm{d}X$ of the plate across which the instantaneous electric field, displacement and voltage, are assumed to be uniform. Hence each piezoelectric layer behaves as a parallel-plate capacitor [42]. The electrical load R is connected to the internal capacitance of the piezoelectric pair, see again Fig. 3.2. The electric charge $\Theta(X,t)$ generated in each piezoelectric layer is estimated using the Gauss law, see [40, 42],

$$\Theta = \oint_S \mathbf{D} \cdot \mathbf{n}\, \mathrm{d}S, \tag{3.38}$$

where $\mathbf{D}$ is the electric displacement over a surface S of unit width and outward normal $\mathbf{n}(X, Z)$ enclosing an electrode.

Let us first consider the bottom piezoelectric layer. It is a parallel-plate capacitor in which $\mathbf{D}$ is oriented along the 3-axis as shown schematically in Fig. 3.3. Note that the only contribution to the integrand in (3.38) come from D_3, since the scalar product between perpendicular versors is null. The bottom piezoelectric patch has length $\mathrm{d}X$ and unit width, hence the patch area is $A = 1\mathrm{d}X$. Therefore equation (3.38) becomes

$$\Theta = \int_{\mathrm{d}X} D_3 \mathbf{i_3} \cdot \mathbf{i_3} \mathrm{d}X = \int_{\mathrm{d}X} D_3 \mathrm{d}X. \tag{3.39}$$

Now we differentiate (3.39) over the elementary area $\mathrm{d}X$, we substitute in the second piezoelectric relation (3.32) and we use $E_3 = -V_b/d_p$, to get

$$Q = \frac{E_p \, |d_{31}|}{1 - \nu_p} \epsilon_{XX} - C_b V_b. \tag{3.40}$$

In the latter, $Q(X, t) = \mathrm{d}\Theta/\mathrm{d}X$ is the charge per unit area of the piezoelectric layer and $C_b = \epsilon^S/(2d_p)$ is the electrical surface capacitance of the bottom layer (in F m^{-2}), see [40, 42]. Substituting $\epsilon_{XX} = -Z\partial^2 W/\partial X^2$ into (3.40) and integrating along Z over any of the piezoelectric patches, we obtain the desired electromechanical equation

$$Q = -\theta \frac{\partial^2 W}{\partial X^2} - C_b V_b. \tag{3.41}$$

A similar equation can be obtained for the top layer. For the series connection, the circuit is equivalent to a single-capacitor circuit of total surface capacitance $C = (2/C_b)^{-1} = \epsilon^S/2d_p$ and total voltage $V = 2V_b$ provided both piezoelectric layers have the same properties. Hence, (3.41) becomes:

$$Q = -\theta \frac{\partial^2 W}{\partial X^2} - CV, \tag{3.42}$$

which is the electrical circuit equation. Now note that to close our system we need one last equation, as we have four unknowns (Q, V, W, M_{XX}), but only three equations, which are (3.27), (3.36) and (3.42), see [40]. Ohm's resistive law gives

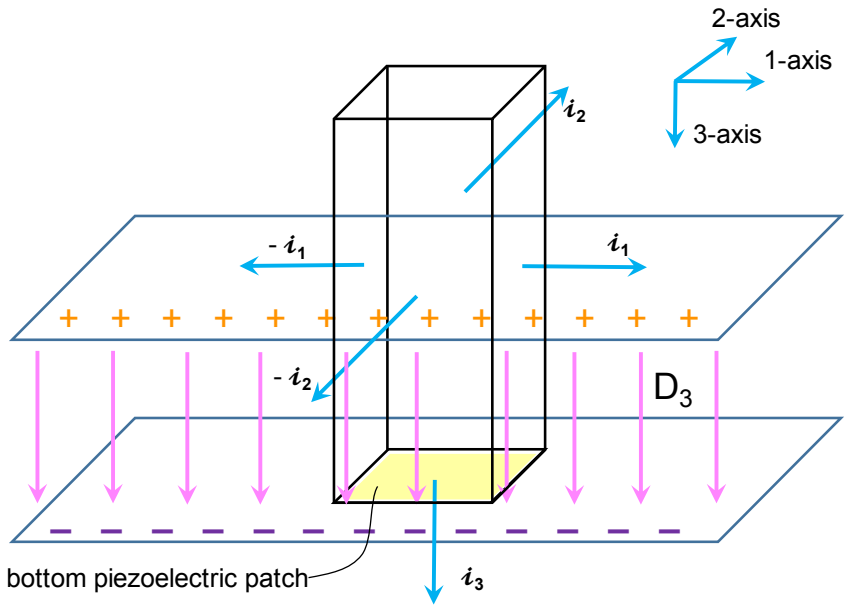

Figure 3.3: As a result of the Gauss law, the electric charge $\Theta(X,t)$ developed in each piezoelectric layer is given by the integral of the electric displacement $\mathbf{D}$ over a surface S enclosing an electrode, which can be written as $\Theta = \oint_S \mathbf{D}\cdot\mathbf{n}\,\mathrm{d}S$ where $\mathbf{n}(X,Z)$ is the outward normal. First we consider the bottom piezoelectric patch of length $\mathrm{d}X$ and unit width, so that the patch area is $A = \mathrm{d}X$ (in yellow). $\mathbf{D}$ is oriented along the 3-axis, therefore $\Theta = \int_A D_3 \mathrm{d}A$.

$\partial\Theta/\partial t = \Gamma V$, where $\Gamma = 1/R$ is the conductance and R is the resistive load of the circuit (in S^{-1}). Differentiating Ohm's law over the elementary area $\mathrm{d}S$, in which V is constant, we get

$$\frac{\partial Q}{\partial t} = GV, \tag{3.43}$$

where $G = \mathrm{d}\Gamma/\mathrm{d}X$ is the surface conductance (in $\mathrm{S\ m}^{-2}$). Therefore the dynamics of the bimorph plate is governed by the electromechanical equations (3.27), (3.36), (3.42) and (3.43), see [40]. Similar systems are derived by [16] and [8]. Also, our plate is immersed in water waves, so the dynamic surface load $\tilde{q}$ of (3.27) is precisely the pressure forcing applied by the wave field on the plate. Hence, the electro-mechanical (EM) equations need to be coupled with a hydrodynamic (HD) system, which is derived in the next chapter. After deriving the coupled hydro-electromechanical system, we will consider two possible real applications of piezoelectric harvesters, such as a double-clamped plate, or a plate fixed at a vertical wall (e.g. a breakwater). We will analyse complex interactions between flexible devices, piezoelectric effect and the superimposition of incident, radiated

and reflected wave components. We will determine new analytical expressions for the hydro-electromechanical dispersion relation and the velocity potentials, predict the power output of both systems and analyse the effect of the vertical wall, see chapter 4.

Chapter 4

Coupling EM and HD problems

In chapters 2 and 3 I obtained governing differential equations characterising a propagating ocean surface wave problem and a flexible piezoelectric plate problem respectively. These two problems (hydrodynamic and the electro-mechanical) can now be coupled in order to derive a novel hydro-electromechanical model for a piezoelectric WEC. In particular, I investigate the interaction of linear water waves with a flexible piezoelectric plate. I consider two possible practical configurations, i.e. a plate fixed at a vertical wall (e.g. a breakwater) and a double-clamped plate. Fig. 4.1 shows schematically both the configurations subjects of this study. As is usual in structural dynamics [38], I introduce a local reference system on the plates, with $(X', Y', Z') = (x', -y', -z' - d')$, so that the local Z' axis points downwards. As in section 3.3, I model deformations of the flexible plates as purely two-dimensional, i.e. $\partial/\partial Y' = 0$.

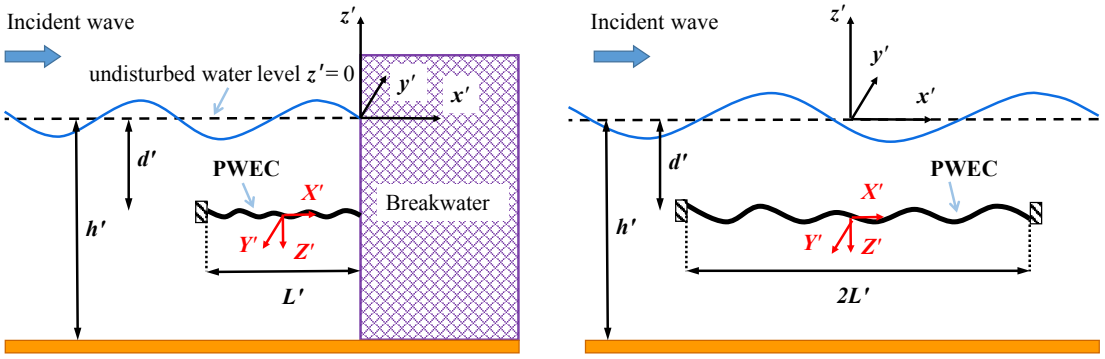

Figure 4.1: Geometry of two piezoelectric wave energy harvester systems in physical variables. A PWEC moored on a breakwater (left-hand side) and a PWEC clamped at both ends to rigid support systems in the ocean (right-end side).

On the left-hand side, the PWEC is a flexible plate clamped to a rigid support system in the ocean at $(x', z') = (-L', d')$ and moored on a caisson breakwater at $(x', z') = (0, d')$, while on the right-hand side, the piezoelectric wave energy converter (PWEC) is clamped at both ends at $(x', z') = (\pm L', -d')$. Note the different position of the global coordinate system (x', y', z') within the two configurations and the different length of the flexible plates along the X' axis, i.e. L' for the converter moored on the breakwater, $2L'$ for the other one. These configurations reproduce possible real applications of piezoelectric WECs, where a superimposition of incident, radiated and reflected wave components interact dynamically with the converter [51]. The interaction of such components affects the energy yield of the device, which attains maximum power when the flexible plate resonates with the wave system [40]. Previous studies on piezoelectric WECs considered rather simplified mathematical models, in which the hydro-electromechanical problem is uncoupled into two separate wave-structure and electric problems. This approach yields a preliminary estimate of the extracted power, but does not give sufficient consideration to the real situation in which the dynamics of waves, structural elasticity and piezoelectricity are inherently coupled in a PWEC. Therefore, the development of a coupled hydro-electromechanical model is fundamental to provide an accurate analysis of the system. Mathematically, I analyse a new fully coupled boundary-value problem based on the complex interactions between wave action, the flexible device and the piezoelectric effect. The solution is derived within the framework of a linearised potential flow theory (chapter 2) by using the method of matching potentials and coupling the hydro electro-mechanical problem with the matching conditions at the common boundaries [40]. I derive analytical expressions for the hydro-electromechanical dispersion relation and potentials. The piezoelectric plate dynamics and predicted power output of the system are obtained using numerical models for both the configurations. Finally, I analyse both mathematical models through convergence tests.

4.1 Flexible piezoelectric wave energy harvester moored on a breakwater

In this section I derive a boundary-value problem for a flexible piezoelectric harvester moored on a breakwater coupling the EM and the HD problems. To find the analytical solution, I follow [7, 29, 40] and split the fluid domain into three different areas using the matching conditions at the common boundaries of the three domains. This yields analytical expressions for the hydro-electromechanical dispersion relation and the velocity potentials for each of the three regions. After that, I come to the numerical part of this study, determining both the roots of the hydro-electromechanical dispersion relation with a two-dimensional Newton-Raphson method of tolerance $\epsilon = 10^{-9}$, see [37,40] and the numerical values of the amplitude coefficients of the potentials. Hence, I solve numerically the boundary-value problem for the piezoelectric wave energy harvester moored on a breakwater and I identify quantities of engineering interest such as the spatial component of the free-surface elevation, the spatial displacement of the plate and the electric power available in the output system per unit width. Finally I select a typical plate configuration and I determine the solutions of the hydro-electromecanical dispersion relation and the behaviour of the extracted power with respect to the period of the incident waves.

4.1.1 Analytical solution of the coupled system

Referring to Fig. 4.2, define a global coordinate system (x', y', z'), with the z'-axis pointing upwards from the undisturbed water level $z' = 0$ and a local reference system on the plate (X', Y', Z') with the local Z' axis points downwards. The x'-axis is directed along the direction of propagation of incoming surface waves of amplitude A' and angular frequency ω'. The bottom of the ocean is located at a constant depth $z' = -h'$ and the piezoelectric converter is clamped to a rigid support system in the ocean at $(x', z') = (-L', d')$ and moored on a caisson breakwater at $(x', z') = (0, d')$. Variables with primes denote again physical quantities.

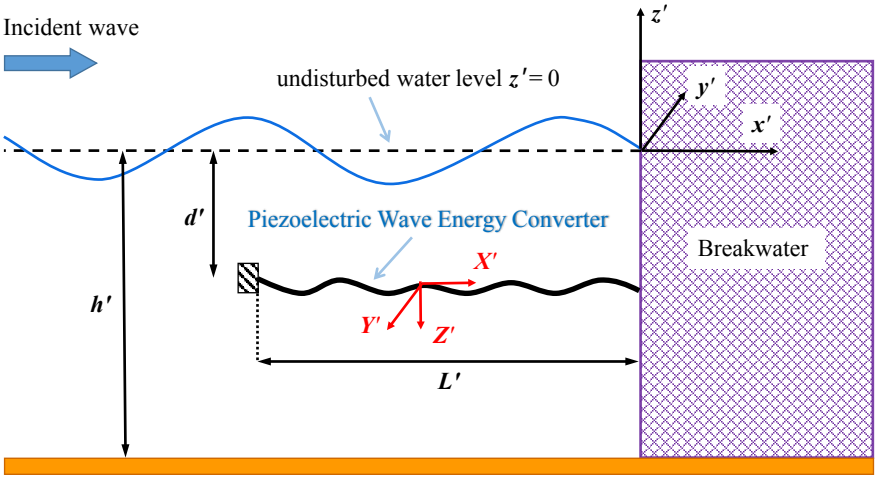

Figure 4.2: Geometry of the system in physical variables.

I aim to couple the model equations of the plate (electro-mechanical problem) with those of the surface waves (hydrodynamic problem). I substitute the electro-mechanical equations (3.36) and (3.42) into the equation of motion (3.27), I replace the surface load $\tilde{q}'$ with the pressure forcing of the waves

$$\tilde{q}'(X',t') = P'(X',-d'+\delta',t') - P'(X',-d'+\delta',t') = P'_+ - P'_-, \qquad \delta \to 0 \quad (4.1)$$

and I rewrite the result in the global reference system (x', y', z'), obtaining the coupled hydro-electromechanical equation

$$\left(B' + \frac{\theta'^2}{C'}\right)\frac{\partial^4 W'}{\partial x'^4} - I'_0\frac{\partial^2 W'}{\partial t'^2} + \frac{\theta'}{C'}\frac{\partial^2 Q'}{\partial x'^2} = \Delta P'. \quad (4.2)$$

In the latter, W' is defined positive upwards and $\Delta P'(x',t') = P'_- - P'_+$ is the pressure jump across the plate in the z' direction. Using the linearised Bernoulli equation, see [27], I can assume $\Delta P' = -\rho(\partial\Delta\Phi')/\partial t'$, where $\Delta\Phi'$ is the jump of the spatial potential Φ' across the plate along the z' direction. I also rewrite (3.42) and (3.43) in the global reference system to get

$$Q' = \theta'\frac{\partial^2 W'}{\partial x'^2} + C'V' \quad (4.3)$$

and

$$\frac{\partial Q'}{\partial t} = -GV'. \quad (4.4)$$

Let me introduce the following non-dimensional variables, see [40]:

$$(x', y', z', h', d') = L'(x, y, z, h, d), \quad t' = \sqrt{\frac{L'}{g}}t, \quad \Phi' = \sqrt{gL'}A'\Phi, \quad W' = A'W,$$
$$Q' = A'\sqrt{\frac{gI_0'C'}{L'}}, \quad V' = A'\sqrt{\frac{gI_0'}{L'C'}}V, \tag{4.5}$$

so that I can obtain the non-dimensional form of our equations. The coupled hydro-elecromechanical equation of motion (4.2) becomes

$$\beta(1+\alpha^2)\frac{\partial^4 W}{\partial x^4} + \frac{\partial^2 W}{\partial t^2} - \alpha\sqrt{\beta}\frac{\partial^2 Q}{\partial x^2} = -r\frac{\partial \Delta\Phi}{\partial t}, \tag{4.6}$$

where $\alpha = \theta'/\sqrt{B'C'}$ is a non-dimensional piezoelectric coupling parameter, $\beta = B'/(L'^3 g I_0')$ is a non-dimensional stiffness and $r = \rho L'/I_0'$ is a surface density ratio. Analogously, the electromechanical equation (4.3) and the circuit equation (4.4) become, respectively,

$$Q - V - \alpha\sqrt{\beta}\frac{\partial^2 W}{\partial x^2} = 0 \tag{4.7}$$

and

$$\xi\frac{\partial Q}{\partial t} = -V, \tag{4.8}$$

where $\xi = C'/G'\sqrt{g/L'}$ is the non-dimensional resistive term.

Non-dimensionalisation of the hydrodynamic equations (2.21), (2.22) and (2.25) according to (4.5) yields, respectively,

$$\nabla^2\Phi = 0 \tag{4.9}$$

for the Laplace equation in the fluid domain,

$$\frac{\partial \Phi}{\partial z} = 0 \tag{4.10}$$

for the no-flux condition at the sea bottom and

$$\frac{\partial^2 \Phi}{\partial t^2} + \frac{\partial \Phi}{\partial z} = 0 \tag{4.11}$$

for the kinematic-dynamic boundary condition on the free surface. Also, looking at the configuration shown in Fig. 4.2, I can add further boundary conditions to the governing differential equations of the EM-HD problem that we are considering in this section. Since the plate is clamped at both ends, I have

$$W'(-L,t) = W(0,t) = \left.\frac{\partial W'(x',t')}{\partial x'}\right|_{x'=-L'} = \left.\frac{\partial W'(x',t')}{\partial x'}\right|_{x'=0} = 0, \tag{4.12}$$

where I already used the global reference system. The boundary condition for the breakwater is

$$\frac{\partial \Phi'}{\partial x'} = 0, \qquad x' = 0. \tag{4.13}$$

Finally, Φ' needs to satisfy a kinematic condition on the surface of the plate. Let λ' be the characteristic wavelength of the incident waves. Assume that such a wavelength is comparable to the total length of the device, $\lambda'/(2L') = O(1)$. Because the total thickness of the plate is much smaller than λ', I can apply the thin-plate hypothesis and consider the thickness of the plate to be immaterial in solving the potential-flow problem, see [40,41]. This yields the kinematic condition on the plate

$$\frac{\partial W'}{\partial t'} = \frac{\partial \Phi'}{\partial z'}, \qquad -L' < x' < 0, \quad z' = -d' \pm \delta, \quad \delta \to 0. \tag{4.14}$$

Non-dimensionalisation of equations (4.12)-(4.14) according to (4.5) yields, respectively,

$$W(-1,t) = W(0,t) = \left.\frac{\partial W(x,t)}{\partial x}\right|_{x=-1} = \left.\frac{\partial W(x,t)}{\partial x}\right|_{x=0} = 0, \tag{4.15}$$

$$\frac{\partial \Phi}{\partial x} = 0 \qquad x = 0 \tag{4.16}$$

and

$$\frac{\partial W}{\partial t} = \frac{\partial \Phi}{\partial z} \qquad -1 < x < 0, \quad z = -d \pm \delta, \quad \delta \to 0. \tag{4.17}$$

As in (2.4), I assume that the wave forcing is harmonic with frequency ω, so I

can factorise out the time variable by introducing the spatial variables

$$[\Phi(x,z,t), P(x,z,t), W(x,t), Q(x,t), V(x,t)] = \Re\{[\phi(x,z), p(x,z), w(x), q(x), v(x)]e^{-i\omega t}\}. \tag{4.18}$$

In the following, the real part operator $\Re$ will be omitted for the sake of brevity and subscripts denote differentiation with respect to the relevant variable. Now I substitute (4.18) in the hydrodynamic equations (4.9)-(4.11), into the electromechanical equations (4.6)-(4.8), into the kinematic conditions at the ends of the plate (4.15) and into the kinematic condition on the breakwater (4.16). Finally, I substitute (4.18) into the kinematic condition on the plate (4.17) which relates Φ and W, therefore, coupling equations together, I obtain the following hydro-electromechanical boundary-value problem in terms of the spatial potential ϕ only:

$$\nabla^2\phi = 0, \qquad \text{in the fluid domain,} \tag{4.19}$$

$$\phi_z - \omega^2\phi = 0, \qquad z = 0, \tag{4.20}$$

$$\phi_z = 0, \qquad z = -h, \tag{4.21}$$

$$\beta\left(1 + \frac{\alpha^2\omega\xi}{i+\omega\xi}\right)\phi_{xxxxz} - \omega^2\phi_z = \omega^2 r\Delta\phi, \quad -1 < x < 0, \quad z = -d \pm \delta, \quad \delta \to 0, \tag{4.22}$$

$$\begin{aligned} \phi_z = \phi_{xz} = 0, \quad x = -1, \quad z = -d \pm \delta, \quad \delta \to 0, \\ x = 0, \quad z = -d \pm \delta, \quad \delta \to 0, \end{aligned} \tag{4.23}$$

$$\phi_x = 0, \qquad x = 0, \qquad -h < z < 0. \tag{4.24}$$

Expressions (4.19)-(4.21) are the hydrodynamic equations, (4.22) is the dy-

namic boundary condition on the plate, (4.23) are the kinematic boundary conditions at the ends of the plate and (4.24) is the boundary condition for the breakwater. If I consider the short-circuit limit $\xi \to 0$, the fifth derivative of the velocity potential in (4.22) is multiplied only by the non-dimensional stiffness β, then the boundary-value problem is equivalent to that of a submerged elastic plate without power extraction [29, 40, 45]. In fact in (4.22), the complex coefficient $\alpha^2\omega\xi/(i+\omega\xi)$ is a dissipative term which models the extraction of energy from the system.

The system (4.19)-(4.24) will be solved with the method of matching potentials and appropriate conditions at each of the physical boundaries of the system, see [7, 27, 29, 40]. As shown in Fig. 4.3, I split the fluid domain into three different areas.

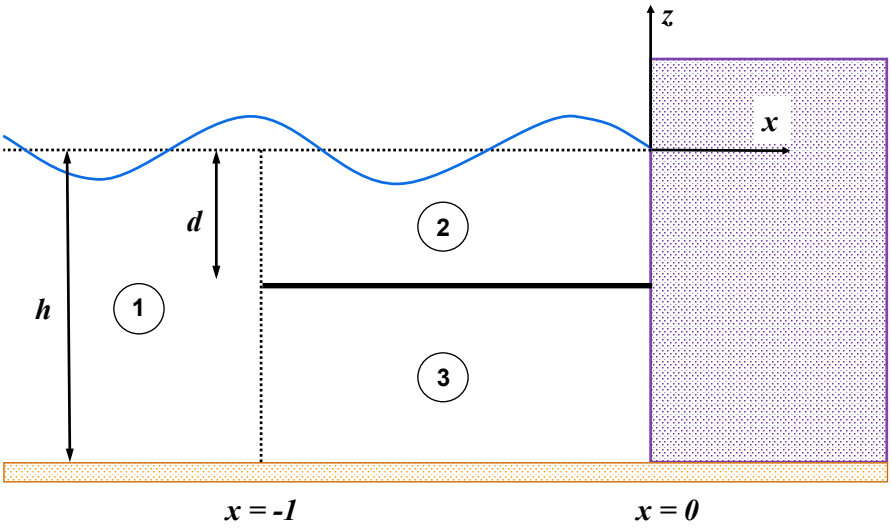

Figure 4.3: Domain decomposition used to solve the boundary-value problem.

The matching conditions at the common boundaries of the three domains are

$$\phi_{2z} = \phi_{3z}, \qquad x \in (-1, 0), \quad z = -d, \tag{4.25}$$

$$\phi_1 = \phi_2, \quad \phi_{1x} = \phi_{2x}, \qquad x = -1 \quad z \in (-d, 0), \tag{4.26}$$

$$\phi_1 = \phi_3, \quad \phi_{1x} = \phi_{3x} \qquad x = -1 \quad z \in (-h, -d), \tag{4.27}$$

where the ϕ_i denote the potential ϕ in each area $i = 1, 2, 3$. I also require that the scattered potential in the open ocean area 1 is outgoing in the far field [27]. I shall now solve the boundary-value problem separately in each region and then match the potentials via (4.25)-(4.27).

Region 1

In region 1 the potential $\phi_1(x, z)$ must satisfy equations (4.19) - (4.21). Applying the separation of variables rule to (4.19), I get $\phi_1(x, z) = X(x)Z(z)$. Now I use the conditions (4.20) and (4.21) and I obtain $\phi_1(x, z) = (a_0 e^{ikx} + b_0 e^{-ikx}) \cosh[k(z + h)]$. Note that the eigenvalue condition for the wave number k is the well-known dispersion relation $\omega^2 = k \tanh(kh)$, see Chapter 2. There is a pair of real roots $\pm k$ which correspond to the same normalised eigenfunction, hence only the positive real root needs to be considered. In addition, there are also imaginary eigenvalues $k = i\kappa$ corresponding to the real solutions of $\omega^2 = -\kappa \tan(\kappa h)$. The last admits infinite number of discrete roots $\kappa = \pm k_n$. Again it is only necessary to consider positive k_n, see [27]. Consequently we can use the expression $\phi_1(x, z) = (a_0 e^{ikx} + b_0 e^{-ikx}) \cosh[k(z+h)] + \sum_{n=1}^{+\infty} (a_n e^{k_n x} + b_n e^{-k_n x}) \cos[k_n(z+h)]$. Now, $b_n = 0$ because $|X(x)|$ is limited. Then we can say that in region 1 the solution of the system is the superimposition of incident (right-going) wave, radiated and reflected (left-going) waves and evanescent waves and it is expressed by

$$\phi_1(x, z) = -\frac{2i}{\omega} \frac{\cosh[k(z + h)]}{\cosh(kh)} \cos(kx) + \sum_{n=0}^{\infty} R_n e^{-i\kappa_n x} c_n Z_n(z), \tag{4.28}$$

where the R_n are unknown complex coefficients. The Z_n are the orthonormal functions:

$$Z_n(z) = \sqrt{2} \cosh[\kappa_n(z + h)]/(h + \omega^{-2} \sinh^2(\kappa_n h))^{1/2}, \tag{4.29}$$

which satisfy $\int_{-h}^{0} Z_n Z_m dz = \delta_{nm}$, where δ_{nm} is the Kronecker delta, see [27] and [40] and the c_n are complex constants: $c_n = (h + \omega^{-2} \sinh^2(\kappa_n h))^{1/2}/\sqrt{2}$.

Region 2 and 3

Both ϕ_2 and ϕ_3 must satisfy equations (4.19) and (4.22)-(4.24) and the vertical continuity condition (4.25), in addition ϕ_2 must satisfy the surface condition (4.44) while ϕ_3 must satisfy the bottom boundary condition (4.21). First I apply again the separations of variables to the Laplace equation choosing $\phi_{(2,3)}(x,z) = \varphi_{(2,3)}(x)\psi_{(2,3)}(z)$ and I solve simultaneity both systems in regions 2 and 3. Now the vertical continuity condition (4.25) reduces to

$$\left.\frac{\partial\psi_2(z)}{\partial z}\right|_{z=-d} = \left.\frac{\partial\psi_3(z)}{\partial z}\right|_{z=-d}. \tag{4.30}$$

The latter is a reasonable physical hypothesis since $\psi^{(2,3)}(z)$ transfer the velocity along the z-direction. The solution of the problem in terms of the spatial potential ϕ_2 and ϕ_3 is

$$\phi_{2,3}(x,z) = \sum_{n=-2}^{\infty}(A_n e^{i\sigma_n x} + B_n e^{-i\sigma_n x})\psi_n^{(2,3)}, \tag{4.31}$$

where the A_n and B_n are unknown complex coefficients, $\psi_n^{(2)}(z) = [\sigma_n\cosh(\sigma_n z) + \omega^2\sinh(\sigma_n z)]\sinh[\sigma_n(h-d)]$ and $\psi_n^{(3)}(z) = [\omega^2\cosh(\sigma_n d) - \sigma_n\sinh(\sigma_n d)]\cosh[\sigma_n(z+h)]$ are the vertical eigenfunctions of the regions 2 and 3, respectively, the σ_n are horizontal wave numbers which can be determined by substituting (4.31) into the boundary condition on the plate (4.22). This yields a novel hydro-electromechanical dispersion relation, see [40]:

$$\begin{aligned} F(\sigma_n) = &\left[\beta\left(1+\frac{\alpha^2\omega\xi}{i+\omega\xi}\right)\sigma_n^4 - \omega^2\right][\omega^2\sigma_n\cosh(\sigma_n d) - \sigma_n^2\sinh(\sigma_n d)] \\ &\times\tanh[\sigma_n(h-d)] - \omega^2 r\{\omega^2\cosh(\sigma_n d) - \sigma_n\sinh(\sigma_n d) \\ &+ [\omega^2\sinh(\sigma_n d) - \sigma_n\cosh(\sigma_n d)]\tanh[\sigma_n(h-d)]\} = 0, \end{aligned} \tag{4.32}$$

which is an even complex function of σ_n and admits an infinite number of complex solutions $\pm\sigma_n$. I determine the roots of the hydro-electromechanical dispersion relation for a typical system configuration with a two-dimensional Newton-Raphson method of tolerance $\epsilon = 10^{-9}$, see [40].

The choice to start the series in (4.31) from -2 is only practical and does not affect the solution. Expressions (4.31) is the superimposition of damped waves in the plate region, see [40]. The complex coefficients R_n, A_n and B_n in (4.28) and (4.31) are obtained by solving numerically the matching conditions (4.25)-(4.27) in combination with the clamping conditions on the plate (4.23) and (4.24), see next section.

4.1.2 Numerical solution of the coupled system

Following the procedure in [40], substitute the solutions ϕ_2 and ϕ_3 (4.31) into the physical condition on breakwater (4.24). Then, multiply both equations by $Z_m(z)$, $m = 0, 1, ...,$ integrate them along z over the respective domains and finally sum the results to obtain

$$\sum_{n=-2}^{N} \sigma_n (A_n - B_n) b_{mn} = 0, \qquad m = 0, 1, 2, ..., N, \tag{4.33}$$

where $b_{mn} = \int_{-d}^{0} \psi_n^{(2)}(z) Z_m(z) dz + \int_{-h}^{-d} \psi_n^{(3)}(z) Z_m(z) dz$ is a complex coefficient. In (4.33), the orthogonality of the vertical modes Z_m has been exploited and the sum has been truncated to a finite value $n = N$ for numerical evaluation. Now I use the same procedure to match the fluxes substituting the solution ϕ_1 (4.28), ϕ_2 and ϕ_3 (4.31) into the first conditions of both (4.26) and (4.27) and we obtain

$$R_m = \left[\frac{2ia}{\omega} \cos(k) \delta_{0m} e^{-i\kappa_m} + \sum_{n=-2}^{N} (A_n e^{-i(\sigma_n + \kappa_m)} + B_n e^{i(\sigma_n - \kappa_m)}) b_{mn} \right] \frac{1}{c_m}, \tag{4.34}$$

where c_m is the same as c_n in (4.28), $a = [h + \omega^{-2} \sinh^2(kh)]^{1/2} / \sqrt{2} \cosh(kh)$ and $m = 0, 1, 2, ..., N$. Using once again the same procedure for the second conditions of both (4.26) and (4.27), I get

$$\frac{2ik}{\omega} a \sin(k) \delta_{0m} - i\kappa_m R_m c_m e^{i\kappa_m} = \sum_{n=-2}^{N} i\sigma_n (A_n e^{-i\sigma_n} + B_n e^{i\sigma_n}) b_{mn}, \tag{4.35}$$

with $m = 0, 1, 2, ..., N$. Now I substitute the expression for R_m (4.34) in (4.35).

This yields

$$\frac{2ia}{\omega}\delta_{0m}[ik\sin(k)-\kappa_m\cos(k)]=\sum_{n=-2}^{N}b_{mn}[A_ne^{-i\sigma_n}(\sigma_n+\kappa_m)-B_ne^{i\sigma_n}(\sigma_n-\kappa_m)], \tag{4.36}$$

with $m=0,1,2,...,N$. Finally, from the kinematic boundary conditions at the end of the plate (4.23), I obtain

$$\sum_{n=-2}^{N}(A_n+B_n)f_n=0, \tag{4.37}$$

$$\sum_{n=-2}^{N}(A_ne^{-i\sigma_n}+B_ne^{i\sigma_n})f_n=0, \tag{4.38}$$

$$\sum_{n=-2}^{N}\sigma_n(A_n-B_n)f_n=0, \tag{4.39}$$

$$\sum_{n=-2}^{N}\sigma_n(A_ne^{-i\sigma_n}-B_ne^{i\sigma_n})f_n=0, \tag{4.40}$$

where

$$f_n=[\omega^2\cosh(\sigma_nd)-\sigma_n\sinh(\sigma_nd)]\sigma_n\sinh[\sigma_n(h-d)], \tag{4.41}$$

with $m=0,1,2,...,N$. Expressions (4.33), (4.36) and (4.37)-(4.40) are $2N+6$ equations in $2(N+3)$ unknowns, therefore the system can be solved numerically for the A_n and B_n with a suitable choice of N. (Details of the numerical convergence of the system are given in section 4.3). This has been implemented in a Matlab code, see appendix A, that allows me to identify the numerical solutions of the system and to determine all the quantities of engineering interest i.e. the spatial displacement of the flexible plate, the spatial component of the free-surface elevation in the regions 1 and 2 and finally the average electric power in the output system per unit width, as follows.

Spatial displacement of the flexible plate

The spatial displacement of the plate can be evaluated using the kinematic condition on the plate (4.14). I use dimensionless variables (2.16), I factor time out as in (4.18) and I substitute the expression for the potential (4.31). This yields

$$w(x) = \frac{i}{\omega} \sum_{n=-2}^{N} (A_n e^{i\sigma_n x} + B_n e^{-i\sigma_n x}) f_n, \tag{4.42}$$

where the sum has been truncated to a finite value $n = N$ for numerical evaluation.

Spatial component of the free-surface elevation in regions 1 and 2

Defining the free-surface elevation as in (2.11) and using the dimensionless variables (2.16), we write $\zeta_t = \Phi_z|_{z=0}$, see [27]. Then I factor time out by defining $\zeta(x,t) = \Re\{\eta(x)e^{-i\omega t}\}$. Hence

$$\eta_i(x) = \frac{i}{\omega}\phi_{i_z}(x,z)|_{z=0}, \qquad i = 1,2 \tag{4.43}$$

is the spatial component of the free-surface elevation in the region $i = 1, 2$, [40]. Substituting the relevant forms for the potentials (4.28) and (4.31) in (4.43), I obtain respectively

$$\eta_1(x) = \frac{2}{\omega^2} k \tanh(kh)\cos(kx) + \frac{i}{\omega}\sum_{n=0}^{N} R_n e^{-i\kappa_n x}\kappa_n \sinh(\kappa_n h) \tag{4.44}$$

and

$$\eta_2(x) = \frac{i}{\omega}\sum_{n=-2}^{N} (A_n e^{i\sigma_n x} + B_n e^{-i\sigma_n x})\omega^2\sigma_n \sinh[\sigma_n(h-d)]. \tag{4.45}$$

Power output of the system

The electric power obtainable from the output system per unit width, in physical variable, is

$$\mathcal{P}' = -V'\frac{\partial Q'}{\partial t'}, \tag{4.46}$$

see [31, 40]. Using the non-dimensionalisation (4.5) in equation (4.46) and substituting the circuit equation (4.8) we obtain

$$\mathcal{P}' = \frac{A'gI_b'}{L'}\xi\sqrt{\frac{g}{L'}}\left(\frac{\partial Q}{\partial t}\right)^2 = \left(\frac{A'g}{L'}\right)^2 I_b'\frac{C'}{G'}\left(\frac{\partial Q}{\partial t}\right)^2. \tag{4.47}$$

Now let me integrate over the length of the device and over the period $T' = 2\pi/\omega'$, so that I obtain the average electric power in the output system per unit width, in physical variables

$$\overline{\mathcal{P}}' = \int_{-L'}^{0}\left[\frac{1}{T'}\sqrt{\frac{L'}{g}}\int_0^{T'}\left(\frac{A'g}{L'}\right)^2 I_b'\frac{C'}{G'}\left(\frac{\partial Q}{\partial t}\right)^2\sqrt{\frac{g}{L'}}\,\mathrm{d}t'\right]\frac{\mathrm{d}x'}{L'}, \tag{4.48}$$

which can be written as

$$\overline{\mathcal{P}}' = \frac{(A'g)^2}{L'}I_b'\frac{C'}{G'}\overline{\mathcal{P}}, \tag{4.49}$$

in W m^{-1} where

$$\overline{\mathcal{P}} = \int_{-1}^{0}\left[\frac{1}{T}\int_0^{T}\left(\frac{\partial Q}{\partial t}\right)^2\mathrm{d}t\right]\mathrm{d}x \tag{4.50}$$

is the non-dimensional average power extracted by the device per unit width over a cycle. Note that this results can be reproduced only if the design of the converter is such that voltage cancellations do not occur along the plate, [17, 40]. Finally I can evaluate the non-dimensional average power per unit width of the device, substituting equations (4.7) and (4.8) in (4.50) and factor time out with (4.18) as follows

$$\overline{\mathcal{P}} = \int_{-1}^{0}\left[\frac{1}{T}\int_0^{T}\Re\left\{\frac{-i\omega\alpha w_{xx}}{\gamma(1-i\omega\xi)}e^{-i\omega t}\right\}\Re\left\{\frac{-i\omega\alpha w_{xx}}{\gamma(1-i\omega\xi)}e^{-i\omega t}\right\}\mathrm{d}t\right]\mathrm{d}x. \tag{4.51}$$

The latter can be written as

$$\overline{\mathcal{P}} = \frac{\omega^2}{2}\int_{-1}^{0}\left|\frac{\alpha w_{xx}}{\gamma(1-i\omega\xi)}\right|^2\mathrm{d}x, \tag{4.52}$$

where we exploited the property $1/T\int_0^T\Re\{Ae^{-i\omega t}\}\Re\{Be^{-i\omega t}\}\,\mathrm{d}t = 1/2\Re\{AB^*\}$.

4.1.3 Results

I select a typical plate configuration to analyse the roots of the hydro-electromechanical dispersion relation (4.32) and the dynamics of wave power extraction. Referring to Fig. 4.2, the length of the plate is $L' = 10$ m, the water depth is $h' = 10$ m and the submergence of the plate is $d' = 2$ m. In addition I assume that the amplitude of the ocean surface waves is $A' = 1$ m and the bimorph piezoelectric plate is characterised by: silicone rubber layer (substrate) of thickness $d'_0 = 0.01$ m, polyvinylidene fluoride (PVDF) piezoelectric layers of thickness $d'_p = 1.1 \times 10^{-4}$ m. Typical values of the system coefficients for commercial silicone rubber and PVDF are shown in the following Tab. 4.1, see e.g. [16, 17, 40, 44].

Table 4.1: Silicone rubber and PVDF coefficients for a PWEC moored on a caisson breakwater.

Stiffness	**Piezoelectric coupling parameter**	**Resistive term**
β	α	ξ
3.8×10^{-4}	0.24	1

Roots of the hydro-electromechanical dispersion relation

A two-dimensional Newton-Raphson method of tolerance $\epsilon = 10^{-9}$ has been used for finding successively better approximations to the roots of the hydro-electromechanical dispersion relation (4.32) as in [11]. The location of the first 18 eigenvalues of (4.32) is shown in Fig. 4.4 and their numerical values are reported in Tab. 4.2. In this example the period of the incident wave is T'= 5 s.

The dispersion relation obtained from Hassan and Meylan, [29] for a submerged elastic plate coincides with the hydro-electromechanical equation (4.32) in the short-circuit limit $\xi \to 0$. Within this limit, (4.32) admits two complex eigenvalues, say σ_{-2} and σ_{-1}, two positive real eigenvalues, say σ_0 and σ_1 and an infinite number of positive imaginary eigenvalues σ_n, $n = 2, 3, ...$ for typical plate parameters [29]. As shown in Fig. 4.4, the location of the roots of the hydro-electromechanical dispersion relation changed with respect to what was found by Hassan & Meylan. This is due to the presence of the piezoelectric term proportional to ξ in (4.32). In fact, as reported in Tab. 4.2, there are no real roots, no imaginary roots,

an infinite number of complex solutions σ_n, $n = 2, 3, ...$ shifted into the first quadrant of the complex plane with respect to the short-circuit scenario, therefore the real part is much smaller than the imaginary part (see again Tab. 4.2). These modes physically describe evanescent waves, [27]. Physically, the real part of the wavenumber is related to the propagating part of the perturbation, while the imaginary part corresponds to the damping rate. As for the submerged elastic plate, there are still two roots in the complex plane, which we name σ_{-2} and σ_{-1}, following [7, 29, 40].

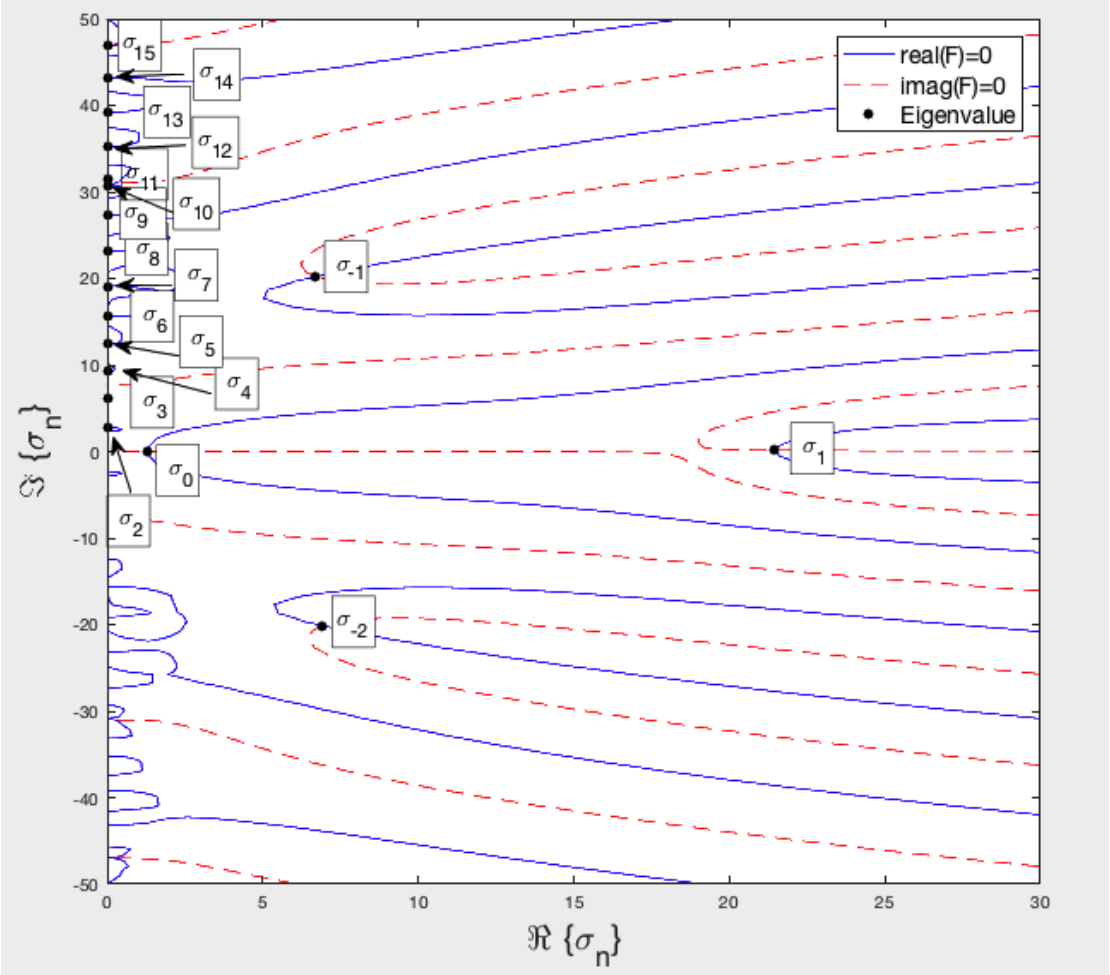

Figure 4.4: Location of the first 18 eigenvalues of the hydro-electromechanical dispersion relation $F(\sigma_n) = 0$ in the complex σ_n plane. The solid blue lines correspond to the contours $\Re\{F\} = 0$, while the dashed red lines identify the contours $\Im\{F\} = 0$.

These roots correspond to heavily damped oscillatory modes, as discussed by Behera and Sahoo [7]. Finally, the numerical values of σ_0 and σ_1 are characterised by a small imaginary part which is associated to weakly damped progressive waves.

Table 4.2: Numerical values of the complex eigenvalues σ_n, solutions of the dispersion relation (4.32) represented in Fig. 4.4.

Eigenvalue	**Numerical Value**	**Behaviour in the plate region**
σ_{-2}	6.9100 -20.1783i	Oscillatory heavily damped
σ_{-1}	0.0018 +46.9518i	Oscillatory heavily damped
σ_0	1.2990 + 0.0000i	Long-crested weakly damped
σ_1	21.4641 + 0.1346i	Short-crested weakly damped
σ_2	0.0000 + 2.7537i	Evanescent
σ_3	0.0001 + 6.0981i	Evanescent
σ_4	0.0009 + 9.3220i	Evanescent
σ_5	0.0013 +12.5121i	Evanescent
σ_6	0.0000 +15.6379i	Evanescent
σ_7	0.0073 +19.1035i	Evanescent
σ_8	6.6720 +20.2396i	Evanescent
σ_9	0.0125 +23.1556i	Evanescent
σ_{10}	0.0081 +27.2714i	Evanescent
σ_{11}	0.0165 +30.7592i	Evanescent
σ_{12}	0.0002 +31.3891i	Evanescent
σ_{13}	0.0015 +35.2935i	Evanescent
σ_{14}	0.0010 +39.2397i	Evanescent
σ_{15}	0.0006 +43.1779i	Evanescent

Note from Tab. 4.2 that $\Re\{\sigma_1\} \gg \Re\{\sigma_0\}$ which means that σ_0 and σ_1 correspond, respectively, to long- and short-crested waves. This does not happen in the flexible-plate case of Hassan & Meylan [29] and in the porous plate case of [7], where the two wavenumbers are comparable. Therefore, the occurrence of a coupled system of short- and long-crested weakly damped progressive waves that propagate in the plate region is a characteristic of the submerged piezoelectric plate.

Power output of the system

In subsection 4.1.2 I derived a linearised theory to predict the power output of the system. Let me now investigate the effect of the incident wave period on the generated power. The plot of Fig. 4.5 shows the behaviour of the average extracted power (4.49) with respect to the period of the incident waves, for the bimorph piezoelectric plate moored on a breakwater studied in this section. The hydro-electromechanical behaviour of the device causes sharp resonant peaks in the generated power. Considering the first 18 vibrational modes of flexural waves on the plate, we identify the existence of 3 resonant periods in the interval [4-9] s

at which the extracted power is significant. In particular, the maximum peak of about 8.01 kW/m occurs at T'= 5.2 s, as shown in Fig. 4.5. Note that this value is about two orders of magnitude greater than the power output of piezoelectric beams predicted by simplified uncoupled models [48–50].

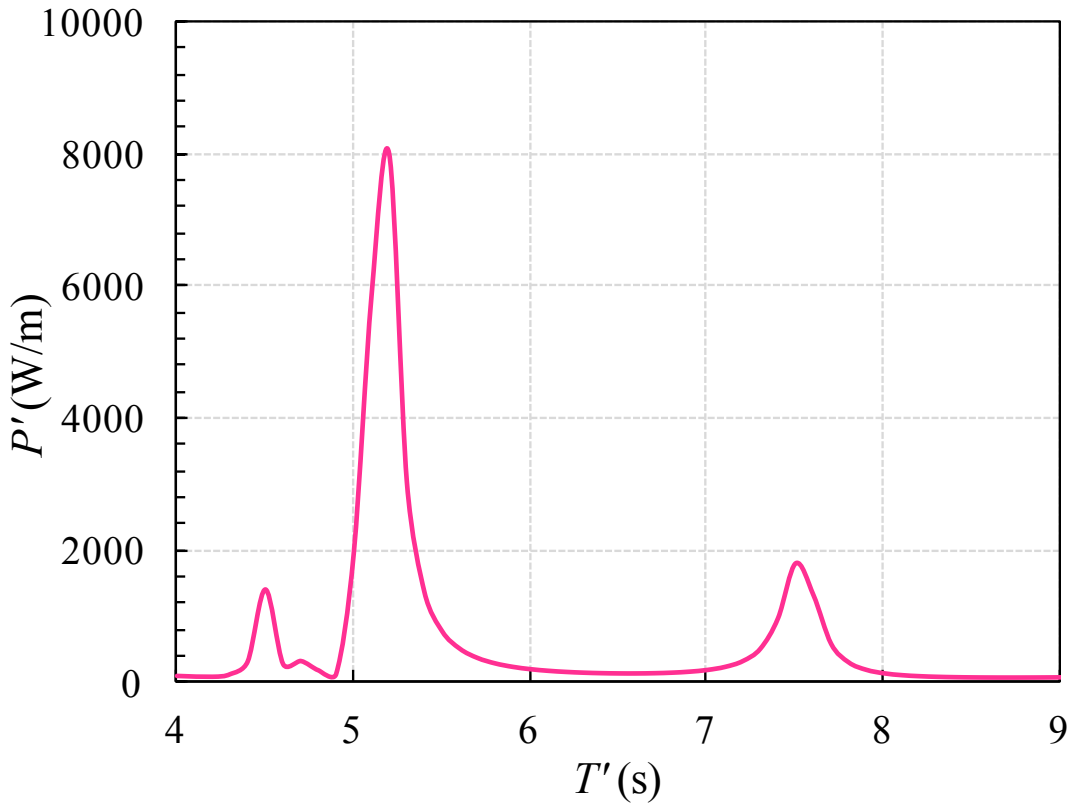

Figure 4.5: Wave power generated by a bimorph piezoelectric plate WECs moored on a caisson breakwater versus the period of the incident wave. The submergence is $d' = 2$ m in a water depth $h' = 10$ m. $\beta = 3.8 \times 10^{-4}$, $\alpha = 0.24$ and $\xi = 1$. The first 18 modes have been considered.

The beneficial effect of using a vertical wall to maximise the power output of a wave energy device was already demonstrated in [43] and in [30] for an oscillating wave energy converter. Therefore in the following section I consider a PWEC which is clamped at both ends to rigid support systems in the ocean, and compare it to the breakwater-PWEC system. I will show that the power output is maximised in the breakwater case, in accordance with the early results for the oscillating WEC. In addition, moorings for wave energy converters have been identified as a major component of the cost for such systems, see [20]. On the other hand, breakwaters are a form of erosion control, don't interfere with the local water

flows and if damage does occur to breakwaters, the maintenance to replace them is very affordable. Therefore the use of a caisson breakwater as mooring system for a PWEC is a smart idea resulting in a reduction in infrastructure costs.

4.2 Flexible piezoelectric wave energy harvester clamped at both ends to rigid support systems in the ocean

The configuration of the PWEC proposed in this section has been analysed by Renzi in [40]. Here we report the basic elements of the theory for the sake of comparison with the breakwater case. As shown in Fig. 4.6 the piezoelectric converter is a flexible plate clamped at both ends to rigid support systems in the ocean. As mentioned at the beginning of chapter 4, initially we define two coordinate systems, one global (x', y', z') and one local on the plate (X', Y', Z') such that $(X', Y', Z') = (x', -y', -z' - d')$. Again, we model deformations of the flexible plates as purely two-dimensional, i.e. $\partial/\partial Y' = 0$ because we assume that the flexible plate width in the transverse direction Y' is much greater than its length $2L'$ along the X' axis.

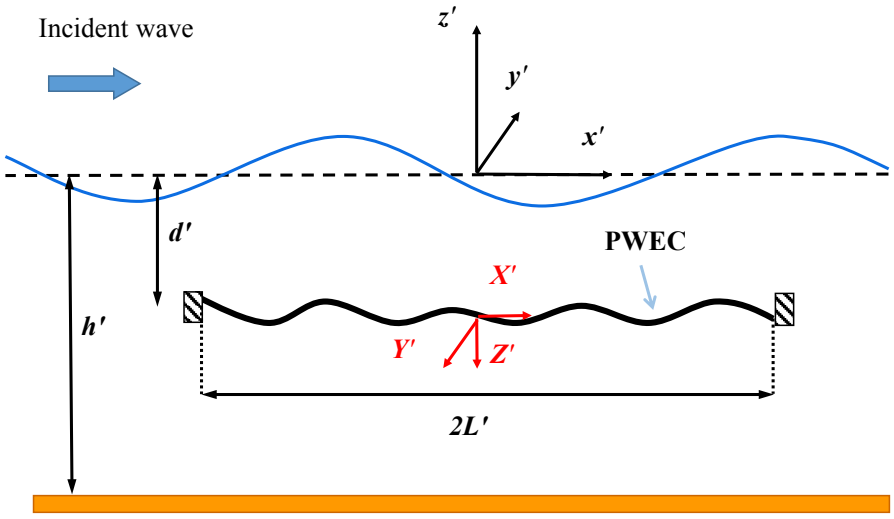

Figure 4.6: Geometry of a double-clamped PWEC in physical variables.

The governing equations of the coupled hydro-electromechanical system are obtained by using a distributed-parameter approach for the piezoelectric plate

(see section 3.3) and a potential-flow theory for the waves (see chapter 2). Since the geometry of the system is different with respect to the PWEC moored on a caisson breakwater, see again Fig. 4.6, we need to take into account different boundary conditions. Hence, the clamping conditions at both ends of the plate (4.12) become

$$W'(\pm L, t) = \left.\frac{\partial W'(x', t')}{\partial x'}\right|_{x'=\pm L'} = 0 \tag{4.53}$$

and the kinematic condition on the surface of the plate (4.14) turns into

$$\frac{\partial W'}{\partial t'} = \frac{\partial \Phi'}{\partial z'}, \qquad |x'| \leq L', \quad z' = -d' \pm \delta, \quad \delta \to 0. \tag{4.54}$$

Also, in the previous configuration we had the boundary condition for the breakwater $\partial\Phi'/\partial x' = 0$ in $x' = 0$, which clearly does not occur in this case. Non-dimensionalisation of equations (4.53) and (4.54) according to (4.5) yields, respectively,

$$W(\pm 1, t) = \left.\frac{\partial W(x, t)}{\partial x}\right|_{x=\pm 1} = 0 \tag{4.55}$$

and

$$\frac{\partial W}{\partial t} = \frac{\partial \Phi}{\partial z} \qquad |x| \leq 1, \quad z = -d \pm \delta, \quad \delta \to 0. \tag{4.56}$$

To obtain the hydro-electromechanical boundary-value problem in terms of the spatial potential ϕ only, we factor out the time variable assuming that the wave forcing is harmonic with frequency ω, so that equation (4.18) can be exploited. Then we substitute (4.18) in the hydrodynamic equations (4.9)-(4.11), into the electro-mechanical equations (4.6)-(4.8) and into the kinematic conditions at the ends of the plate (4.55). Finally, we substitute (4.18) into the kinematic condition on the surface of the plate (4.56) which relates Φ and W. Now we couple equations together. This yields

$$\nabla^2 \phi = 0, \qquad \text{in the fluid domain,} \tag{4.57}$$

$$\phi_z - \omega^2 \phi = 0, \qquad z = 0, \tag{4.58}$$

$$\phi_z = 0, \qquad z = -h, \tag{4.59}$$

$$\beta \left(1 + \frac{\alpha^2 \omega \xi}{i + \omega \xi}\right) \phi_{xxxxz} - \omega^2 \phi_z = \omega^2 r \Delta \phi, \quad |x| \leq 1, \quad z = -d \pm \delta, \quad \delta \to 0, \tag{4.60}$$

$$\phi_z = \phi_{xz} = 0, \quad x = \pm 1, \quad z = -d \pm \delta, \quad \delta \to 0, \tag{4.61}$$

where subscripts denote differentiation with respect to the relevant variable. The above system (4.57)-(4.61) will be solved with the method of matching potentials and appropriate conditions at each of the physical boundaries of the system, see [7, 27, 29, 40]. Fig. 4.7 shows the fluid domain decomposition in four different areas. The following matching conditions at the common boundaries of the four domains will be add to the boundary-value problem (4.57)-(4.61) to find the solution:

$$\phi_{2z} = \phi_{3z}, \qquad |x| \leq 1, \quad z = -d, \tag{4.62}$$

$$\phi_1 = \phi_2, \quad \phi_{1x} = \phi_{2x}, \qquad x = -1 \quad z \in (-d, 0), \tag{4.63}$$

$$\phi_1 = \phi_3, \quad \phi_{1x} = \phi_{3x}, \qquad x = -1 \quad z \in (-h, -d), \tag{4.64}$$

$$\phi_2 = \phi_4, \quad \phi_{2x} = \phi_{4x}, \qquad x = 1 \quad z \in (-d, 0), \tag{4.65}$$

$$\phi_3 = \phi_4, \quad \phi_{3x} = \phi_{4x}, \qquad x = 1 \quad z \in (-h, -d). \tag{4.66}$$

As final condition, we require that the scattered potential in the open ocean areas 1 and 4 is outgoing in the far field [27, 40]. We shall now solve the boundary-

value problem separately in each region and then match the potentials via (4.62)-(4.66).

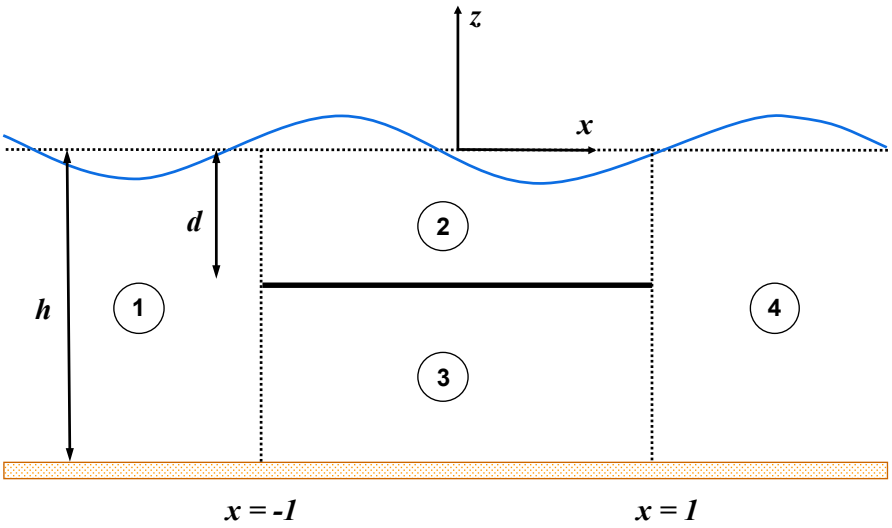

Figure 4.7: Domain decomposition used to solve the boundary-value problem of a double-clamped PWEC.

Regions 1 and 4

In regions 1 and 4 the boundary-value problems for $\phi_1(x,z)$ and $\phi_4(x,z)$, respectively, reduce to (4.57) - (4.59). In particular if we apply the separation of variables rule to (4.19) and we use the boundary conditions (4.58) and (4.59), we can have a solution for $\phi(x,z)$ as product of a function of x and a function of z. Physically, the difference between region 1 and region 4 is the nature of the wave components which describe the situation. Hence, for example, a function of x, which we name $X(x)$ can be written as the superimposition of

$$\underbrace{a_0 e^{ikx}}_{\text{incident wave}} \;, \quad \underbrace{R_0 e^{-ikx}}_{\text{reflected (left-going) wave}} \;, \quad \underbrace{a_n e^{-k_n x}}_{\text{exponentially growing wave}} \;, \quad \underbrace{R_n e^{k_n x}}_{\text{evanescent wave}} \tag{4.67}$$

in region 1 and

$$\underbrace{T_0 e^{ikx}}_{\text{transmitted (right-going) wave}} \;, \quad \underbrace{T_n e^{-k_n x}}_{\text{evanescent wave}} \;, \quad \underbrace{b_n e^{k_n x}}_{\text{exponentially growing wave}} \tag{4.68}$$

in region 4, where a_0, a_n, R_0, R_n, b_n, T_0, T_n are unknown complex coefficients. Also, for physical reasons we need to exclude from the solutions $a_n e^{-k_n x}$ and $b_n e^{k_n x}$ because they are not limited in their domains. On the other end we can choose functions of z same as (4.29), hence the expressions for the spatial potentials in region 1 and 4 are respectively

$$\phi_1(x,z) = -\frac{i}{\omega}\frac{\cosh[k(z+h)]}{\cosh(kh)}e^{ikx} + \sum_{n=0}^{\infty} R_n e^{-i\kappa_n x} Z_n(z), \tag{4.69}$$

where we used equations (2.32) and (2.33) to express a_0, see [27] and

$$\phi_4(x,z) = \sum_{n=0}^{\infty} T_n e^{-i\kappa_n x} Z_n(z), \tag{4.70}$$

where $\kappa_0 = k$ and $\kappa_n = ik_n$ are the solutions of the dispersion relations $\omega^2 = k\ \tanh(kh)$ and $\omega^2 = -k_n\ \tan(k_n h)$ respectively.

Regions 2 and 3

Both ϕ_2 and ϕ_3 must satisfy the Laplace equation (4.57), the condition on the plate (4.60) and the vertical continuity condition (4.62), in addition ϕ_2 must satisfy the surface condition (4.58) while ϕ_3 must satisfy the bottom boundary condition (4.59). We solve simultaneously both systems in regions 2 and 3 and we obtain the same expressions for the spatial potentials $\phi_{2,3}(x,z)$ and the hydro-electromechanical dispersion relation that we derived for the PWEC moored on a breakwater, see equations (4.31) and (4.32).

Amplitude coefficients R_n, T_n, A_n and B_n

Having derived the analytical solution of the boundary-value problem for a PWEC double-clamped to rigid support systems in the ocean coupling EM and HD problems, now we follow the procedure in 4.1.2 to find the numerical values of the complex coefficients R_n, T_n, A_n and B_n, [40]. This will be obtained by solving numerically the matching conditions (4.62)-(4.66). First, we match the potentials substituting the solutions ϕ_1 (4.69), ϕ_2 and ϕ_3 (4.31) into the first conditions of both (4.63) and (4.64). Then, multiply both equations by $Z_m(z)$, $m = 0, 1, ...$, integrate them along z over the respective domains and finally sum the results [40].

This yields

$$R_m = \left[\frac{i}{\omega} \delta_{0m} c e^{-i(k+\kappa_m)} + \sum_{n=-2}^{N} (A_n e^{-i(\sigma_n+\kappa_m)} + B_n e^{i(\sigma_n-\kappa_m)}) b_{mn} \right], \tag{4.71}$$

where $c = [h + \omega^{-2} \sinh^2(kh)]/\sqrt{2}\cosh(kh)$, δ_{0m} is the Kronecker delta and $b_{mn} = \int_{-d}^{0} \psi_n^{(2)}(z) Z_m(z) dz + \int_{-h}^{-d} \psi_n^{(3)}(z) Z_m(z) dz$ is a complex coefficient. Now we match the fluxes (second conditions of both (4.63) and (4.64)) using the same procedure. This yields

$$\frac{k}{\omega} \delta_{0m} c e^{-ik} - i\kappa_m R_m e^{i\kappa_m} = \sum_{n=-2}^{N} i\sigma_n (A_n e^{-i\sigma_n} - B_n e^{i\sigma_n}) b_{mn}, \tag{4.72}$$

with $m = 0, 1, 2, ..., N$. Now we substitute the expression for R_m (4.71) in (4.72) to get

$$-\frac{i}{\omega}(k + \kappa_m) \delta_{0m} c e^{-ik} = \sum_{n=-2}^{N} [A_n e^{-i\sigma_n}(\sigma_n + \kappa_m) - B_n e^{i\sigma_n}(\sigma_n - \kappa_m)] b_{mn}, \tag{4.73}$$

$m = 0, 1, 2, ..., N$. With the same procedure, we match fluxes and potentials at the common boundary between regions 2 and 4, 3 and 4 (first and second conditions of equations (4.65) and (4.66)) to obtain

$$T_m = \sum_{n=-2}^{N} [A_n e^{i(\sigma_n-\kappa_m)} + B_n e^{-i(\sigma_n+\kappa_m)}] b_{mn}, \tag{4.74}$$

with $m = 0, 1, 2, ..., N$ and

$$\sum_{n=-2}^{N} [A_n e^{i\sigma_n}(\sigma_n - \kappa_m) - B_n e^{-i\sigma_n}(\sigma_n + \kappa_m)] b_{mn} = 0, \tag{4.75}$$

with $m = 0, 1, 2, ..., N$. Looking at equations (4.71), (4.73)-(4.75), note that once the A_n and B_n are determined, the R_n and T_n can be found using (4.71) and (4.74), respectively. To obtain numerical values of the A_n and B_n we can use expressions (4.73) and (4.75), but at this point we have $2(N+1)$ equations in $2(N+3)$ unknows, therefore we need four additional equations to close the system. These are provided by the clamping conditions on the plate (4.61) which we have

not used yet, [40]. Substituting either ϕ_2 or ϕ_3 into (4.61), we get

$$\sum_{n=-2}^{N}(A_n e^{-i\sigma_n} + B_n e^{i\sigma_n})f_n = 0, \tag{4.76}$$

$$\sum_{n=-2}^{N}(A_n e^{i\sigma_n} + B_n e^{-i\sigma_n})f_n = 0, \tag{4.77}$$

$$\sum_{n=-2}^{N}(A_n \sigma_n e^{-i\sigma_n} - B_n \sigma_n e^{i\sigma_n})f_n = 0, \tag{4.78}$$

$$\sum_{n=-2}^{N}(A_n \sigma_n e^{i\sigma_n} - B_n \sigma_n e^{-i\sigma_n})f_n = 0, \tag{4.79}$$

[40], where f_n is given in (4.41). The system (4.73), (4.75)-(4.79) can now be solved numerically with a suitable choice of N. The numerical solution and all the quantities of engineering interest have been obtained implementing a Matlab code. In the framework of this thesis, we are interested, for example, in comparing the result of the average power extracted (4.49) from both the PWEC configurations described. Therefore we select a typical plate configuration for the piezoelectric wave energy harvester clamped at both ends to rigid support systems in the ocean. Referring to figure 4.6, the length of the plate is $2L' = 20$ m, the water depth is h' $= 10$ m and the submergence of the plate is $d' = 2$ m. In addition we assume that the amplitude of the ocean surface waves is $A' = 1$ m and the bimorph piezoelectric plate is characterised by: silicone rubber layer (substrate) of thickness $d'_0 = 0.01$ m, polyvinylidene fluoride (PVDF) piezoelectric layers of thickness $d'_p = 1.1 \times 10^{-4}$ m, [40]. Typical values of the system coefficients for commercial silicone rubber and PVDF are shown in the following Tab. 4.3, see e.g. [16, 17, 40, 44].

Table 4.3: Silicone rubber and PVDF coefficients for a PWEC clamped at both ends to rigid support systems in the ocean.

Stiffness	**Piezoelectric coupling parameter**	**Resistive term**
β	α	ξ
3.8×10^{-4}	0.21	1

To predict the power generated from the double-clamped PWEC above, we use the linearised theory derived in the subsection 4.1.2. Hence, the average extracted

power per unit width is expressed by equation (4.49), whose behaviour is shown in Fig. 4.8 with respect to the period of the incident waves. Although capture width ratio (CRW) has been used widely to assess the performance of wave energy devices, it is not a physically meaningful indicator for a 2D device of infinite length such as the one considered in this work. As already seen before for the case of the PWEC moored on a vertical wall, the hydro-electromechanical behaviour of the device causes sharp resonant peaks in the generated power. Here we consider 13 vibrational modes (because of a faster level of convergence of this model with respect to the one of the PWEC moored on a breakwater) and we identify the existence of 4 resonant periods in the interval [4-9] s with a maximum peak of about 4.4 kW/m at $T' \simeq 5.4$ s. Note that this value is about half the power output of a half-length (L'= 10 m) bimorph piezoelectric plate WEC moored on a caisson breakwater, see again Fig. 4.5. Hence, the effect of the breakwater on the power output of the system is extremely beneficial, as it allows one to extract roughly twice the amount of energy, but using half the material, of a system without breakwater.

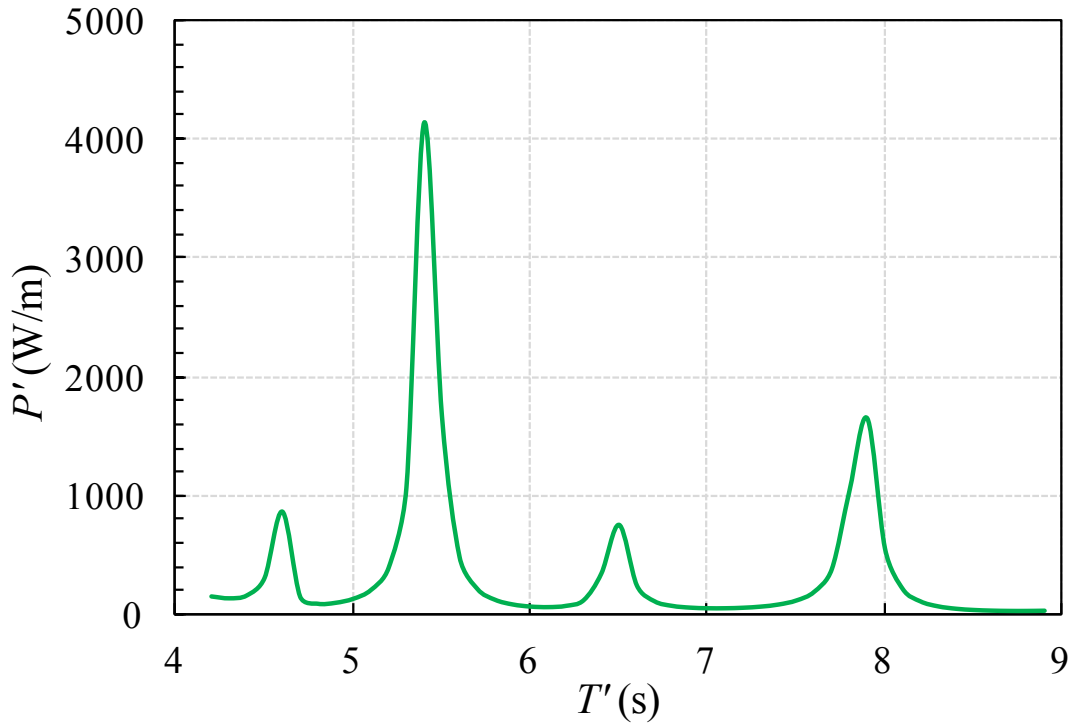

Figure 4.8: Wave power generated by a bimorph piezoelectric plate WECs clamped at both ends to rigid support systems in the ocean versus the period of the incident wave. The submergence is $d' = 2$ m in a water depth $h' = 10$ m. $\beta = 3.8 \times 10^{-4}$, $\alpha = 0.21$ and $\xi = 1$. The first 13 modes have been considered.

4.3 Convergence tests

Here, I provide some considerations on the numerical solution of the linear system of equations (4.33), (4.36), (4.37)-(4.40) which describe the hydro-electromechanical model for the PWEC moored on a breakwater analysed in section 4.1. The numerical solution has been obtained by truncating the series expansions up to a suitable number of terms, N. To determine an appropriate value for N in our numerical calculations, I performed a convergence test by analysing the influence of N on the power output of the system $\mathcal{P}$ (4.49). To assess convergence I calculated the relative error at the nth numerical iteration as

$$\epsilon_n = \frac{|\mathcal{P}_{n+1} - \mathcal{P}_n|}{\max\{|\mathcal{P}_{n+1}|, |\mathcal{P}_n|\}}. \tag{4.80}$$

The major convergence problems occur around the resonant periods of the device, at which the power output is significant, as shown in Fig. 4.9. The plot

shows the behaviour of the power output of the system for two different values of N versus the period of the incident wave.

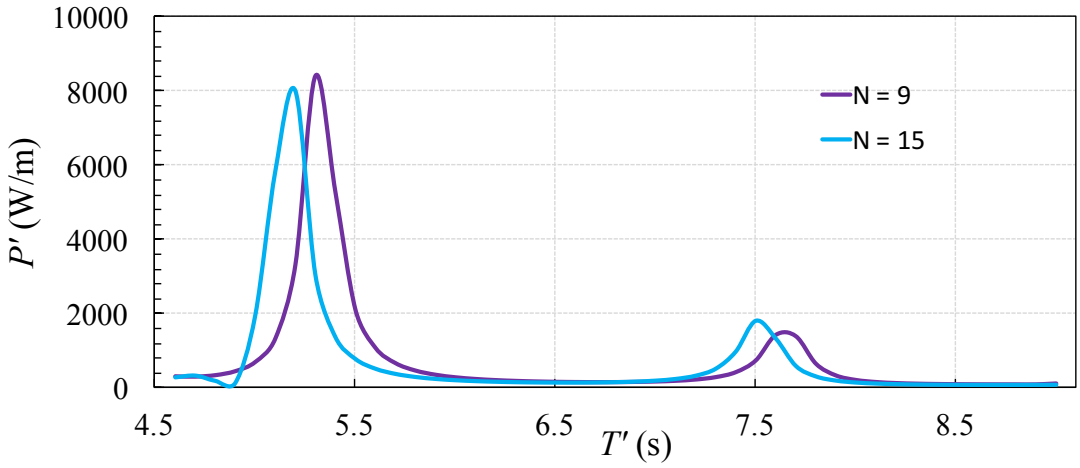

Figure 4.9: Behaviour of the average extracted power by the device versus the period of the incident waves considering two different values of N. There is a visible good convergence in the power output far from the resonant peaks between $N = 9$ and $N = 15$. On the other end, convergence tests need to be carried on around the resonant periods of the device.

Note that there is practically no visible difference between the cases N = 9 and N = 15 far from the peaks. In fact the maximum error ϵ_N in the interval $[6 - 7]$ s is of the order of $O(10^{-2})$ and this trend is maintained for any values of N between 9 and 16. However, to select a suitable value of N, the convergence around the peaks needs to be further investigated.

Fig. 4.10 shows the relative error of the wave power generated around the maximum resonant peak at the $15th$ numerical iteration (i.e. $\epsilon_{15} = |\mathcal{P}_{16} - \mathcal{P}_{15}|/\max\{|\mathcal{P}_{16}|, |\mathcal{P}_{15}|\}$) versus the period of the incident wave. The average error in the interval $[5 - 6]$ s is of the order of $O(10^{-2})$. The latter is accurate enough for graphical purposes in all cases considered here. Hence N = 15 provides an adequate level of convergence. That corresponds to considering up to 18 flexural modes on the plate, $n = -2, -1, ..., 15$.

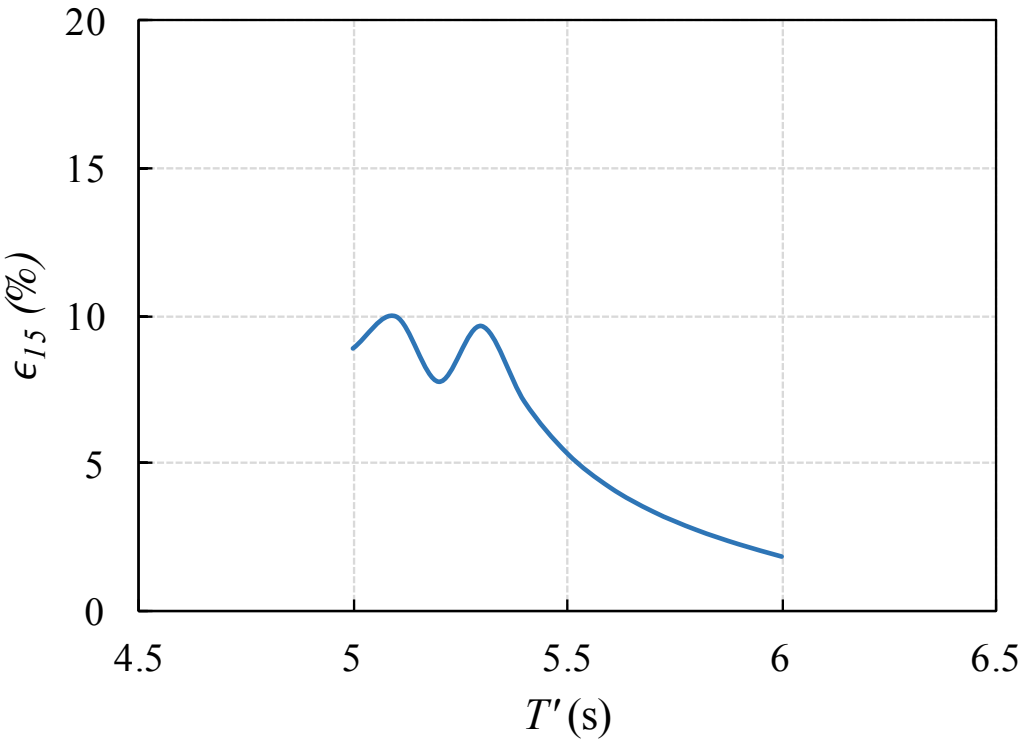

Figure 4.10: Relative error ϵ_{15} of the output power generated around the maximum resonant peak by a bimorph PWEC moored on a caisson breakwater versus the period of the incident wave. $N = 15$ and $N = 16$ have been considered for a convergence test. The average error in the interval $[5 - 6]$ s is of the order of $O(10^{-2})$.

4.3.1 Approach to a parametric analysis: water depth

Another example of convergence test has been undertaken at the beginning of a parametric analysis whose purpose was to find the optimal device configuration. In particular, first, I wanted to investigate the behaviour of the power output of the system, mooring the PWEC on a caisson breakwater at different water depths, d'. Since the resonant periods of the device are the most delicate areas in terms of convergence analysis, numerically, I solved the linear system (4.33), (4.36), (4.37)-(4.40) around the maximum peak of the extracted power. Hence, I selected the periods of the incident wave in the interval $[5 - 6]$ s and compared the power behaviour obtained in subsection 4.1.3 with the power extracted from a PWEC characterised by the same geometry but a lower mooring depth. Fig. 4.11 shows the wave power generated around the maximum resonant peak by two flexible piezoelectric energy harvesters moored on a caisson breakwater at different water

depths, $d' = 2$ m and $d' = 4$ m.

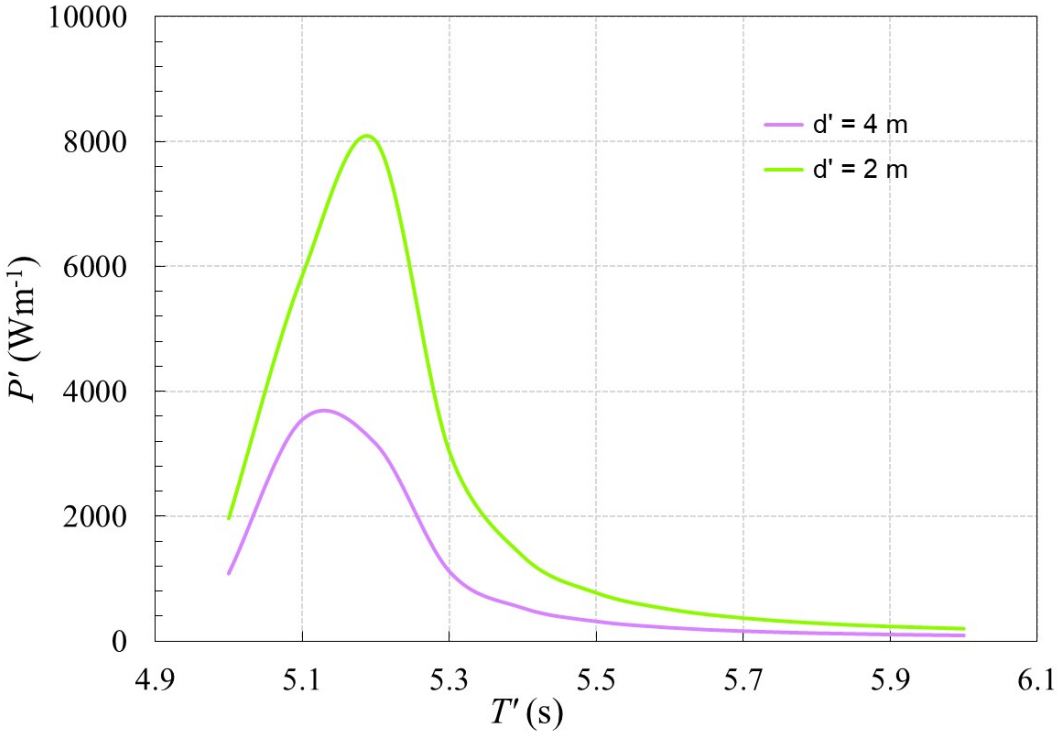

Figure 4.11: Wave power generated around the maximum resonant peak by two bimorph piezoelectric plate WECs moored on a caisson breakwater versus the period of the incident wave. The length of the plates is $L' = 10$ m and the water depth is $h' = 10$ m. The green line identifies the PWEC moored at $d' = 2$ m (the first 18 modes have been considered), while the violet line corresponds to the same PWEC moored at $d' = 4$ m (the first 19 modes have been considered). Note that comparing the power generated at both the maximum peaks, we observe a significant drop of the performance of the device.

As expected, there is a significant drop of the performance of the device when the mooring depth increases because of the reduction of the amplitude of the progressive waves travelling along the plate. The violet curve has been obtained by truncating the series expansions of the linear system (4.33), (4.36), (4.37)-(4.40) up to $N = 16$ because, as shown in Fig. 4.12, the convergence test denotes an accurate agreement between the cases $N = 16$ and $N = 17$ with a maximum error of 2%. In the plot there is practically no visible difference between the two curves, so that $N = 16$ provides an adequate level of convergence. That corresponds to considering up to 19 flexural modes on the plate, $n = -2, -1, ..., 16$, see again Fig. 4.11.

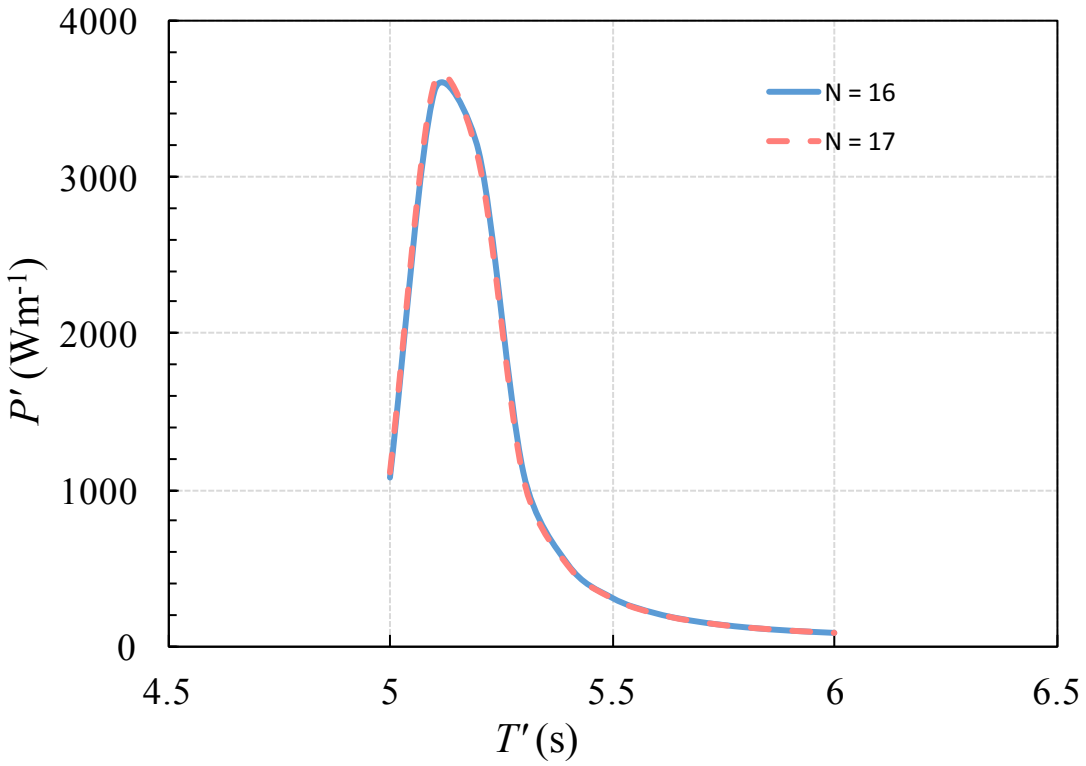

Figure 4.12: Detail of the wave power generated around the maximum resonant peak by a bimorph PWEC moored on a caisson breakwater at a water depth $d' = 4$ m versus the period of the incident wave. $N = 16$ and $N = 17$ have been considered for a convergence test. The maximum error in the interval $[5 - 6]$ s is of the order of $O(10^{-2})$.

Despite these preliminary good results, I need to point out some difficulties in finding a correct solution for the linear system of equations (4.33), (4.36), (4.37)-(4.40) in the case of $d' = 4$ m. In particular, I am dealing with a quasi-singular matrix which generates a badly conditioned problem and loss of numerical precision. This means that if I change the initial data, even by a tiny bit, I obtain very different results. Hence, the eigenvalues σ_n, solutions of the hydro-electromechanical dispersion relation $F(\sigma_n) = 0$, see (4.32), sometimes correspond to totally wrong values that cannot be accepted. This happens mainly because the method I used to solve equation (4.32), i.e. a two-dimensional Newton-Raphson method, on one side allows to easily obtain all the quantities of engineering interest and clearly demonstrate the feasibility of the device, but on the other hand, it is based on the function $F(\sigma_n)$, its derivative $F'(\sigma_n)$ and an initial guess (a grid points). First of all, the expression for $F(\sigma_n)$ include multiplications between hyperbolic sines (or cosines) (very big terms), and negative exponentials (very small terms) which is

not easy to compute numerically to a high order of precision with Matlab. But above all, the initial grid has a fundamental role in terms of both grid dimensions and grid spacing. The grid I am concerned with is in the complex σ_n plane already seen in Fig. 4.4. Every time I run the Matlab code to obtain the eigenvalues σ_n, I need to specify an initial input to the code that consists of giving dimensions and spacing of a suitable sub-domain in complex plane, both along the horizontal and the vertical directions. Tab. 4.4 shows an example of how the initial grid can badly affect the convergence of the numerical solutions of the system (4.33), (4.36), (4.37)-(4.40). Case 1 and case 2 are obtained changing the grid dimension and the spacing along the vertical axes $\Im\{\sigma_n\}$. In particular setting a maximum value of $\Im\{\sigma_n\} = 30$ with a spacing of 100, yields numerical eigenvalues reported in case 1, while changing the maximum value of $\Im\{\sigma_n\}$ to 51 with a spacing of 300, yields numerical eigenvalues reported in case 2, see second and third column of Tab 4.4, respectively. As a result of a dense grid, solutions of the dispersion relation (4.32) which are close to each other, converge on the same eigenvalues, therefore I obtain repeated eigenvalues (which are subsequently discarded by the Matlab code in order to proceed with the analysis). This happens for both sets of data, but in case 2, the grid is bigger and denser. In this case I get more eigenvalues (all values of case 1 plus new ones), therefore the power output of the system is different, i.e. about 9.7 kW/m against 17.1 kW/m obtained in case 1. The first 24 and 33 flexural plate modes have been considered respectively in case 1 and 2. Note that, despite considering high modes ($N > 16$), the convergence of the results is still very slow and the power output of the system keeps changing considerably.

In addition to this analysis, mathematically, I used the method of matching potentials as in [7, 29, 40]. Hassan, Meylan [29] and Renzi [40] already pointed out that the eigenfunction-matching method does not have an optimal convergence because of the square-root singularity at the plate edge [25]. In fact, even in the case of $d' = 2$ m, I noted pretty slow convergence rates. An improvement of the method used to solve the dispersion relation (4.32) could be to use numerical optimisation methods. I have tried to use Matlab Optimization Toolbox but with unsatisfactory results. Also, the eigenvalues σ_n could be calculated still

Table 4.4: Numerical values of the complex eigenvalues σ_n obtained solving the dispersion relation (4.32) with different grid dimension and spacing along the vertical axes $\Im\{\sigma_n\}$. Parameters are: $A' = 1$ m, $T' = 4$ s, $d' = 4$ m, $\alpha = 0.24$, $\beta = 3.8 \times 10^{-4}$, $\xi = 1$. Grid characteristic are as follows. Case 1: Max $\Im\{\sigma_n\} = 30$, grid spacing along $\Im\{\sigma_n\} = 100$. Case 2: Max $\Im\{\sigma_n\} = 51$, grid spacing along $\Im\{\sigma_n\} = 300$.

Eigenvalue	**Numerical Value - case 1**	**Numerical Value - case 2**
σ_{-2}	7.8388 -23.8984i	7.8388 -23.8984i
σ_{-1}	0.5694 -20.1779i	0.5694 -20.1779i
σ_0	0.5694 -20.1779i	0.5694 -20.1779i
σ_1	1.6049 -19.3985i	0.5694 -20.1779i
σ_2	1.6049 -19.3985i	1.6049 -19.3985i
σ_3	1.6049 -19.3985i	1.6049 -19.3985i
σ_4	1.6049 -19.3985i	1.6049 -19.3985i
σ_5	2.5479 + 0.0000i	1.6049 -19.3985i
σ_6	25.1957 + 0.1412i	1.6049 -19.3985i
σ_7	0.0000 + 2.3110i	2.5479 + 0.0000i
σ_8	0.0000 + 5.8779i	25.1957 + 0.1412i
σ_9	0.0002 + 9.1574i	0.0000 + 2.3110i
σ_{10}	0.0014 +12.4018i	0.0000 + 5.8779i
σ_{11}	0.0000 +15.5490i	0.0002 + 9.1574i
σ_{12}	0.0139 +19.1648i	0.0014 +12.4018i
σ_{13}	1.5773 +19.3884i	0.0000 +15.5490i
σ_{14}	1.5773 +19.3884i	0.0139 +19.1648i
σ_{15}	1.5773 +19.3884i	1.5773 +19.3884i
σ_{16}	1.5773 +19.3884i	1.5773 +19.3884i
σ_{17}	1.5773 +19.3884i	1.5773 +19.3884i
σ_{18}	0.6098 +20.1940i	1.5773 +19.3884i
σ_{19}	0.0092 +22.1838i	1.5773 +19.3884i
σ_{20}	7.5728 +23.9848i	0.6098 +20.1940i
σ_{21}	0.0104 +25.6324i	0.0092 +22.1838i
σ_{22}		7.5728 +23.9848i
σ_{23}		0.0104 +25.6324i
σ_{24}		0.0214 +30.5280i
σ_{25}		0.0003 +31.3487i
σ_{26}		0.0040 +36.5173i
σ_{27}		0.0039 +38.9709i
σ_{28}		0.0018 +41.8241i
σ_{29}		0.0022 +46.9228i
σ_{30}		0.0004 +47.0998i

using a Newton-Raphson method but with an analitical approach to derive the Jacobian matrix instead of a numerical one. Another possibility is to change model completely in favour of a different approach based on the so-called "dry modes" of the system, for which there is no need to solve the dispersion relation [33].

However, to the best of my knowledge, to date there is no available application of the method to coupled piezo-electric problems. Finally, the convergence issues related to the singularity at the tip could be overcome by developing a new model based on integral equations as shown in the next section for the FBWEC.

Chapter 5

Floater Blanket Wave Energy Converter

In this section, I analyse a novel wave-structure interaction problem whose macro structure is similar to a flexible carpet which I name Floater Blanket (FB). The common feature with the flexible piezoelectric devices of sections 4.1 and 4.2 is the overall shape of a plate, in the sense that the thickness in the vertical direction of both FB and P devices is much smaller than their dimensions (length and width) in the other two directions. However the PWEC is a flexible plate characterised by a bimorph configuration of the piezoelectric material, in which piezoelectric patches are attached on both sides of an elastic substrate. In addition the power take-off (PTO) system is in the piezoelectric material itself because of its ability to generate an electric potential when deformed due to vibrations (sensor effect). On the other hand, the floater blanket wave energy converter (FBWEC) consists of a grid of interconnected floater elements with each floater being connected to a piston-type hydraulic pumping system (a multi-piston pump) as shown in Fig. 5.1. Each single element works similarly to a point-absorber which absorbs wave energy through its vertical movements at the water surface. The relative motion between the wave-activated float on the sea surface and a support structure activates a PTO system. Also the FB device floats on the free surface while both the PWECs studied in this thesis are clamped at a certain water depth d', see agin Fig. 4.1. The movement of a single hinged floater affects inevitably the behaviour of the whole system generating a complex wave-structure interaction problem. Therefore, in the

framework of this thesis, I derive and solve the radiation problem for a single row of interconnected floater elements of a FBWEC, considering a two-dimensional analysis as the first step to approach the hydrodynamic characterisation of the whole floater blanket. This will form the basis for the study of a 3D case.

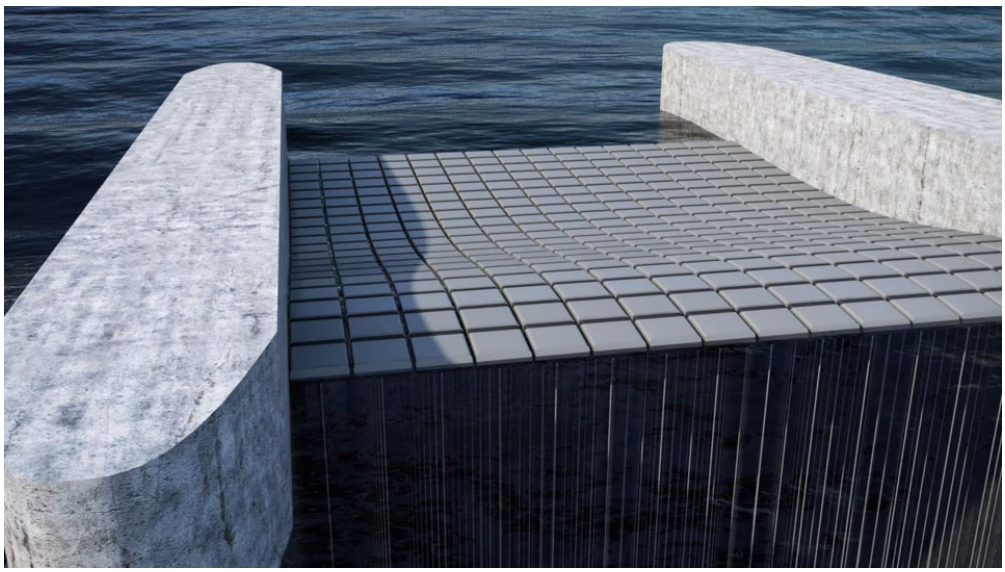

Figure 5.1: The floater blanket designed by the University of Groningen as part of the Ocean Grazer massive platform, [3].

A wave train incident upon a floating structure will set the structure in motion to produce a radiated field and also will be scattered to produce a diffracted wave field [25, 27]. By linear superposition, the velocity potential may be decomposed into two parts as

$$\Phi' = \Phi'_R + \Phi'_D. \tag{5.1}$$

The potential Φ'_R is the solution of the radiation problem in which the structure is forced to oscillate in the absence of an incident wave, see following section. The potential Φ'_D is the solution of the diffraction problem in which the structure is held fixed in incident waves and it may be further decomposed as

$$\Phi'_D = \Phi'_I + \Phi'_S, \tag{5.2}$$

where Φ'_I represents the incident wave train and Φ'_S the scattered waves. In the framework of this thesis, I analyse wave-structure interactions solving the

radiation problem and leaving details of the diffraction problem in appendix D for further research developments.

Let me consider the vertical movement of a single generic floater element, which I name m, hence the two-dimensional geometry of the system is as shown in Fig. 5.2. I limit the analysis to two-dimensional effects. Referring to Fig. 5.2, I define a two-dimensional coordinate system (x', z'), in which the z'-axis points upwards from the undisturbed water level $z' = 0$. The x'-axis is directed along the direction of propagation of incoming waves of amplitude A' and frequency ω'. Variables with primes denote again physical quantities. The bottom of the ocean is located at a constant depth $z' = -h'$ and the device is floating on the free surface in correspondence of an ocean step characterised by a height of c', while a' is the submergence of the device. Moreover, without loss of generality, I assume that the first and the last floaters are fixed. For example, they could represent mooring points of the system.

This chapter presents a two-dimensional analytical model derived for the FB-WEC of Fig. 5.2 and it is organised as follows. First I decompose the frequency-domain problem in the radiation and diffraction potentials problems. I derive and solve the radiation problem in the internal region by splitting the fluid domain in three different areas and using the matching conditions at the common boundaries of the three domains (section 5.1). Then, I derive and solve the radiation problem in the external regions by using a solution method based on the integral equations (section 5.2). Hence, I apply the law of conservation of mass flow rate in the fluid volume in the internal region to obtain the continuity equation (section 5.4) so that I have a well-posed boundary-value radiation problem (section 5.5), whose numerical solutions are identified developing suitable Matlab programs, see chapter 6.

In appendix B I derive an alternative approach based on a suitable Bessho-Newman relation obtained applying Green's theorem to the radiation and diffraction problems. This method can be used in substitution of the continuity equation and considerations on symmetry arguments derived in section 5.4. However, this implies the analysis and solution of the diffraction problem (appendix D), which inevitably makes the solution procedure more onerous.

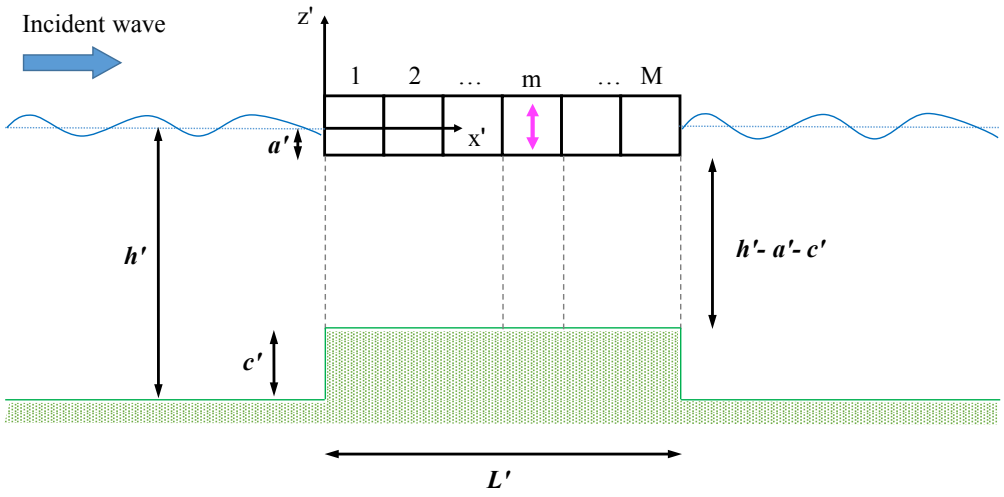

Figure 5.2: Geometry of the FBWEC system in physical variables.

5.1 Radiation: internal

Let me consider the vertical movement of the element m in the z' direction as schematically shown in Fig. 5.3. In the following, the subscript m denotes the dependance from the movement of the m element. From now on primes will be dropped for simplicity in the whole chapter.

The dynamic of the system, which consists of ocean surface waves and floater blanket is described according to the theory developed in chapter 2. Due to linearity, I expand the potential as $\sum_{m=1}^{M} V_m \Phi_m$, where V_m is the unknown vertical velocity of the m-th element, and Φ_m is the relevant potential. I solve the radiation problem in the internal region by splitting the fluid domain in three different areas and applying the matching conditions at the common boundaries of the three domains. Note that the method applied here, i.e. matching potentials has been used also to derive the boundary-value problem for both the piezoelectric WECs and the slow convergence rate due to the plate edge has been already pointed out, see 4.3. Nevertheless, in this case, I deal with a 'smooth' fluid domain since there are no edges or tips in the internal region, therefore the matching potentials method represents a good choice to derive a well-posed boundary-value problem to describe the radiation of the FBWEC system in the internal region.

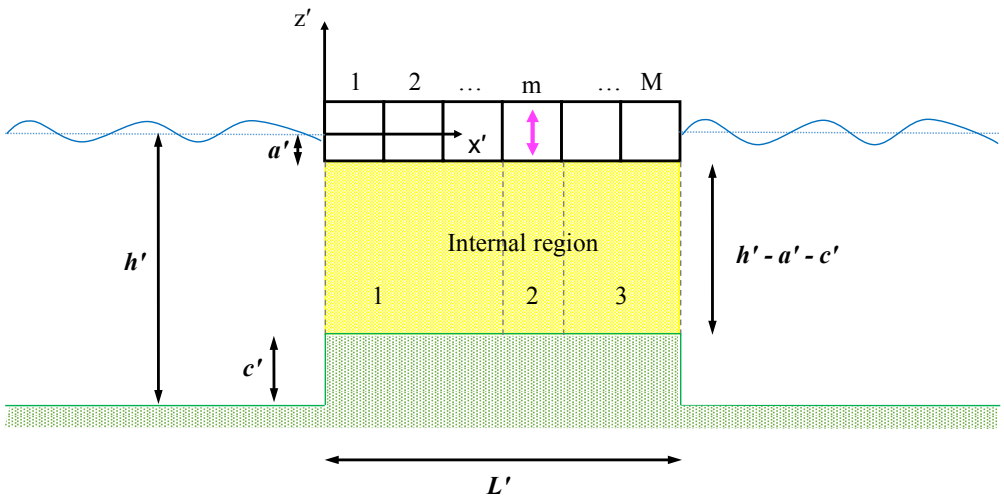

Figure 5.3: Geometry of the FBWEC system with emphasis on the internal region (yellow) which corresponds to the fluid domain below the floating device and above ocean step. Moreover, the internal region is split in three subareas regarding the position of the m-th floater.

5.1.1 Governing equations

In the following subsection I make a list of the governing partial differential equations for the problem described in Fig. 5.3:

$$\nabla^2 \Phi_m^{(1,2,3)} = 0, \qquad 0 < x < L, \qquad -h + c \leq z \leq -a, \tag{5.3}$$

$$\Phi_{mz}^{(1,2,3)} = 0, \qquad 0 < x < L, \qquad z = -h + c, \tag{5.4}$$

$$\Phi_{mz}^{(1)} = 0, \qquad x_0 < x < x_{m-1}, \qquad z = -a, \tag{5.5}$$

$$\Phi_{mz}^{(2)} = 1, \qquad x_{m-1} < x < x_m, \qquad z = -a, \tag{5.6}$$

$$\Phi_{mz}^{(3)} = 0, \qquad x_m < x < L, \qquad z = -a, \tag{5.7}$$

where $\Phi_m^{(i)}$ is the potential in region $i = 1, 2, 3$.

5.1.2 Expressions for the internal potentials

The wave forcing is harmonic with frequency ω, so I use (4.18) to factor out the time variation: $\Phi_m^{(1,2,3)} = \Re\{\phi_m^{(1,2,3)}(x,z)e^{-i\omega t}\}$. To find solutions in terms of the spatial potential $\phi_m(x,z)$, I consider $\phi_m(x,z) = X(x)Z(z)$ so that

$$\nabla^2\phi_m = \phi_{mxx} + \phi_{mzz} = X_{xx}Z + Z_{zz}X,$$

(separation of variables). Now, solving the separated equations, I obtain

$$X(x) = A_m e^{ikx} + B_m e^{-ikx}$$

and

$$Z(z) = a_m \cosh[k(z+h-c)] + b_m \sinh[k(z+h-c)],$$

hence $\phi_m^{(1)}$ is expressed by

$$\phi_m^{(1)}(x,z) = (A_m e^{ikx} + B_m e^{-ikx})[a_m \cosh k(z+h-c)] + b_m \sinh k(z+h-c)], \quad (5.8)$$

where A_m, B_m, a_m and b_m are integration constants. I use equation (5.4) and I obtain $b_m = 0$, then (5.5) gives me a condition on k, when $x_0 \leq x \leq x_{m-1}$:

$$k \sinh[k(h-a-c)] = 0. \quad (5.9)$$

The latter admits a real solution for k if and only if $k = 0$. To find possible complex solutions, I analyse the equation (5.9) in the complex plane. Substitute $k = i\tilde{k}$ to get

$$i\tilde{k} \sinh[i\tilde{k}(h-a-c)] = 0, \quad (5.10)$$

from which I obtain our condition on $\tilde{k}$:

$$\tilde{k}_p = \frac{p\pi}{h-a-c}, \qquad p = 1, 2, 3... \quad (5.11)$$

Therefore,

$$\phi_m^{(1)}(x,z) = A_{0m}x + B_{0m} + \sum_{p=1}^{+\infty}(A_{pm}e^{-\tilde{k}_p x} + B_{pm}e^{\tilde{k}_p x})\cos[\tilde{k}_p(z+h-c)], \quad (5.12)$$

with $x_0 \leq x \leq x_{m-1}$. Following the same procedure for the problem described by the equations (5.3), (5.4) and (5.7), I obtain

$$\phi_m^{(3)}(x,z) = C_{0m}(x-L) + D_{0m} + \sum_{p=1}^{+\infty}(C_{pm}e^{-\tilde{k}_p(x-L)} + D_{pm}e^{\tilde{k}_p(x-L)}) \cos[\tilde{k}_p(z+h-c)], \quad x_m \leq x \leq L. \quad (5.13)$$

Now, let me turn to region 2. Since (5.6) is a non-homogeneous partial differential equation, to get an expression for the spatial velocity ϕ_m in region 2, I follow the method used by Linton and McIver, see [25]. I assume that $\phi_m^{(2)}$ can be written as the sum of homogeneous and particular solutions, i.e. $\phi_m^{(2)} = \phi_{mh}^{(2)} + \overline{\phi}_m^{(2)}$. I can find the expression for $\phi_{mh}^{(2)}$ as I did for regions 1 and 3:

$$\phi_{mh}^{(2)}(x,z) = E_{0m}x + F_{0m} + \sum_{p=1}^{+\infty}(E_{pm}e^{-\tilde{k}_p x} + F_{pm}e^{\tilde{k}_p x})\cos[\tilde{k}_p(z+h-c)]. \quad (5.14)$$

To obtain the expression for the particular solution $\overline{\phi}_m^{(2)}$ I use the equation for a straight line connecting two points ($\overline{\phi}_{mz}^{(2)} = 0, z = -h+c$) and ($\overline{\phi}_{mz}^{(2)} = 1, z = -a$) which come directly from equations (5.4) and (5.6). Fig. 5.4 may help to figure out the schematic situation.

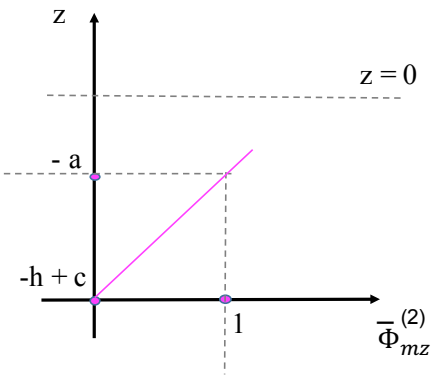

Figure 5.4: Schematic sketch used to get an expression for the particular solution $\overline{\phi}_m^{(2)}$ in the region 2. Graphic expression for a straight line given the following two points: $(\overline{\phi}_{mz}^{(2)} = 0, z = -h + c)$ and $(\overline{\phi}_{mz}^{(2)} = 1, z = -a)$.

This gives

$$\overline{\phi}_{mz}^{(2)} = \frac{z + h - c}{h - a - c}.$$

Integrating $\overline{\phi}_{mz}^{(2)}$ along z and using equation (5.3), I get

$$\overline{\phi}_m^{(2)}(x, z) = \frac{(z + h - c)^2 - (x - x_{m-1})(x - x_m)}{2(h - a - c)}, \tag{5.15}$$

so that the full solution in region 2 is

$$\phi_m^{(2)}(x, z) = E_{0m}x + F_{0m} + \sum_{p=1}^{+\infty}(E_{pm}e^{-\tilde{k}_p x} + F_{pm}e^{\tilde{k}_p x})\cos[\tilde{k}_p(z + h - c)] + \frac{(z + h - c)^2 - (x - x_{m-1})(x - x_m)}{2(h - a - c)}, \quad x_{m-1} \leq x_m. \tag{5.16}$$

5.1.3 Amplitude coefficients

Having obtained the expressions for $\phi_m^{(1)}, \phi_m^{(2)}$ and $\phi_m^{(3)}$, see respectively (5.12), (5.13) and (5.16), I am now in a position to express the amplitude coefficients A_{pm}, B_{pm}, C_{pm} and D_{pm} in terms of E_{pm} and F_{pm} and A_{0m}, B_{0m}, C_{0m} and D_{0m} in terms of E_{0m} and F_{0m} and A_{0m}, B_{0m}, C_{0m} and D_{0m} in terms of E_{0m} and F_{0m} by using the following matching conditions at the common boundaries of the three

internal domains:

$$\phi_m^{(1)} = \phi_m^{(2)}, \qquad \phi_{mx}^{(1)} = \phi_{mx}^{(2)}, \qquad x = x_{m-1}, \quad z \in (-h+c,\ -a), \tag{5.17}$$

$$\phi_m^{(2)} = \phi_m^{(3)}, \qquad \phi_{mx}^{(2)} = \phi_{mx}^{(3)}, \qquad x = x_m, \quad z \in (-h+c,\ -a), \tag{5.18}$$

where the $\phi_m^{(i)}$ denote the potential ϕ in each area $i = 1, 2, 3$ when the m-th element of the FBWEC moves along the z-direction with unit velocity. First, substitute the solutions $\phi_m^{(1)}$ (5.12) and $\phi_m^{(2)}$ (5.16) into the first condition of (5.17). Then, multiply by $\cos[\tilde{k}_q(z+h-c)]$ with $q = 1, 2, ...$, integrate along z between $z = -h+c$ and $z = -a$ to obtain

$$A_{pm}e^{-\tilde{k}_p x_{m-1}} + B_{pm}e^{\tilde{k}_p x_{m-1}} = E_{pm}e^{-\tilde{k}_p x_{m-1}} + F_{pm}e^{\tilde{k}_p x_{m-1}} + \frac{2(-1)^p}{\tilde{k}_p^2(h-a-c)}. \tag{5.19}$$

In the latter, the orthogonality of the cosines has been exploited and $p = 1, 2, ...$ Using the same procedure, from the second condition of (5.17) and from (5.18) I obtain, respectively,

$$A_{pm}e^{-\tilde{k}_p x_{m-1}} - B_{pm}e^{\tilde{k}_p x_{m-1}} = E_{pm}e^{-\tilde{k}_p x_{m-1}} - F_{pm}e^{\tilde{k}_p x_{m-1}}, \tag{5.20}$$

$$C_{pm}e^{-\tilde{k}_p (x_m - L)} + D_{pm}e^{\tilde{k}_p (x_m - L)} = E_{pm}e^{-\tilde{k}_p x_m} + F_{pm}e^{\tilde{k}_p x_m} + \frac{2(-1)^p}{\tilde{k}_p^2(h-a-c)} \tag{5.21}$$

and

$$C_{pm}e^{-\tilde{k}_p (x_m - L)} - D_{pm}e^{\tilde{k}_p (x_m - L)} = E_{pm}e^{-\tilde{k}_p x_m} - F_{pm}e^{\tilde{k}_p x_m}. \tag{5.22}$$

Hence I can solve the system of equations (5.19)-(5.22) to obtain

$$A_{pm} = E_{pm} + \frac{(-1)^p e^{\tilde{k}_p x_{m-1}}}{\tilde{k}_p^2(h-a-c)}, \tag{5.23}$$

$$B_{pm} = F_{pm} + \frac{(-1)^p e^{-\tilde{k}_p x_{m-1}}}{\tilde{k}_p^2(h-a-c)}, \tag{5.24}$$

$$C_{pm} = E_{pm} e^{-\tilde{k}_p L} + \frac{(-1)^p e^{\tilde{k}_p (x_m - L)}}{\tilde{k}_p^2(h-a-c)} \tag{5.25}$$

and

$$D_{pm} = F_{pm} e^{\tilde{k}_p L} + \frac{(-1)^p e^{-\tilde{k}_p (x_m - L)}}{\tilde{k}_p^2(h-a-c)}, \tag{5.26}$$

with $p = 1, 2, ...$ To obtain the expressions of A_{0m}, B_{0m}, C_{0m} and D_{0m} in terms of E_{0m} and F_{0m}, I repeat the procedure above but this time I multiply by $\cos[\tilde{k}_q(z+h-c)]$ with $q = 0$. Hence, the second condition of (5.17) yields

$$A_{0m} = E_{0m} + \frac{x_m - x_{m-1}}{2(h-a-c)}, \tag{5.27}$$

while from the first condition of (5.17) I obtain

$$B_{0m} = F_{0m} + x_{m-1}(E_{0m} - A_{0m}) + \frac{h-a-c}{6}. \tag{5.28}$$

Finally, C_{0m} and D_{0m} are given from the second and first conditions of (5.18) respectively:

$$C_{0m} = E_{0m} + \frac{x_{m-1} - x_m}{2(h-a-c)} \tag{5.29}$$

and

$$D_{0m} = F_{0m} + E_{0m} x_m - C_{0m}(x_m - L) + \frac{h-a-c}{6}. \tag{5.30}$$

These equations match the potential below the moving body m with the potentials below the static bodies in the inner region. Now I need to link the inner wave field with the outer wave field at the common boundaries and this will give me a system of integral equations, see section 5.2.

5.2 Radiation: external

I solve the radiation problem in the external regions left (L) and right (R), defining respectively the problem at the interface $x = 0$ and the problem at the interface $x = L$ and using a solution method based on the integral equations. This procedure is mathematically more onerous respect to the potentials matching method but allows to avoid singularity issues which would definitely occur both at the edges of the floater blanket and at the corners of the ocean step.

5.2.1 Left region (L)

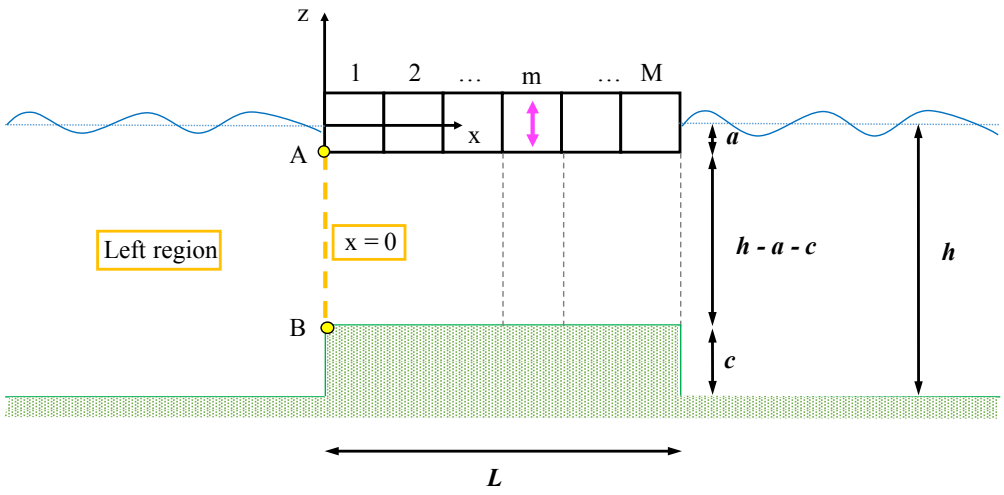

Figure 5.5: Left region and interface $x = 0$.

Let ϕ_{Lm} be the spatial potential in the left region, $x < 0$. Looking at Fig. 5.5, let me define the problem at the interface $x = 0$ as follow:

$$\frac{\partial \phi_{Lm}}{\partial x} = 0, \qquad x = 0^-, \quad z \in (-h,\ -h + c), \quad z \in (-a,\ 0), \tag{5.31}$$

$$\phi_{Lm} = \phi_m^{(1)}, \qquad x = 0^-, \quad z \in (-h + c,\ -a), \tag{5.32}$$

$$\frac{\partial \phi_{Lm}}{\partial x} = \frac{\partial \phi_m^{(1)}}{\partial x}, \qquad x = 0, \quad z \in (-h + c,\ -a) \tag{5.33}$$

and

$$|\nabla\phi_{Lm}| = O(r^{-1/3}) \qquad \text{on A and B, see again Fig. 5.5,} \tag{5.34}$$

where r is the distance from an edge. Using the method in [24], let me now define

$$\frac{\partial\phi_{Lm}}{\partial x}(0^-, z) \doteq f_{Lm}(z), \qquad z \in (-h,\ 0). \tag{5.35}$$

Then (5.31) becomes

$$f_{Lm}(z) = 0, \quad z \in (-h,\ -h+c), \quad z \in (-a,\ 0) \tag{5.36}$$

and (5.33) gives

$$f_{Lm}(z) = \left.\frac{\partial\phi_m^{(1)}}{\partial x}\right|_{x=0}, \qquad z \in (-h+c,\ -a). \tag{5.37}$$

Also, due to the edge condition described by (5.34), I must have the requirement that

$$f_{Lm} = O(|z+h-c|^{-1/3}), \qquad z \to -h+c \tag{5.38}$$

and

$$f_{Lm} = O(|z+a|^{-1/3}), \qquad z \to -a. \tag{5.39}$$

Now, the spatial velocity potential in the left region $\phi_{Lm}(x,z)$ is expressed by the usual form

$$\phi_{Lm}(x,z) = a_{0m}Z_0(z)e^{-ikx} + \sum_{p=1}^{+\infty} a_{pm}Z_p(z)e^{k_p x}, \qquad x \in (-\infty,\ 0^-), \quad z \in (-h,\ 0), \tag{5.40}$$

where the $Z_p(z)$ are the orthonormal functions:

$$Z_p(z) = \frac{\sqrt{2}\cosh[\kappa_p(z+h)]}{(h + g/\omega^2\sinh^2(\kappa_p h))^{1/2}}, \qquad p = 0, 1, 2, ...$$

In the latter, $\kappa_0 = k$ and $\kappa_p = ik_p$ with $p = 1, 2, ..$ solve the dispersion relations $\omega^2 = gk\tanh(kh)$ and $\omega^2 = -gk_p\tan(k_p h)$, respectively. The a_{0m} and a_{pm} are unknown coefficients. The $Z_p(z)$ satisfy $\int_{-h}^{0} Z_p Z_q \,\mathrm{d}z = \delta_{pq}$, where δ_{pq} is the Kronecker delta, see [27] and [40]. Hence substituting (5.40) in (5.35), multiplying by $Z_q(z)$, $q = 0, 1, 2...$, and integrating along z, I obtain

$$-ika_{0m} = \int_{-h+c}^{-a} f_{Lm}(z) Z_0(z) \,\mathrm{d}z \tag{5.41}$$

and

$$a_{pm}k_p = \int_{-h+c}^{-a} f_{Lm}(z) Z_p(z) \,\mathrm{d}z. \tag{5.42}$$

In (5.41) and (5.42), condition (5.36) has been used and the orthogonality of the vertical modes Z_q has been exploited. Using the same method, conditions (5.32) and (5.37) yield respectively

$$A_{pm} + B_{pm} = \frac{2}{h-a-c}[a_{0m}\Im_{0p} + \sum_{q=1}^{+\infty} a_{qm}\Im_{qp}] \tag{5.43}$$

and

$$B_{pm} - A_{pm} = \frac{2}{\tilde{k}_p(h-a-c)} \int_{-h+c}^{-a} f_{Lm}(z)\cos[\tilde{k}_p(z+h-c)] \,\mathrm{d}z, \tag{5.44}$$

where I exploited again the orthogonality of cosines. In (5.43),

$$\Im_{0p} = \int_{-h+c}^{-a} Z_0(z)\cos[\tilde{k}_p(z+h-c)] \,\mathrm{d}z \tag{5.45}$$

and

$$\Im_{qp} = \int_{-h+c}^{-a} Z_q(z)\cos[\tilde{k}_p(z+h-c)] \,\mathrm{d}z. \tag{5.46}$$

Finally, the integral equations for the left region can be obtained by substitut-

ing (5.12) and (5.40) in (5.33). This yields

$$-ika_{0m}Z_0(z)+\sum_{p=1}^{+\infty}a_{pm}Z_p(z)=A_{0m}+\sum_{p=1}^{+\infty}\tilde{k}_p(B_{pm}-A_{pm})\cos[\tilde{k}_p(z+h-c)]. \quad (5.47)$$

The amplitude coefficient A_{0m} can be determined by substituting (5.40) into (5.37) and integrating (5.37) along z between $z=-h+c$ and $z=-a$:

$$A_{0m}=\frac{1}{h-a-c}\int_{-h+c}^{-a}f_{Lm}(z)\,\mathrm{d}z. \quad (5.48)$$

Now I substitute (5.42), (5.44) and (5.48) in (5.47) and I get the integral equation:

$$\int_{-h+c}^{-a}F_{Lm}(u)\mathcal{M}(u,z)\,\mathrm{d}u=Z_0(z), \quad (5.49)$$

where $F_{Lm}(u)=-f_{Lm}(u)/ika_{0m}$ and $\mathcal{M}(u,z)$ is real and symmetric in u and z and is expressed by

$$\mathcal{M}(u,z)=\frac{1}{h-a-c}\left[2\sum_{p=1}^{+\infty}\cos[\tilde{k}_p(u+h-c)]\cos[\tilde{k}_p(z+h-c)]+1\right] -\sum_{p=1}^{+\infty}Z_p(u)Z_p(z). \quad (5.50)$$

Solving (5.49) with respect to f_{Lm} will allow me to determine the coefficients a_{0m} and a_{pm} from (5.41) and (5.42), respectively. Then A_{pm} and B_{pm} will be obtained from (5.43) and (5.44), respectively. Finally the coefficient B_{0m} in (5.12) is obtained by integrating (5.32) along z between $z=-h+c$ and $z=-a$:

$$B_{0m}=\frac{1}{h-a-c}\left[a_{0m}\int_{-h+c}^{-a}Z_0(z)\,\mathrm{d}z+\sum_{p=1}^{+\infty}a_{pm}\int_{-h+c}^{-a}Z_p(z)\,\mathrm{d}z\right]. \quad (5.51)$$

5.2.2 Right region (R)

As I did for the left region, I now obtain the integral relation for the right region, see Fig. 5.6.

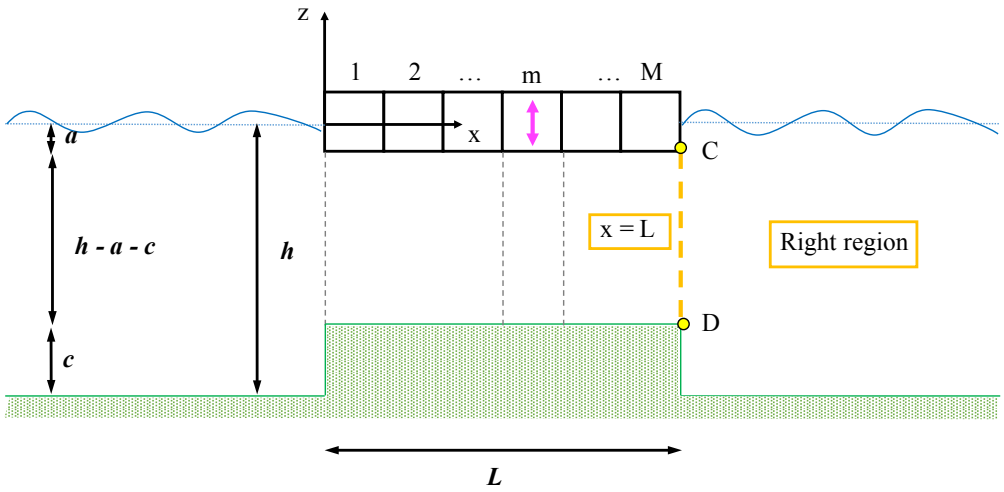

Figure 5.6: Right region and interface $x = L$.

The problem at the interface $x = L$ is

$$\frac{\partial \phi_{Rm}}{\partial x} = 0, \qquad x = L^+, \quad z \in (-h,\ -h + c), \quad z \in (-a,\ 0), \tag{5.52}$$

$$\phi_{Rm} = \phi_m^{(3)}, \qquad x = L, \quad z \in (-h + c,\ -a), \tag{5.53}$$

$$\frac{\partial \phi_{Rm}}{\partial x} = \frac{\partial \phi_m^{(3)}}{\partial x}, \qquad x = L, \quad z \in (-h + c,\ -a) \tag{5.54}$$

and

$$|\nabla \phi_{Rm}| = O(r^{-1/3}) \qquad \text{on C and D, see again Fig.5.6.} \tag{5.55}$$

Following the procedure in section 5.2.1, let me now define

$$\frac{\partial \phi_{Rm}}{\partial x}(L^+, z) \doteq f_{Rm}(z), \qquad z \in (-h,\ 0). \tag{5.56}$$

Then (5.52) gives

$$f_{Rm}(z) = 0, \qquad z \in (-h,\ -h+c), \quad z \in (-a,\ 0) \tag{5.57}$$

and (5.53) gives

$$f_{Rm}(z) = \left.\frac{\partial \phi_m^{(3)}}{\partial x}\right|_{x=L}, \qquad z \in (-h+c,\ -a). \tag{5.58}$$

Also, due to the edge condition described by (5.55), I must have the requirement that

$$f_{Rm} = O(|z+h-c|^{-1/3}), \qquad z \to -h+c \tag{5.59}$$

and

$$f_{Rm} = O(|z+a|^{-1/3}), \qquad z \to -a. \tag{5.60}$$

Now, the spatial velocity potential in the right region $\phi_{Rm}(x,z)$ is expressed by

$$\phi_{Rm}(x,z) = b_{0m} Z_0(z) e^{ik(x-L)} + \sum_{p=1}^{+\infty} b_{pm} Z_p(z) e^{-k_p(x-L)}, \qquad x \in (L^+,\ +\infty),$$
$$z \in (-h,\ 0). \tag{5.61}$$

Hence substituting (5.61) in (5.56), multiplying by $Z_q(z)$ and integrating along z, I obtain

$$ikb_{0m} = \int_{-h+c}^{-a} f_{Rm}(z) Z_0(z)\, \mathrm{d}z \tag{5.62}$$

and

$$-b_{pm}k_p = \int_{-h+c}^{-a} f_{Rm}(z) Z_p(z)\, \mathrm{d}z. \tag{5.63}$$

In (5.62) and (5.63), condition (5.57) has been used and the orthogonality of

the vertical modes Z_q has been exploited. Now the condition (5.53) and (5.58) yield respectively

$$C_{pm} + D_{pm} = \frac{2}{h-a-c}[b_{0m}\Im_{0p} + \sum_{q=1}^{+\infty} b_{qm}\Im_{qp}] \tag{5.64}$$

and

$$D_{pm} - C_{pm} = \frac{2}{\tilde{k}_p(h-a-c)} \int_{-h+c}^{-a} f_{Rm}(z)\cos[\tilde{k}_p(z+h-c)]\,\mathrm{d}z. \tag{5.65}$$

Finally the integral equations for the right region is

$$\int_{-h+c}^{-a} F_{Rm}(u)\mathcal{M}(u,z)\,\mathrm{d}u = Z_0(z), \tag{5.66}$$

which is the analogous of the equation (5.49). In (5.66), $F_{Rm}(u) = f_{Rm}(u)/ikb_{0m}$. Solving (5.66) with respect to f_{Rm} will allow me to determine the coefficients b_{0m} and b_{pm} from (5.62) and (5.63), respectively. Then C_{pm} and D_{pm} will be obtained from (5.64) and (5.65), respectively. Finally C_{0m} and D_{0m} in (5.13) can be obtained integrating respectively (5.58) and (5.53) along z between $z = -h + c$ and $z = -a$, which gives:

$$C_{0m} = \frac{1}{h-a-c} \int_{-h+c}^{-a} f_{Rm}(z)\,\mathrm{d}z, \tag{5.67}$$

$$D_{0m} = \frac{1}{h-a-c}\left[b_{0m}\int_{-h+c}^{-a} Z_0(z)\,\mathrm{d}z + \sum_{p=1}^{+\infty} b_{pm}\int_{-h+c}^{-a} Z_p(z)\,\mathrm{d}z\right]. \tag{5.68}$$

5.3 Useful identities

By inspection, equations (5.49) and (5.66) yield the following:

$$\int_{-h+c}^{-a} [F_{Lm}(u) - F_{Rm}(u)]\mathcal{M}(u,z)\,\mathrm{d}u = 0, \qquad \forall z \in [-h+c,\ -a], \tag{5.69}$$

so that

$$F_{Lm}(u) = F_{Rm}(u) = F_m(u). \tag{5.70}$$

The latter yields

$$\frac{f_{Lm}^{(u)}}{a_{0m}} + \frac{f_{Rm}^{(u)}}{b_{0m}} = 0, \qquad u \in (-h+c, \ -a) \tag{5.71}$$

and

$$\frac{f_{Rm}^{(u)}}{b_{0m}} - \frac{f_{Lm}^{(u)}}{a_{0m}} = 2F_m(u). \tag{5.72}$$

In addition, equations (5.42), (5.43) and (5.64) can be combined to get

$$\frac{A_{pm} + B_{pm}}{a_{0m}} = \frac{C_{pm} + D_{pm}}{b_{0m}} \tag{5.73}$$

or similarly

$$\frac{A_{pm} + B_{pm}}{f_{Lm}(u)} = -\frac{C_{pm} + D_{pm}}{f_{Rm}(u)}. \tag{5.74}$$

Analogously, equations (5.44) and (5.65) can be combined to get

$$\frac{A_{pm} - B_{pm}}{a_{0m}} = \frac{D_{pm} - C_{pm}}{b_{0m}} \tag{5.75}$$

and

$$\frac{A_{pm} - B_{pm}}{f_{Lm}(u)} = \frac{C_{pm} - D_{pm}}{f_{Rm}(u)}, \tag{5.76}$$

so that I can obtain

$$\frac{A_{pm}}{a_{0m}} = \frac{D_{pm}}{b_{0m}} \qquad \text{and} \qquad \frac{B_{pm}}{a_{0m}} = \frac{C_{pm}}{b_{0m}}. \tag{5.77}$$

Therefore, if I solve the problem in the left region for A_{pm} and B_{pm}, I also have the solution of the problem in the right region for C_{pm} and D_{pm}. Note that the full solution of the problem, given by (5.49) and (5.66), respectively, still depends on the unknown constants a_{0m} and b_{0m}. These can be determined by using the continuity equation and symmetry arguments, as shown in the following

section, in which I use the law of conservation of mass flow rate in the internal region to get the continuity equation. In addition, in appendix B, I derive an alternative relation between a_{0m} and b_{0m} based on the solution of both radiation and diffraction problems which yields a novel Bessho-Newman relation for the floater blanket.

5.4 Continuity equation

Let me consider that the vertical displacement of the floater m along the z direction is X_m as shown in Fig. 5.7.

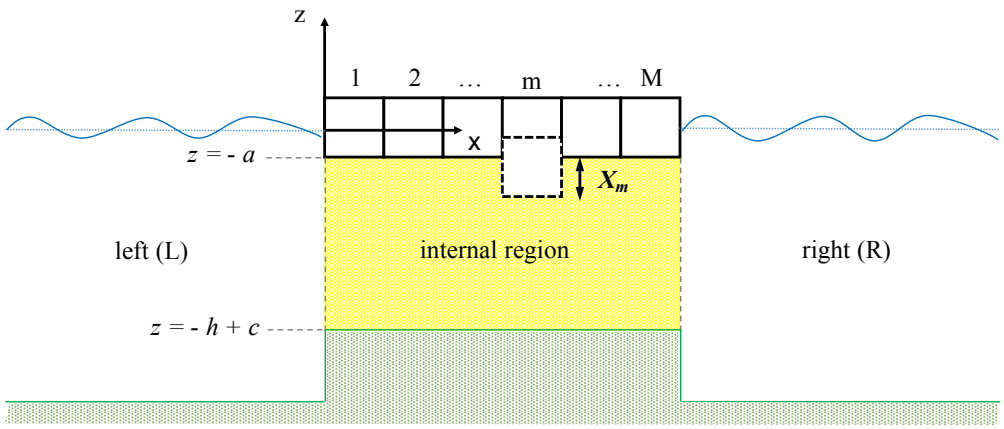

Figure 5.7: X_m is the vertical displacement of the floater m along the z direction. Considering the incoming (left) and outcoming (right) mass flow rates, I derive the continuity equation in the internal region (yellow).

Hence the law of conservation of mass flow rate in the internal region can be written as

$$Q_{ML} - Q_{MR} = \rho \frac{\partial V}{\partial t}, \tag{5.78}$$

where Q_{ML} and Q_{MR} are the incoming (left) and outcoming (right) mass flow rates, respectively and V is the fluid volume in the internal region, [10]. In fact I define the mass flow rate as the mass of water that passes through any cross sectional area per unit of time, so that in this case, the left-hand side of equation

(5.78), becomes

$$Q_{ML} - Q_{MR} = \int_{-h+c}^{-a} \rho \left[\frac{\partial \phi_L}{\partial x} - \frac{\partial \phi_R}{\partial x} \right] \mathrm{d}z = \int_{-h+c}^{-a} \rho [f_{Lm} - f_{Rm}] \, \mathrm{d}z, \tag{5.79}$$

where I exploited definitions (5.35) and (5.56). The right-hand side of equation (5.78) can be rewritten as

$$\rho \frac{\partial V}{\partial t} = \rho (x_m - x_{m-1}) \frac{\partial X_m}{\partial t}, \tag{5.80}$$

see again Fig. 5.7. Finally equation (5.78) yields

$$\int_{-h+c}^{-a} [f_{Lm} - f_{Rm}] \, \mathrm{d}z = x_m - x_{m-1}, \tag{5.81}$$

where I assumed that the floater moves along the z direction with unit vertical velocity, i.e. $\partial X_m / \partial t = 1$. In addition, equation (5.81) depends on a_{0m} and b_{0m} because, as stated in subsections 5.2.1 and 5.2.2 respectively, $f_{Lm}(u) = -ikF_{Lm}(u)a_{0m}$ and $f_{Rm}(u) = ikF_{Rm}(u)b_{0m}$. Also, exploiting the identity (5.70), the continuity equation (5.81) becomes

$$\int_{-h+c}^{-a} F_m(z) \, \mathrm{d}z = -\frac{x_m - x_{m-1}}{ik(a_{0m} + b_{0m})}. \tag{5.82}$$

The latter gives a relation between the amplitude coefficients a_{0m} and b_{0m}.

5.4.1 Symmetry and antisymmetry

I can observe that in the case of identical floaters, the effect generated from the vertical motion of a generic single element of the FBWEC which moves along the z-direction with vertical velocity V is the same effect generated by the sum of the vertical movements of two single elements of the device characterised by vertical velocity $V/2$ plus the movements of two other elements with opposite vertical velocities $V/2$ and $-V/2$ (see Fig. 5.8). Therefore I can describe the motion of a generic element of the FBWEC as superimposition of symmetric and antisymmetric problems. This allows me to reduce the complexity of the problem.

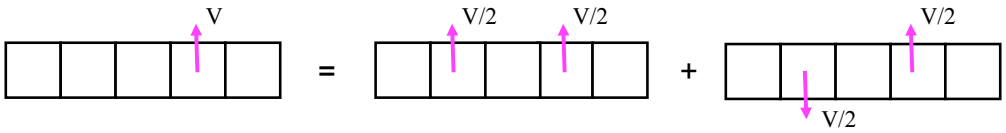

Figure 5.8: Superimposition of effects in terms of velocity.

In fact, if I introduce a new coordinate system with $x = x'' + L/2$, (see Fig. 5.9) and I consider now the symmetric case, then in the outer region $\phi_{Lm}(-x'') = \phi_{Rm}(x'')$, $x'' > 0$.

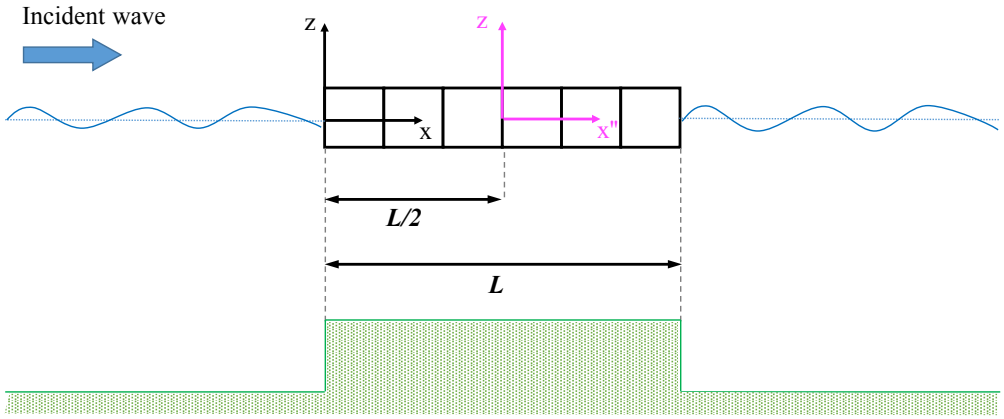

Figure 5.9: New coordinate system with $x = x'' + L/2$ (see magenta arrows).

Asymptotically, (5.40) ad (5.61) give, respectively,

$$\phi_{Lm}(-x'') \sim a_{0m} Z_0(z) e^{ik(x''-L/2)}, \qquad x'' \to \infty \tag{5.83}$$

and

$$\phi_{Rm}(x'') \sim b_{0m} Z_0(z) e^{ik(x''-L/2)}, \qquad x'' \to \infty. \tag{5.84}$$

Equating (5.83) and (5.84), I obtain that in the symmetric case $a_{0m} = b_{0m}$. Similarly, considering the antisymmetric case $\phi_{Lm}(-x'') = -\phi_{Rm}(x'')$ I get $a_{0m} = -b_{0m}$.

5.5 Summary of equations and unknowns of the radiation problem

Here I present a summary of equations and unknowns which describe the radiation problem for a single element of the FBWEC which moves along the z-direction with unit velocity:

$$\int_{-h+c}^{-a} F_m(u)\mathcal{M}(u,z)\,\mathrm{d}u = Z_0(z), \tag{5.85}$$

$$F_m(u) = \frac{f_{Rm}}{b_{0m}} = -\frac{f_{Lm}}{a_{0m}}, \tag{5.86}$$

$$A_{0m} = \frac{1}{h-a-c}\int_{-h+c}^{-a} f_{Lm}(z)\,\mathrm{d}z, \tag{5.87}$$

$$B_{0m} = \frac{1}{h-a-c}\left[a_{0m}\int_{-h+c}^{-a} Z_0(z)\,\mathrm{d}z + \sum_{p=1}^{+\infty} a_{pm}\int_{-h+c}^{-a} Z_p(z)\,\mathrm{d}z\right], \tag{5.88}$$

$$C_{0m} = \frac{1}{h-a-c}\int_{-h+c}^{-a} f_{Rm}(z)\,\mathrm{d}z, \tag{5.89}$$

$$D_{0m} = F_{0m} + E_{0m}x_m - C_{0m}(x_m - L) + \frac{h-a-c}{6}, \tag{5.90}$$

$$E_{0m} = A_{0m} - \frac{x_m - x_{m-1}}{2(h-a-c)}, \tag{5.91}$$

$$F_{0m} = B_{0m} - x_{m-1}(E_{0m} - A_{0m}) - \frac{h-a-c}{6}, \tag{5.92}$$

$$A_{pm} = E_{pm} + \frac{(-1)^p e^{\tilde{k}_p x_{m-1}}}{\tilde{k}_p^2(h-a-c)}, \qquad p = 1, 2, ..., \tag{5.93}$$

$$B_{pm} = F_{pm} + \frac{(-1)^p e^{-\tilde{k}_p x_{m-1}}}{\tilde{k}_p^2(h-a-c)}, \qquad p = 1, 2, ..., \tag{5.94}$$

$$C_{pm} = E_{pm}e^{-\tilde{k}_p L} + \frac{(-1)^p e^{\tilde{k}_p(x_m - L)}}{\tilde{k}_p^2(h-a-c)}, \qquad p = 1, 2, ..., \tag{5.95}$$

$$D_{pm} = F_{pm}e^{\tilde{k}_p L} + \frac{(-1)^p e^{-\tilde{k}_p(x_m - L)}}{\tilde{k}_p^2(h-a-c)}, \qquad p = 1, 2, ..., \tag{5.96}$$

$$B_{pm} - A_{pm} = \frac{2}{\tilde{k}_p(h-a-c)} \int_{-h+c}^{-a} f_{Lm}(z) \cos[\tilde{k}_p(z+h-c)]\, \mathrm{d}z, \tag{5.97}$$

$$D_{pm} - C_{pm} = \frac{2}{\tilde{k}_p(h-a-c)} \int_{-h+c}^{-a} f_{Rm}(z) \cos[\tilde{k}_p(z+h-c)]\, \mathrm{d}z, \tag{5.98}$$

$$\frac{A_{pm}}{a_{0m}} = \frac{D_{pm}}{b_{0m}} \qquad \text{and} \qquad \frac{B_{pm}}{a_{0m}} = \frac{C_{pm}}{b_{0m}}, \tag{5.99}$$

$$\int_{-h+c}^{-a} F_m(z)\, \mathrm{d}z = -\frac{x_m - x_{m-1}}{ik(a_{0m} + b_{0m})}, \tag{5.100}$$

$$a_{0m} = b_{0m} \quad \text{symmetry} \quad \text{or} \quad a_{0m} = -b_{0m} \quad \text{antisymmetry}, \tag{5.101}$$

$$a_{pm}k_p = \int_{-h+c}^{-a} f_{Lm}(z) Z_p(z)\, \mathrm{d}z, \tag{5.102}$$

$$-b_{pm}k_p = \int_{-h+c}^{-a} f_{Rm}(z) Z_p(z)\, \mathrm{d}z. \tag{5.103}$$

5.6 Solution procedure of the radiation problem

Once F_m is determined from the integral equation (5.85), a_{0m} and b_{0m} can be found by using (5.101) for the symmetric and antisymmetric part, respectively and the continuity equation (5.100). Then the a_{pm} and b_{pm} can be found with (5.86), (5.102) and (5.103) respectively. Now A_{pm}, B_{pm}, C_{pm}, D_{pm}, E_{pm} and F_{pm} can be determined by solving the system (5.93)-(5.99). Finally the system (5.87)-(5.92) yields expressions for the amplitude coefficients A_{0m}, B_{0m}, C_{0m}, D_{0m}, E_{0m}

and F_{0m}, respectively so that the potentials ϕ_{Lm}, $\phi_m^{(i)}$, $i = 1, 2, 3$ and ϕ_{Rm} are fully determined. Note that (5.41), (5.43), (5.62), (5.64) and (5.68) have not been used yet. They will be employed to check the accuracy of the numerical solution of the integral equations.

5.6.1 Solution of the integral equation

Exploiting the identity (5.70), our integral equation reduces to

$$\int_{-h+c}^{-a} F_m(u)\mathcal{M}(u,z)\,\mathrm{d}u = Z_0(z), \tag{5.104}$$

which is a Fredholm integral equation of the first kind and belongs to the class of ill-posed problems, i.e. admits a solution which is unstable with respect to small variations in the right-hand side $Z_0(z)$ of the integral equation, [36]. This instability of solutions of integral equations of the first kind causes great difficulties when using such equations for practical purposes, since small errors in input data may cause large variations of a solution. For this reason regularisation methods have been developed to rewrite Fredholm equations of the *first kind* as Fredholm equations of the *second kind* which can be solved by using finite element methods, whence the solution exists and is unique, [36]. Following the Lavrentiev regularisation method, along with equation (5.104) I consider the regularised integral equation

$$\varepsilon F_m(u) + \int_{-h+c}^{-a} F_m(u)\mathcal{M}(u,z)\,\mathrm{d}u = Z_0(z), \tag{5.105}$$

where $\varepsilon > 0$ is the regularisation parameter. On taking a sufficiently small ε, I find a solution $F_{m\varepsilon}(u)$ of equation (5.105) and substitute this solution in equation (5.104), thus obtaining

$$\int_{-h+c}^{-a} F_{m\varepsilon}(u)\mathcal{M}(u,z)\,\mathrm{d}u = Z_{0\varepsilon}(z). \tag{5.106}$$

If the function $Z_{0\varepsilon}(z)$ thus obtained differs only slightly from $Z_0(z)$, that is,

$$||Z_0(z) - Z_{0\varepsilon}(z)|| \leq \delta, \tag{5.107}$$

where δ is a prescribed small positive number, then the solution $F_{m\varepsilon}(u)$ is regarded as a sufficiently good approximate solution of equation (5.104). The parameter δ defines the error of the initial data provided that the right-hand side of equation (5.104) is defined. For the case of which, for a given ε, condition (5.107) fails, I must choose another value of the regularisation parameter and repeat the above procedure.

The integral equation (5.105) is of the second kind and can be solved adopting a Galerkin approach in order to convert a continuous operator problem (integral equation) into a discrete problem, see [24]. The functions $F_m(u)$ are approximated as

$$F_m(u) \approx \mathcal{F}_m(u), \qquad u \in (-h+c, \ -a), \tag{5.108}$$

where $\mathcal{F}_m(u)$ have multi-term Galerkin expansions in terms of suitable basis functions $p_n(u)$ and unknown constants α_{mn}:

$$\mathcal{F}_m(u) = \sum_{n=0}^{N} \alpha_{mn} p_n(u). \tag{5.109}$$

Therefore if I substitute (5.109) in (5.105) using the approximation (5.108), I obtain

$$\varepsilon \sum_{n=0}^{N} \alpha_{mn} p_n(u) + \int_{-h+c}^{-a} \sum_{n=0}^{N} \alpha_{mn} p_n(u) \mathcal{M}(u,z)\, \mathrm{d}u = Z_0(z). \tag{5.110}$$

Now I multiply (5.110) by appropriate $p_q(z)$ and integrate over the interval $(-h+c; \ -a)$ to get the linear systems

$$\sum_{n=0}^{N} \alpha_{mn} K_{nq} = H_q, \qquad n,q = 0,1,2,....,N, \tag{5.111}$$

where

$$K_{nq} = \int_{-h+c}^{-a} \varepsilon p_n(u) p_q(z)\, \mathrm{d}z + \int_{-h+c}^{-a} \int_{-h+c}^{-a} p_n(u) p_q(z) \mathcal{M}(u,z)\, \mathrm{d}u\, \mathrm{d}z, \qquad n,q = 0,1,2,....,N \tag{5.112}$$

and

$$H_q = \int_{-h+c}^{-a} Z_0(z) p_q(z)\,\mathrm{d}z, \qquad q = 0, 1, 2, ..., N. \tag{5.113}$$

The integrals (5.112) and (5.113) can be evaluated explicitly choosing suitable basis functions whose details are described in appendix C, and the constants α_{mn} are obtained by solving the linear equations (5.111).

Chapter 6

FBWEC: numerical example

The analytical boundary-value radiation problem (5.85)-(5.103) is now well-posed and can be solved for different configurations. For the sake of example, in this chapter I present numerical results of a symmetrical configuration of the FBWEC. The system is characterised by a geometrical symmetry respect to the vertical axis passing through the centre of the m-th floater element which is moving up and down along the z direction. In this case, the internal potential in the region 2 is expressed by

$$\phi_m^{(2)}(x,z) = \sum_{p=1}^{+\infty}(E_{pm}e^{-\tilde{k}_p x} + F_{pm}e^{\tilde{k}_p x})\cos[\tilde{k}_p(z+h-c)] + \frac{(z+h-c)^2 - (x-x_{m-1})(x-x_m)}{2(h-a-c)}, \quad x_{m-1} \leq x_m. \tag{6.1}$$

In fact, compared with expression (5.16), E_{0m} must be 0, otherwise $\phi_m^{(2)}(x,z)$ would be composed of a linear term which is definitely not symmetric respect to the vertical axis passing through the centre of the m-th element. In addition, F_{0m} is a constant that can be chosen to be nil because it does not affect the velocity field. Note that the contribute of F_{0m} needs to be considered in any study which involves the pressure field. The symmetry arguments determine a simplification on the radiation problem, therefore, the unknown constants a_{0m} and b_{0m} can be determined by using the matching conditions (5.17) and (5.18) when $p = 0$ to obtain novel expressions for A_{0m}, B_{0m}, C_{0m} and D_{0m} and then, by combining the

latter with the relations already obtained in section 5.2, as shown in section 6.1.

6.1 Radiation problem for a symmetric case

Following the procedure used in subsection 5.1.3, first I substitute the expressions for $\phi_m^{(1)}$ (5.12) and $\phi_m^{(2)}$ (6.1) into the first condition of (5.17). Then, multiply by $\cos[\tilde{k}_q(z+h-c)]$, with $q=0$ and integrate along z between $z=-h+c$ and $z=-a$. This yields

$$B_{0m} = \frac{h-a-c}{6} - A_{0m}x_{m-1}. \tag{6.2}$$

Using the same procedure, from the second condition of (5.17) I obtain

$$A_{0m} = \frac{x_m - x_{m-1}}{2(h-a-c)}, \tag{6.3}$$

while the first and second conditions of (5.18) give, respectively,

$$D_{0m} = \frac{h-a-c}{6} - C_{0m}(x_m - L) \tag{6.4}$$

and

$$C_{0m} = \frac{x_{m-1} - x_m}{2(h-a-c)}. \tag{6.5}$$

Note that these expressions verify (5.27), (5.28), (5.29) and (5.30) respectively when $E_{0m} = F_{0m} = 0$. Now I compare (6.3) with (5.48) to obtain the following expression for a_{0m}:

$$a_{0m} = \frac{x_{m-1} - x_m}{2ik\int_{-h+c}^{-a} F_{Lm}(z)\,\mathrm{d}z}, \tag{6.6}$$

where $F_{Lm}(z) = F_{Rm}(z) = F_m(z)$, see identity (5.70), and will be determined by solving the integral equation $\int_{-h+c}^{-a} F_m(u)\mathcal{M}(u,z)\,\mathrm{d}u = Z_0(z)$ as reported in subsection 5.6.1. Similarly, substituting (6.5) in (5.67), I get

$$b_{0m} = \frac{x_{m-1} - x_m}{2ik\int_{-h+c}^{-a} F_{Rm}(z)\,\mathrm{d}z}, \tag{6.7}$$

hence, $a_{0m} = b_{0m}$, see (6.6), (6.7) and (5.70). Finally substituting (6.3) in (6.2) and (6.5) in (6.4) yields respectively

$$B_{0m} = \frac{(h-a-c)^2 - 3x_{m-1}(x_m - x_{m-1})}{6(h-a-c)} \tag{6.8}$$

and

$$D_{0m} = \frac{(h-a-c)^2 + 3(x_m - L)(x_m - x_{m-1})}{6(h-a-c)}. \tag{6.9}$$

Now, the fact that $a_{0m} = b_{0m}$ allows me to simplify the radiation problem (5.85)-(5.103) which can be rearranged as follows:

$$a_{0m} = b_{0m} = \frac{x_{m-1} - x_m}{2ik\int_{-h+c}^{-a} F_m(z)\,\mathrm{d}z}, \tag{6.10}$$

$$\int_{-h+c}^{-a} F_m(u)\mathcal{M}(u,z)\,\mathrm{d}u = Z_0(z), \tag{6.11}$$

$$F_m(u) = \frac{f_{Rm}}{b_{0m}} = -\frac{f_{Lm}}{a_{0m}}, \qquad f_{Rm} = -f_{Lm}, \tag{6.12}$$

$$a_{pm} = b_{pm} = \frac{1}{k_p}\int_{-h+c}^{-a} f_{Lm}(z)Z_p(z)\,\mathrm{d}z, \tag{6.13}$$

$$A_{0m} = \frac{x_m - x_{m-1}}{2(h-a-c)}, \tag{6.14}$$

$$B_{0m} = \frac{(h-a-c)^2 - 3x_{m-1}(x_m - x_{m-1})}{6(h-a-c)}, \tag{6.15}$$

$$C_{0m} = \frac{x_{m-1} - x_m}{2(h-a-c)}, \tag{6.16}$$

$$D_{0m} = \frac{(h-a-c)^2 + 3(x_m - L)(x_m - x_{m-1})}{6(h-a-c)}, \tag{6.17}$$

$$E_{0m} = F_{0m} = 0, \tag{6.18}$$

$$A_{pm} = E_{pm} + \frac{(-1)^p e^{\tilde{k}_p x_{m-1}}}{\tilde{k}_p^2 (h-a-c)}, \qquad p = 1, 2, ..., \tag{6.19}$$

$$B_{pm} = F_{pm} + \frac{(-1)^p e^{-\tilde{k}_p x_{m-1}}}{\tilde{k}_p^2 (h-a-c)}, \qquad p = 1, 2, ..., \tag{6.20}$$

$$C_{pm} = B_{pm} \qquad \text{and} \qquad D_{pm} = A_{pm}, \tag{6.21}$$

$$B_{pm} - A_{pm} = \frac{2}{\tilde{k}_p (h-a-c)} \int_{-h+c}^{-a} f_{Lm}(z) \cos[\tilde{k}_p (z+h-c)] \, \mathrm{d}z, \tag{6.22}$$

$$D_{pm} - C_{pm} = \frac{2}{\tilde{k}_p (h-a-c)} \int_{-h+c}^{-a} f_{Rm}(z) \cos[\tilde{k}_p (z+h-c)] \, \mathrm{d}z. \tag{6.23}$$

6.2 Numerical results: radiation by a 2D floater blanket

In this section, I solve numerically the system (6.10)-(6.23) by means of suitable Matlab codes which allow me to obtain a numerical evaluation of the integrals defined in subsection 5.6.1 and, hence, the characterisation of the waves radiated by a 2-dimensional FBWEC. This has been done by choosing the basis functions $p_n(z)$ as in appendix C, by considering the Lavrentiev regularisation to solve the integral equations, see again subsection 5.6.1 and by applying a multi-scale method for solving linear systems as in [46]. I select specific configurations, so that the geometry of the floater blanket system is known and can be included in a Matlab code as input data. In particular, all the numerical simulations carried out in this chapter, are based on symmetric FBWECs composed of three floater elements; also, the first and the third bodies are fixed to rigid support structures in the ocean, while the middle floater is moving vertically along the z direction, see Fig. 6.1.

Regarding the numerical analysis, I choose a maximum order of the multi-term Galerkin expansion to be equal to 7, see equation (5.109), a Lavrentiev regularisation parameter $\varepsilon = 0.00001$, see equation (5.105) and a numerical tolerance of

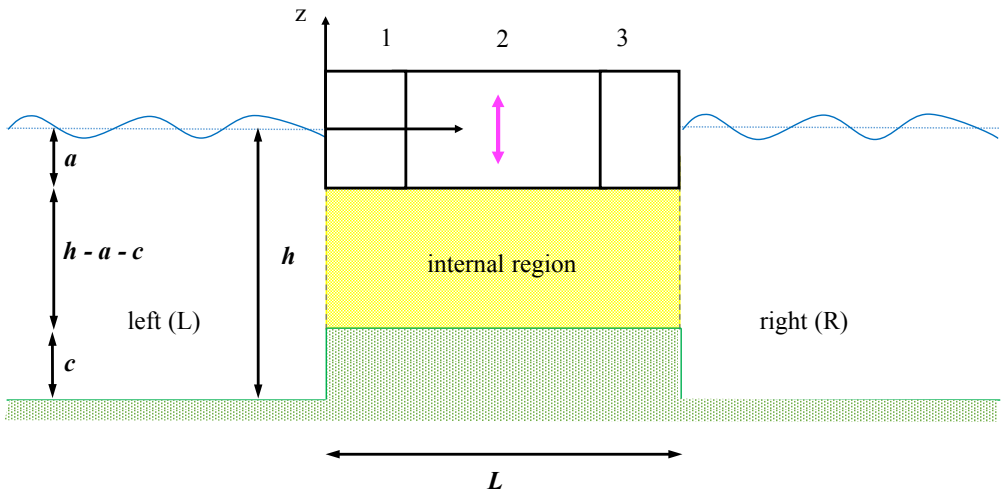

Figure 6.1: Geometry of the FBWEC system used for numerical simulations. Validation of the mathematical model and the parametric behaviour of system have been addressed for a device composed of 3 elements. Element 1 an 3 represent fixed mooring structures and do not move.

1×10^{-6}. The dispersion relation has been solved by using the iterative method proposed by Chamberlain & Porter in [12], which yields a wavenumber vector composed of propagating and evanescent components which represent the eigenmodes of the problem. These are finally used to find solutions of the regularised linear system matrix for each frequency with a multi-scale method, see [46]. Below, I present numerical results in which radiated wave amplitudes have been calculated when the central floater executes only one mode of oscillation, i.e. vertical movement along the z-axis.

With the amplitude of the potential thus found, the corresponding amplitude of the wave height may be inferred from the linearised Bernoulli equation, see chapter 2. Hence, let me define the normalised far field amplitude of the radiated wave as follows

$$Arz = \omega \left| -\frac{i\omega}{g} a_{0m} \frac{\sqrt{2}\cosh(kh)}{\sqrt{h + g/\omega^2 \sinh^2(kh)}} \right|. \tag{6.24}$$

Then, I can plot the latter versus the non-dimensional wavenumber ka. In the following two subsections, I present a validation of our results with those obtained by Black, Mei and Bray in 1971 with a different mathematical method (subsection 6.2.1) and a parametric behaviour of the system (subsection 6.2.2), respectively.

6.2.1 Results validation

To the best of our knowledge, no studies on the propagation of radiated wave from a 2-dimensional body with the same geometry of the floater blanket proposed in this thesis, have beed addressed yet. However, in 1971 Black et al. solved a semi-numerical radiation problem for a horizontal rectangular cylinder floating on the free surface and oscillating up and down along the z direction without shelf ($c = 0$) [9]. Unlike ours, the mathematical method used by Black et al. is based on the application of Schwinger's variational formulation for the far field and the Rayleigh-Ritz procedure, see [9] for further details. Also, note that in [9], the authors considered one single body, while our floater blanket is composed of three elements. Hence, to simulate their analysis and to maintain a symmetric geometry, I selected particular configurations of the three floaters in which the first and the third elements are much shorter than the middle one along the x-axis. Geometric details are reported in Tab. 6.1 and Fig. 6.2.

Table 6.1: Geometry of two floater blankets oscillating vertically on the free surface. The water depth is $h = 20$ m and I assume this value to be constant in the whole fluid domain, therefore I consider the shelf height $c = 0$ m. X is the coordinate vector of the floaters position along the x-axis; a is the blanket draft, see Fig. 6.2.

	FBWEC magenta	**FBWEC blue**
L (m)	60	20
a (m)	10	10
L/2a (-)	3	1
X (m)	[0 0.5 59.5 60]	[0 0.1 19.9 20]
Length I and III floaters (m)	0.5	0.1

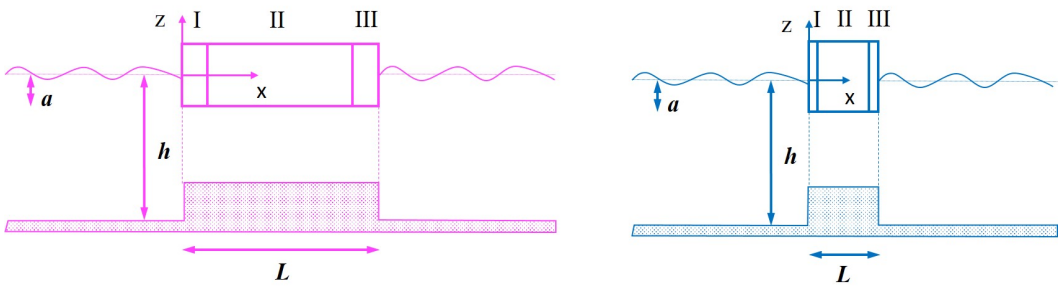

Figure 6.2: Schematic representation of the FBWEC systems related to Tab. 6.1.

By using a different mathematical method based on the integral equations, I

obtained an excellent agreement with the numerical results presented by Black et al. in [9] as shown in Fig. 6.3, where I plotted the normalised far field amplitude of the radiated wave $Arz(k)$ versus the non-dimensional wavenumber ka in the same interval chosen by Black et al., see Fig 6.4, where ka used in this thesis corresponds to kH used in [9]. The maximum regularisation error of this numerical evaluation is 3.697567×10^{-4}.

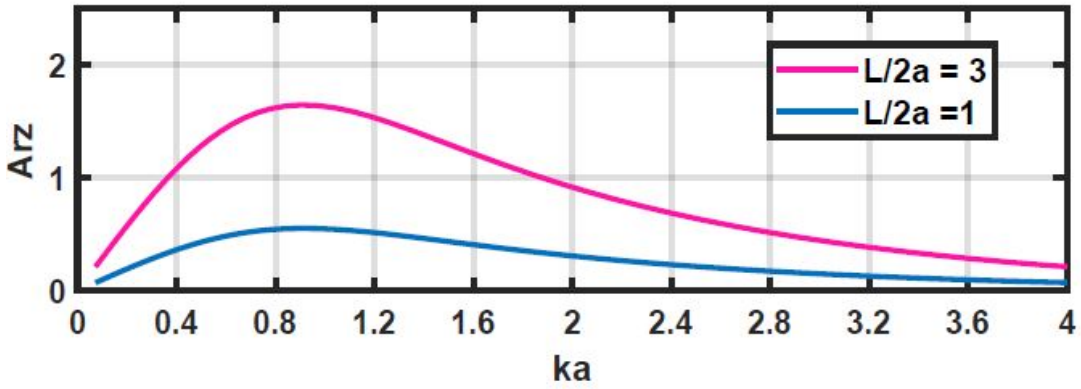

Figure 6.3: Normalised radiated-wave amplitude (Arz) due to vertical oscillation of the central floater of Fig. 6.1 versus the non-dimensional wavenumber ka. Excellent agreement with previous results obtained by Black, Mei and Bray [9].

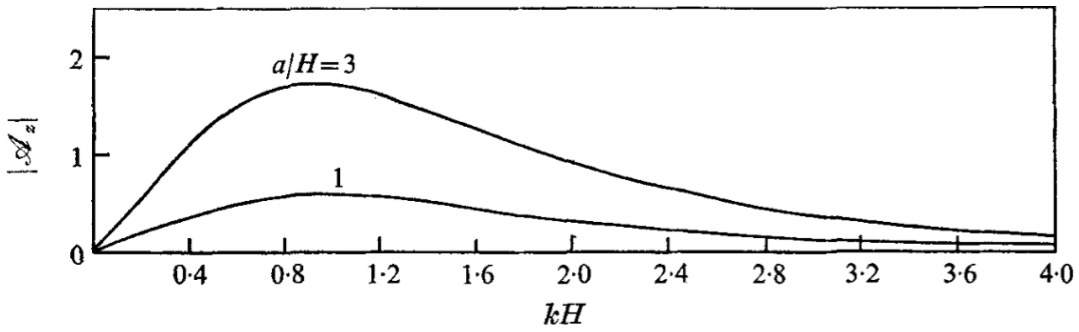

Figure 6.4: Radiated wave amplitude (magnitude and phase) due to vertical body oscillation for a horizontal rectangular cylinder in free surface. The figure is taken from [9].

6.2.2 Parametric analysis

Having validating our model with previous results, I am now in the position to determine the parametric behaviour of the system. This analysis plays a key role for a better understanding of the characterisation of the radiated waves by a 2-

dimensional floater blanket. In particular, in this subsection I present numerical results of the far-field amplitude of the radiated waves in relation to a wide range of frequencies. First, let me investigate the influence of the shelf height c. Numerical results for six values of c are shown in Fig. 6.5. The effect of the ocean step is seen to be more visible when $0.7 < ka < 3$; on the contrary there is practically no visible difference between the six curves when $ka < 0.7$ which for fixed a correspond to longer waves, or lower frequencies. For very short waves ($ka > 3$), it seems that the effect of the ocean step is not remarkable, infact the six curves are close to overlap. In addition, note that the effect of increasing the height of the ocean step c is to slightly shift the radiated-wave amplitude peaks towards higher frequencies ($ka \uparrow$).

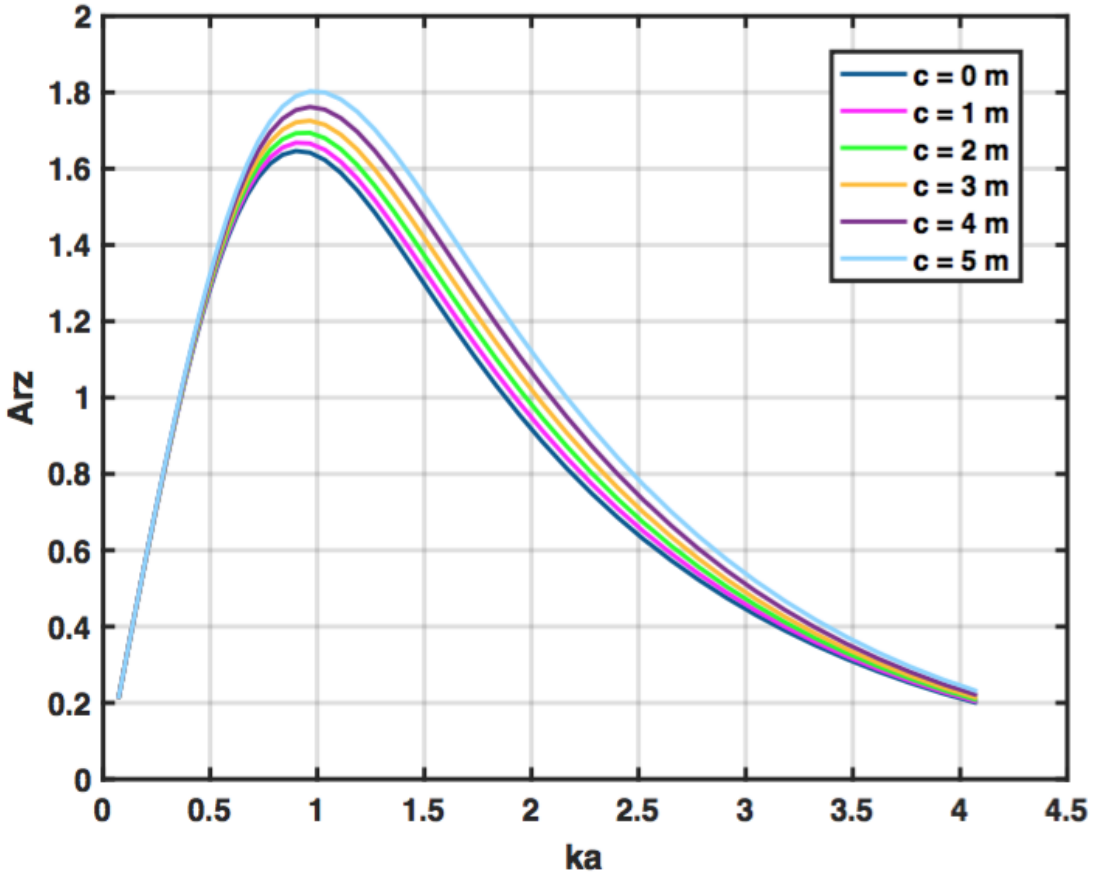

Figure 6.5: Normalised radiated-wave amplitude due to the oscillation of the middle floater of a FBWEC composed of 3 elements. The six curves represent the same device floating on the free surface in correspondence of an ocean step characterised by different height. In particular c varies between 0 m and 5 m. The geometry of the system is: $L = 60$ m, $a = 10$ m, $h = 20$ m. The first and third floaters are 0.5 m long and fixed to rigid support systems in the ocean.

Fig. 6.6 illustrates numerical results obtained from four 60 m long devices characterised by floaters of different lengths. Again, the first and third elements are fixed to rigid support systems in the ocean and have the same length along the x-axis in order to maintain a geometrical symmetry respect to the vertical axis passing through the centre of the second floater which is moving up and down along the z direction. As expected, a reduction of the size of the oscillating body, results in a decrease of the amplitude of the radiated wave due to less volume involved in the movement, see section 5.4 for further details on the law of conservation of mass flow rate. The length of the floaters are summarised in Tab. 6.2. The maximum regularisation error for this study is 4.715135×10^{-4}.

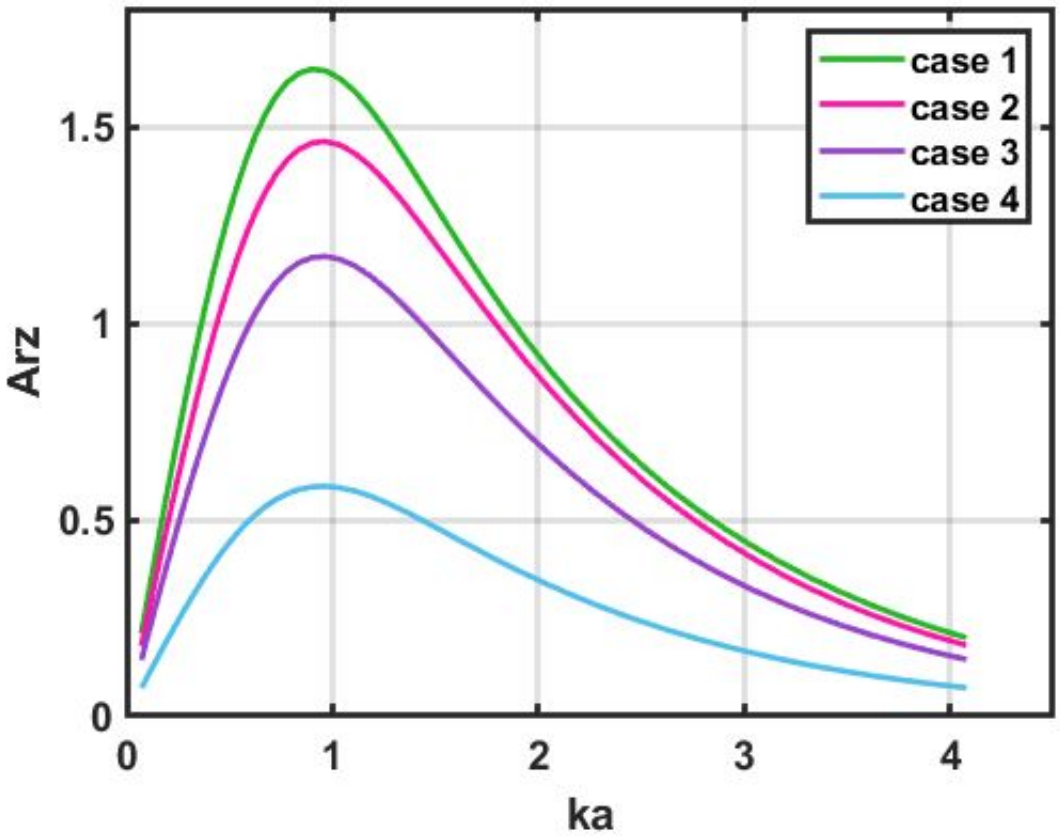

Figure 6.6: Influence of the length of the middle floater on the radiated-wave amplitude by 2D FBWECs composed of 3 elements. The geometry of the system is: $L = 60$ m, $a = 10$ m, $h = 20$ m, $c = 3$ m.

To conclude the parametric analysis for the numerical example presented in this chapter, I investigate the behaviour of the amplitude of the far-field radiated waves maintaining constant the ratio b/L (Fig. 6.7) and h/c (Fig. 6.8), where b

Table 6.2: Lengths of the I, II and III floater elements of the four FBWECs identified in Fig. 6.6 by the green, magenta, purple and light blue curves, respectively.

	Line colour	**Length I and III floaters** m	**Length II floater** m
case 1	Green	0.5	59
case 2	Magenta	5	50
case 3	Purple	10	40
case 4	Light blue	20	20

indicates the length of the middle floater. From Fig. 6.7 it can be seen that the amplitude of the radiated wave depends mainly on the dimensions of the device. In fact, if I fix the geometry of the ocean environment (h, a and c) and the ratio between the length of the whole floater blanket and the length of the oscillating body, bigger is the size of the FB and higher is the amplitude of the radiated wave.

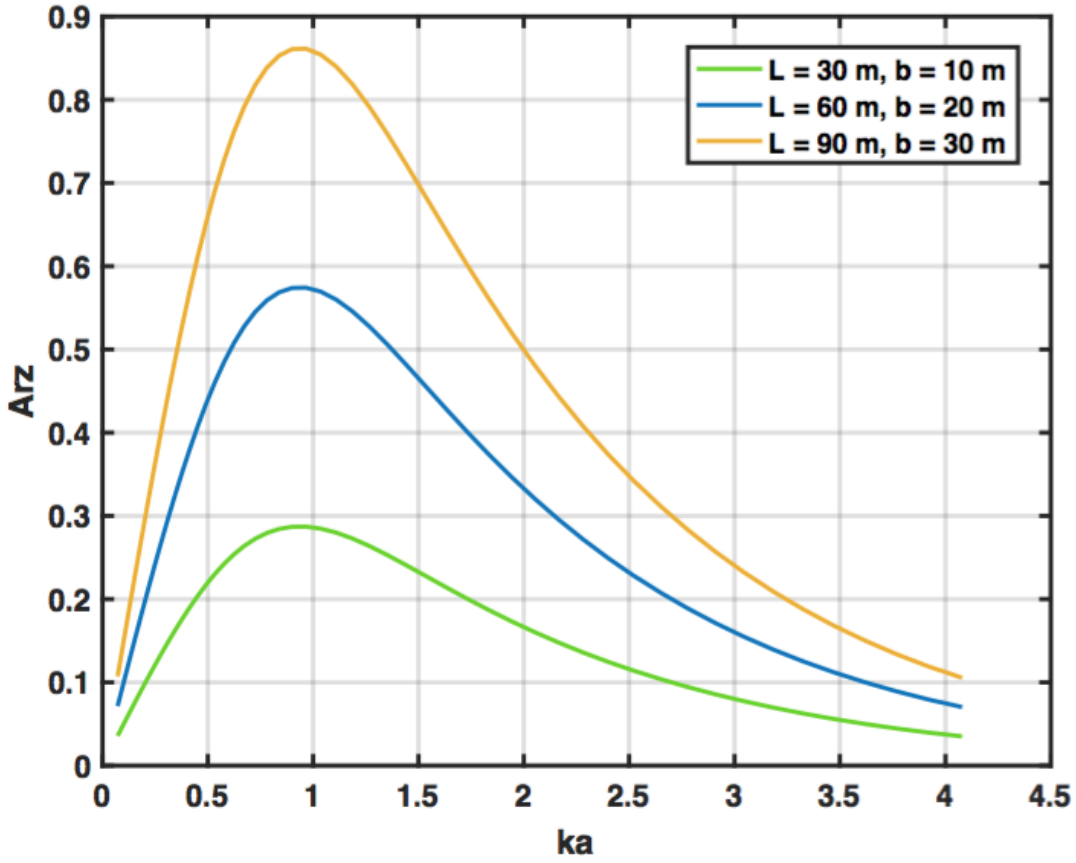

Figure 6.7: Each of the FBWECs represented in this plot is composed of three floaters which have the same dimension along the x-axis. The ratio between the length of the middle floater b and the whole length of the device L is fixed equal to 1/3. The geometry of the system is: $h = 20$ m, $a = 10$ m, $c = 2$ m. Maximum regularisation error is 4.302827×10^{-4}.

Finally, I analyse the influence of the ratio h/c on the radiated wave. Hence, let me choose a 60 m long floater blanket composed of three elements of equal dimensions (20 m each). The draft of the blanket a is fixed at 10 m, while the water depth h and the shelf height c can vary, but their ratio is kept constant ($h/c = 5$). Data in Fig. 6.8, suggest that the effect of the ratio h/c is more important for higher frequencies ($ka > 0.4$); in fact the curves are practically overlapping when $ka < 0.4$ (longer waves, or lower frequencies). In addition, when the height of the water column below the blanket increases, the amplitude of the radiated waves decrease, the corresponding curve become less sharp and the peaks are slightly shifted towards lower frequencies. The maximum error of this numerical study is of the order of $\mathrm{O}(10^{-4})$.

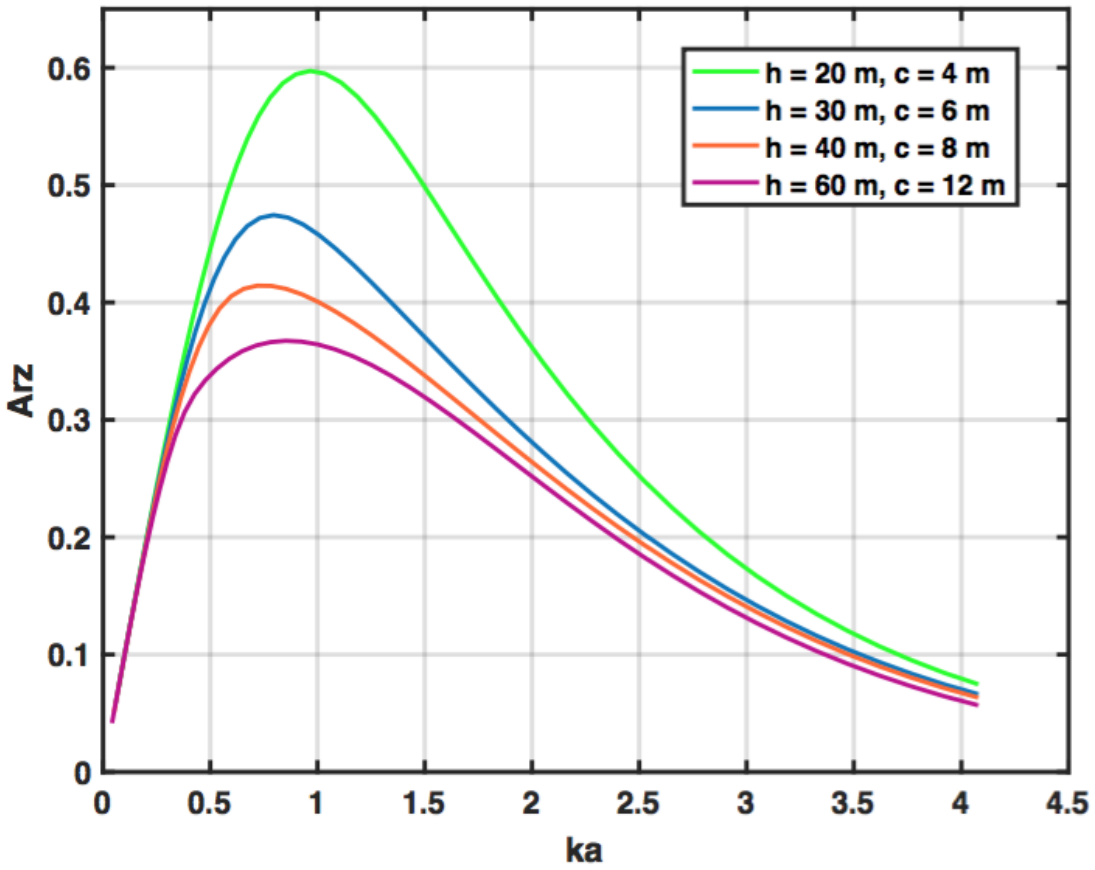

Figure 6.8: Effect of the simultaneous variation of water depth and shelf height on the amplitude of the radiated waves by a 60 m long 2D floater blanket WEC. Four numerical simulations have been carried out varying h and c, but keeping their ration constant and equal to 5. The device is made of three floaters of equal length (20 m each) and the blanket daft is 10 m.

Chapter 7

Concluding remarks

The purpose of this thesis was to provide the reader with mathematical techniques that can be used to develop semi-analytical models in order to analyse wave-structure interaction problems with application to wave energy conversion. In line with both the new trends of devices that I have referred to in section 1.3 and the energy global challenge research theme discussed in chapter 1, I proposed to investigate the hydrodynamic behaviour of two novel WECs: a flexible piezoelectric wave energy converter (PWEC) and a floater blanket wave energy converter (FBWEC).

The PWEC is characterised by sleek design and makes use of a smart material, in fact it consists of a bimorph piezoelectric plate, in which piezoelectric patches are connected in series and bonded at both faces of a flexible substrate with reversed polarities. This configuration allows the device to transform the elastic motion of the plate (induced by incident ocean surface waves) into useful electricity by means of the piezoelectric effect. Two PWEC systems has been considered and compared in this thesis: a PWEC moored on a vertical wall (i.e. a caisson breakwater) characterised by a plate length of 10 m and a 20 m long PWEC not moored on a caisson breakwater. A fully coupled hydro-electromechanical model has been derived for two piezoelectric wave energy harvesters by using a semi-analytical approach. We coupled a distributed-parameter model of the piezoelectric system with a potential-flow model of the water waves obtaining a novel hydro-electromechanical dispersion relation whose roots have been determined numerically in the complex wavenumber plane. We showed that the effect

of the piezoelectric coupling in the hydro-elastic domain generates a system of weakly damped progressive waves travelling along the plate and we identified the presence of sharp resonant periods of the device, at which the power output is significant. The extracted energy can be easily used for low-power applications such as supplying LEDs, wireless routers, computers, sensors, etc. In addition, comparing the power generated by the two devices, I noted that the presence of the breakwater improves significantly the performance of the converter. The extracted power is roughly 4 times greater that the one of the same device which is not moored on the vertical wall. This allows one to produce more electric power minimising the manufacturing costs of the device. Note that the maximum power output of the PWEC (8 kW/m for the PWEC moored on the breakwater) is much smaller than the power output of existing WECs. For example, the nominal power output of the Oyster is 800 kW for a 26 m wide device, [39]. Therefore, PWECs cannot replace more traditional converters, rather they can be used in addition to them, to supply low-power applications such as LEDs, wireless routers, buoys and sensors. Coupled to traditional devices, PWECs offer the advantage of being low maintenance (the power is generated directly on the device without the need of an additional PTO mechanism) and versatile (they can be employed to increase wave damping around offshore oil platforms and near shore breakwaters).

Also, the mathematical model has been developed making several simplifying assumptions. Both the influence of the breakwater in section 4.1 and the clamped structures in section 4.2 has been neglected, even if in reality these might induce wave breaking, which could be analysed with computational fluid dynamics (CFD) software. Also the analysis was performed in the framework of a linearised theory for both the plate deformation and the wave motion. Close to resonance, the displacements of the plate might become significant and a non-linear analysis should be carried out to refine the power output predictions, [40]. In fact close to resonance, viscosity cannot be neglected, hence the hypotesis of potential flow is not valid anymore. In this case alternative methods must be used such as visco-potential flow theory or computational fluid dynamics (CFD), [27]. If there are significant displacements of the plate, the effect of viscosity and the associated turbulence, determine a reduction of power peaks because part of the energy is

dissipated and therefore cannot be harvested by the converter.

Finally I modelled deformations of the flexible plate as purely two-dimensional, hence the case of obliquely incident waves has not been considered. To verify the importance of three-dimensional effects, a full numerical model based on a finite-element approximation of the boundary-value problem should be derived, which, on the other hand cannot provide a valuable physical insights into the problem as the semi-analytical approach I used in the framework of this thesis.

The FBWEC is a novel floating wave energy converter which can be easily integrated in hybrid multi-energy platforms. In this thesis I reduced the complexity of the core technology of the device with the aim to investigate its hydro-mechanical behaviour performing the analysis in a two-dimensional space and considering the controlled vertical movement of a single floater. I derived analytically the radiation problem for a single row of interconnected floaters and I obtained a numerical characterisation of the radiated wave amplitudes. The goal of this study was to implement mathematical techniques to approach a 2D wave-interaction problem for a novel WEC in order to create the basis for a complex 3D analysis of the system. Mathematically, I derived a semi-analytical model for a FBWEC by using solution method based on the combination of both matching potentials and integral equations. In particular, due to the configuration of the system which is characterised by a floating blanket on the free surface in correspondence of a ocean step, I split the fluid domain in internal and external regions and I solved the radiation problems related to these two areas, respectively.

The fluid domain below the floating device and above the ocean step is regular and uniform (no tip singularities), therefore the method of matching potentials is still a valid way to address the problem and yields a valuable physical insights. On the contrary, singularity issues definitely occur both at the edges of the floater blanket and at the corners of the ocean step, hence I derived the governing equations of the radiation problem in the external regions by using a method based on the integral equations. Thus, I obtained two integral equations, on both left and right of the device respectively, and I combined them by means of useful mathematical identities. The resulting relation was a Fredholm integral equation of the first kind (ill-posed problem i.e. it admits an unstable solution with re-

spect to small variations in the right-hand side of the equation), therefore I used the Lavrentiev regularisation method to obtain an integral equation of the second kind [36] which I solved adopting a Galerkin approach [24].

Numerical simulations have been generated for symmetric devices by means of suitable Matlab codes showing an excellent agreement with previous results obtained with different mathematical methods, see [9]. In addition I identified the behaviour of the far-field amplitude of the radiated wave by a 2D floater blanket through a parametrical analysis in order to find optimal device configurations related both to the geometry of the converter and to the ocean environment. In particular I investigated the influence of the ocean shelf, the length of the floaters, the ratio between the length of the oscillating body and the overall length of the blanket and finally the ratio between the water depth and the height of the ocean step. Note that the obtained results offer a valuable physical insight into the problem even if I made simplifying assumptions. In fact I neglected the influence of the supporting structure and mooring lines of the the first and last floating bodies on the wave field. Also I assumed no-mass elements and I ignored the effect of the hinges used to connect the floaters.

Once the radiation problem has been solved, I must even solve the diffraction problem (discussed in appendix D). This will allow me to derive the equations of motion for all the floater elements which will form a system of linear equations to calculate the power output of the system. I suggest to approach this procedure directly in a 3D case for the following reasons: first, because I want to examine complex interactions between floaters in possible real configurations which obviously require the consideration of all three dimensions; also it would be interesting to show the existence of trapped modes which represent free oscillations with finite energy of the fluid surrounding the structure and this is of relevant interest in a 3D system; finally, mathematically, I would solve 3D integral equations by using a Fourier-Galerkin expansion method, which basically involves the solution of two separated problems i.e. one along the x-axis, the other one along the y-axis adopting a Galerkin approach and a Fourier approach, respectively. Note that along the x direction I expect the identical 2D problem already solved in chapter 5 due to the same dynamic of the system. Therefore, this will form the starting

point to address the 3D analysis of a floater blanket wave energy converter in a future research project.

7.1 Future research directions

Taking inspiration from the results we achieved during the past three years of doctoral experience, I suggest the following future research directions for both the piezoelectric and the floater blanket wave energy converters:

PWEC

- Find optimal device configuration determining the parametric behaviour of the system. In subsection 4.3.1 I approached a parametric analysis with regard to different water depth d'. Other parameters (e.g. α, β, ξ, ω, h, r, etc.) could be considered in a large extent of the parametric space, therefore genetic algorithms seem a good alternative to map the parametric behaviour of the system and identify areas of high-quality solutions in the space of parameters.
- Develop a full numerical model based on a finite-element approximation of the boundary-value problem. This will allow me to easily extend the analysis to handle arbitrary geometrical shapes of the plate in three dimensions.

FBWEC

- Combine solutions of radiation and diffraction problems to obtain a system of linear equations describing the motion of each floater directly in 3D.
- Calculate the power output of the system and all the quantities of engineering interest (e. g. spatial displacement of the blanket, spatial component of the free-surface elevation)
- Identify and investigate the existence of trapped modes and the benefits on the power output of the system.
- Derive and solve semi-analytical problems considering the vertical movement of the first and the last element of a single row of the floater elements.

- Combine the movement of two (or more) floater elements and analyse the overall behaviour of the system in order to complete the hydro-mechanical characterisation of the device.

Appendices

Note that in the framework of this thesis, variables with primes denote physical quantities. In appendices B and D primes are dropped for simplicity. Also I assume that the wave forcing is harmonic with frequency ω, therefore I factorise out the time variable as in subsection 5.1.2.

Appendix A

Matlab codes

Here I provide some details on the Matlab codes used to identify the numerical solutions and to determine all the quantities of engineering interest for a piezoelectric wave energy harvester moored on a breakwater.

```
%% PIEZODISP - Dispersion relation for piezoelectric plates in waves
%  Numerical solution with Newton-Raphson method

%% INPUT


% Input data
prompt1 = {'Wave period T (s)','Wave amplitude A (m)','Water depth h (m)'};
name1 = 'Insert wave data';
numlines = 1;
defaultanswer1 = {'5','1','10'};

prompt2 = {'Plate submergence d (m)','Plate lentgh L (m)','Substrate Young Modulus E_0 (N/m^2)','Substrate Poisson ratio \nu_0',...
 'Substrate thickness d_0 (m)','Substrate density \rho_0 (kg/m^3)'};
```

```
15 name2 = 'Insert plate data';
16 defaultanswer2 = {'2','10','3.2e6','0.48','1e-2','1250'};
17
18 prompt3 = {'Young Modulus E_p (N/m^2)','Poisson ratio \nu_0
       ','Patch thickness d_p (m)',...
19      'Patch density \rho_p (kg/m^3)','Piezo constant d_{31}
          (Coul/N)','Relative permittivity \epsilon_r','
          Conductance G (S m^{-2})'};
20 name3 = 'Insert patch data';
21 defaultanswer3 = {'8.3e9','0.18','110e-6','1780','22e-12','
       10','3.9856e-7'};
22
23 prompt4 = {'Max iterations','Tolerance'};
24 name4 = 'Insert numerical analysis data';
25 defaultanswer4 = {'200','1e-9'};
26
27
28 % Physical quantities
29 Tp  = str2double(answer1{1});          % Wave period
30 Ap  = str2double(answer1{2});          % Wave amplitude
31 hp  = str2double(answer1{3});          % Water depth
32
33 dp  = str2double(answer2{1});          % Plate submergence
34 Lp  = str2double(answer2{2});          % Plate length
35 E0p = str2double(answer2{3});          % Substrate Young's
       modulus
36 nu0 = str2double(answer2{4});          % Substrate Poisson
       's ratio
37 d0p = str2double(answer2{5});          % Substrate
       thickness
38 r0p = str2double(answer2{6});          % Substrate density
39
```

```
40 Epp = str2double(answer3{1});          % Patch Young's
       modulus
41 nup = str2double(answer3{2});          % Patch Poisson's
       ratio
42 dpp = str2double(answer3{3});          % Patch thickness
43 rpp = str2double(answer3{4});          % Patch density
44 d31 = str2double(answer3{5});          % Piezoelectric
       constant
45 epr = str2double(answer3{6});          % Relative
       Permittivity
46 Gp  = str2double(answer3{7});          % Conductance
47
48 Nit = str2double(answer4{1});       % Max iterations
49 tol = str2double(answer4{2});       % Tolerance
50
51 % Physical constants
52 rho = 1030;                          % Water density (kg/m^3)
53 g   = 9.807;                         % Gravity acc (m/s^2)
54 ep0 = 8.8541878176e-12;              % Vacuum permitt (F/m)
55
56 eps = epr*ep0;                       % Permittivity (F/m)
57
58 e31 = d31*Epp/(1-nup);               % Piezo constant (C/m^2)
59
60 mup = (2*rpp*dpp+r0p*d0p);           % Surf density (Kg/m^2)
61
62 Bp = (E0p* d0p^3)/(12*(1-nu0^2)) ...
63      +2* (Epp*dpp)/(1-nup^2) ...
64      *(d0p^2/4+ d0p*dpp/2+ dpp^2/3);% Flexural rig (N*m)
65
66 Kip = e31* (d0p+dpp)/2;              % Piezo coup coeff (C/m)
67
```

```
68 Cp = eps/(2*dpp);                    % Capacitance (F/m^2)
69
70 % Nondimensional parameters
71 al = Kip/sqrt(Bp*Cp);
72 be = Bp/(Lp^3*mup*g);
73 ga = sqrt(g*Lp^3*mup/Bp);
74 r  = rho*Lp/mup;
75 xi = Cp/Gp* sqrt(g/Lp);
76
77 % Nondimensional variables
78 h  = hp/Lp;                          % Water depth
79 d  = dp/Lp;                          % Plate submergence
80 T  = sqrt(g/Lp)* Tp;                 % Wave period
81 om = 2*pi/T;                        % Wave frequency
82
83 %% NUMERICAL SOLUTION
84
85 disp('-- Numerical Analysis--')
86
87 % Dispersion relation and derivatives
88
89 f = (@(x,y) real( ((be*(1+al^2)-al^2/(ga^2*(1-1i*om*xi)))
       .*(x+1i*y).^4-om^2).*...
90       (om^2.*(x+1i*y).*cosh((x+1i*y)*d)-(x+1i*y).^2.*sinh((x
             +1i*y)*d)).*tanh((x+1i*y)*(h-d))+...
91       -om^2*r*(om^2.*cosh((x+1i*y)*d)-(x+1i*y).*sinh((x+1i*y)
             *d)+...
92       -((x+1i*y).*cosh((x+1i*y)*d)-om^2.*sinh((x+1i*y)*d)).*
             tanh((x+1i*y)*(h-d))) ));
93
94 dfdx = (@(x,y) 4*real(tanh((d - h)*(x + y*1i))*(be*(al^2 +
       1) + al^2/...
```

```
95      (ga^2*(- 1 + om*xi*1i)))*(sinh(d*(x + y*1i))*(x + y*1i)
            ^2 -...
96      om^2*cosh(d*(x + y*1i))*(x + y*1i))*(x + y*1i)^3) -
            real(tanh((d - h)*...
97      (x + y*1i))*((be*(al^2 + 1) + al^2/(ga^2*(- 1 + om*xi*1
            i)))*(x + y*1i)^4 - om^2)...
98      *(om^2*cosh(d*(x + y*1i)) - sinh(d*(x + y*1i))*(2*x + y
            *2i) - d*...
99      cosh(d*(x + y*1i))*(x + y*1i)^2 + d*om^2*sinh(d*(x + y
            *1i))*(x + y*1i))) -...
100     real(((be*(al^2 + 1) + al^2/(ga^2*(- 1 + om*xi*1i)))*(x
             + y*1i)^4 - om^2)*...
101     (sinh(d*(x + y*1i))*(x + y*1i)^2 - om^2*cosh(d*(x + y*1
            i))*(x + y*1i))*...
102     (d - h)*(tanh((d - h)*(x + y*1i))^2 - 1)) - real(om^2*r
            *(- sinh(d*(x + y*1i)) +...
103     tanh((d - h)*(x + y*1i))*(- d*cosh(d*(x + y*1i))*om^2 +
             cosh(d*(x + y*1i)) +...
104     d*sinh(d*(x + y*1i))*(x + y*1i)) + (sinh(d*(x + y*1i))*
            om^2 - cosh(d*(x + y*1i))*...
105     (x + y*1i))*(d - h)*(tanh((d - h)*(x + y*1i))^2 - 1) -
            d*cosh(d*(x + y*1i))*...
106     (x + y*1i) + d*om^2*sinh(d*(x + y*1i))) );
107
108 dfdy = (@(x,y) real(tanh((d - h)*(x + y*1i))*(be*(al^2 + 1)
        + al^2/(ga^2*...
109     (- 1 + om*xi*1i)))*(sinh(d*(x + y*1i))*(x + y*1i)^2 -
            om^2*cosh(d*(x + y*1i))*...
110     (x + y*1i))*(x + y*1i)^3*4i) - real(tanh((d - h)*(x + y
            *1i))*((be*(al^2 + 1) +...
111     al^2/(ga^2*(- 1 + om*xi*1i)))*(x + y*1i)^4 - om^2)*(om
            ^2*cosh(d*(x + y*1i))*...
```

```
112     1i - sinh(d*(x + y*1i))*(x*2i - 2*y) - d*cosh(d*(x + y
            *1i))*(x + y*1i)^2*1i  +...
113     d*om^2*sinh(d*(x + y*1i))*(x + y*1i)*1i)) - real(om^2*r
            *(- sinh(d*(x + y*1i))*...
114     1i + tanh((d - h)*(x + y*1i))*(- d*cosh(d*(x + y*1i))*
            om^2*1i  +...
115     cosh(d*(x + y*1i))*1i + d*sinh(d*(x + y*1i))*(x + y*1i)
            *1i)  -...
116     d*cosh(d*(x + y*1i))*(x + y*1i)*1i + (sinh(d*(x + y*1i)
            )*om^2  -...
117     cosh(d*(x + y*1i))*(x + y*1i))*(tanh((d - h)*(x + y*1i)
            )^2 - 1)*...
118     (d*1i - h*1i) + d*om^2*sinh(d*(x + y*1i))*1i)) - real
            (((be*(al^2 + 1)  +...
119     al^2/(ga^2*(- 1 + om*xi*1i)))*(x + y*1i)^4 - om^2)*(
            sinh(d*(x + y*1i))*...
120     (x + y*1i)^2 - om^2*cosh(d*(x + y*1i))*(x + y*1i))*(
            tanh((d - h)*...
121     (x + y*1i))^2 - 1)*(d*1i - h*1i)) );
122
123 gg = (@(x,y) imag( ((be*(1+al^2)-al^2/(ga^2*(1-1i*om*xi)))
        .*(x+1i*y).^4-om^2).*...
124     (om^2*(x+1i*y).*cosh((x+1i*y)*d)-(x+1i*y).^2.*sinh((x+1
            i*y)*d)).*tanh((x+1i*y)*(h-d))+...
125     -om^2*r*(om^2.*cosh((x+1i*y)*d)-(x+1i*y).*sinh((x+1i*y)
            *d)+...
126     -((x+1i*y).*cosh((x+1i*y)*d)-om^2.*sinh((x+1i*y)*d)).*
            tanh((x+1i*y)*(h-d))) ));
127
128 dgdx = (@(x,y) 4*imag(tanh((d - h)*(x + y*1i))*(be*(al^2 +
        1) + al^2/...
```

```
129     (ga^2*(- 1 + om*xi*1i)))*(sinh(d*(x + y*1i))*(x + y*1i)
            ^2 - om^2*...
130     cosh(d*(x + y*1i))*(x + y*1i))*(x + y*1i)^3) - imag(
            tanh((d - h)*(x + y*1i))*...
131     ((be*(al^2 + 1) + al^2/(ga^2*(- 1 + om*xi*1i)))*(x + y
            *1i)^4 - om^2)*...
132     (om^2*cosh(d*(x + y*1i)) - sinh(d*(x + y*1i))*(2*x + y
            *2i) - d*cosh(d*...
133     (x + y*1i))*(x + y*1i)^2 + d*om^2*sinh(d*(x + y*1i))*(x
             + y*1i))) -...
134     imag(((be*(al^2 + 1) + al^2/(ga^2*(- 1 + om*xi*1i)))*(x
             + y*1i)^4 - om^2)*...
135     (sinh(d*(x + y*1i))*(x + y*1i)^2 - om^2*cosh(d*(x + y*1
            i))*(x + y*1i))*...
136     (d - h)*(tanh((d - h)*(x + y*1i))^2 - 1)) - imag(om^2*r
            *(- sinh(d*(x + y*1i)) +...
137     tanh((d - h)*(x + y*1i))*(- d*cosh(d*(x + y*1i))*om^2 +
             cosh(d*(x + y*1i)) +...
138     d*sinh(d*(x + y*1i))*(x + y*1i)) + (sinh(d*(x + y*1i))*
            om^2 -...
139     cosh(d*(x + y*1i))*(x + y*1i))*(d - h)*(tanh((d - h)*(x
             + y*1i))^2 - 1) -...
140     d*cosh(d*(x + y*1i))*(x + y*1i) + d*om^2*sinh(d*(x + y
            *1i)))) );
141
142 dgdy = (@(x,y) imag(tanh((d - h)*(x + y*1i))*(be*(al^2 + 1)
        + al^2/...
143     (ga^2*(- 1 + om*xi*1i)))*(sinh(d*(x + y*1i))*(x + y*1i)
            ^2 - om^2*...
144     cosh(d*(x + y*1i))*(x + y*1i))*(x + y*1i)^3*4i) - imag(
            tanh((d - h)*...
```

```
145     (x + y*1i))*((be*(al^2 + 1) + al^2/(ga^2*(- 1 + om*xi*1
            i)))*(x + y*1i)^4 -...
146     om^2)*(om^2*cosh(d*(x + y*1i))*1i - sinh(d*(x + y*1i))
            *(x*2i - 2*y) -...
147     d*cosh(d*(x + y*1i))*(x + y*1i)^2*1i + d*om^2*sinh(d*(x
            + y*1i))*...
148     (x + y*1i)*1i)) - imag(om^2*r*(- sinh(d*(x + y*1i))*1i
            + tanh((d - h)*...
149     (x + y*1i))*(- d*cosh(d*(x + y*1i))*om^2*1i + cosh(d*(x
            + y*1i))*1i +...
150     d*sinh(d*(x + y*1i))*(x + y*1i)*1i) - d*cosh(d*(x + y*1
            i))*(x + y*1i)*1i +...
151     (sinh(d*(x + y*1i))*om^2 - cosh(d*(x + y*1i))*(x + y*1i
            ))*(tanh((d - h)*...
152     (x + y*1i))^2 - 1)*(d*1i - h*1i) + d*om^2*sinh(d*(x + y
            *1i))*1i)) -...
153     imag(((be*(al^2 + 1) + al^2/(ga^2*(- 1 + om*xi*1i)))*(x
            + y*1i)^4 - om^2)*...
154     (sinh(d*(x + y*1i))*(x + y*1i)^2 - om^2*cosh(d*(x + y*1
            i))*(x + y*1i))*...
155     (tanh((d - h)*(x + y*1i))^2 - 1)*(d*1i - h*1i)) );
156
157
158 %% OUTPUT
159
160 % Parameters
161 disp(' ')
162 disp('--- Input Parameters ---')
163 disp(['Wave amplitude (m) = ', num2str(Ap)]);
164 disp(['Wave period (s) = ', num2str(Tp)]);
165 disp(['Water depth (m) = ', num2str(hp)]);
166 disp(' ')
```

```
167 disp(['Plate submergence (m) = ',num2str(dp)]);
168 disp(['Plate length (m) = ',num2str(Lp)]);
169 disp(['Substrate Young''s Modulus (N/m^2) = ',num2str(E0p)
    ]);
170 disp(['Substrate Poisson''s ratio = ',num2str(nu0)]);
171 disp(['Substrate thickness (m) = ',num2str(d0p)]);
172 disp(['Substrate density (kg/m^3) = ',num2str(r0p)]);
173 disp('')
174 disp(['Patch Young''s Modulus (N/m^2) = ',num2str(Epp)]);
175 disp(['Patch Poisson''s ratio = ',num2str(nup)]);
176 disp(['Patch thickness (m) = ',num2str(dpp)]);
177 disp(['Patch density (kg/m^3) = ',num2str(rpp)]);
178 disp(['Piezoelectric constant (Coul/N) = ',num2str(d31)]);
179 disp(['Relative permittivity = ',num2str(epr)]);
180 disp(['Conductance (S/m^2) = ',num2str(Gp)]);
181 disp(' ')
182 disp('--- Constants ---')
183 disp(['Permittivity (F/m) = ',num2str(eps)]);
184 disp(['Piezoelectric constant e31 (Coul/m^2) = ' ,num2str(
    e31)]);
185 disp(['Surface density (kg/m^2) = ',num2str(mup)]);
186 disp(['Flexural rigidity (N*m) = ',num2str(Bp)]);
187 disp(['Piezoel. coupling coeff. (Coul/m) = ',num2str(Kip)])
    ;
188 disp(['Capacitance (F/m^2) = ',num2str(Cp)]);
189 disp(' ')
```

```
1 %% PIEZOPOWER - Wave power extraction from piezoelectric
    flexible plate
2 % Numerical solution with matching potentials
3
4 %% INPUT
5 % Input parameters & dispersion relation
```

```
6  run PIEZODISP_fede.m
7
8  %% NUMERICAL SOLUTION
9  disp(' ')
10 disp('--- PIEZOPOWER ---')
11 disp(' ')
12 disp('--- Numerical system ---')
13 % Initialise values
14
15 N = length(Sn)-3;
16 % Dispersion relation for outer regions
17
18 % Propagating mode n=0
19 k = fzero(@(x) om^2-x* tanh(x*h), om.^2);
20 if max(abs(om.^2 - k.* tanh(k.*h))) > tol
21     disp('Warning: Dispersion relation not solved for n
       =0!!!')
22 end
23
24 % Evanescent modes n > 0
25 km = zeros(1,N);
26 for m = 1:1:N
27     km(m) = fzero(@(x) om^2 *h/x + tan(x), m*pi-tol);
28 end
29
30 km = km/h;
31
32 if max(abs(om^2 + km.* tan(km.*h))) > tol
33     disp('Warning: Dispersion relation not solved for n
       >0!!!')
34 end
35
```

```
36 Km = [k 1i*km].';
37
38 % - Building linear system -
39
40 % Initialise
41 M1 = zeros(N+1,N+3);
42 M2 = M1;
43 M3 = M2;
44 M4 = M3;
45
46 M5 = zeros(1,N+3);
47 M6 = M5;
48 M7 = M6;
49 M8 = M7;
50 M9 = M8;
51 M10 = M9;
52 M11 = M10;
53 M12 = M11;
54
55 a = (h+om^(-2)*(sinh(k*h))^2)^(1/2)/...
56    (2^(1/2)*cosh(k*h));
57
58 bmn = zeros(N+1,N+3);
59
60 % First N+1 rows
61 for m = 1:1:N+1
62     for n = 1:1:N+3
63
64         bmn(m,n) = (2^(1/2)*om^2*sinh(Sn(n)*(d - h))*(Sn(n)
               *...
65             (cosh(h*Km(m)) - cosh(Km(m)*(d - h))*cosh(d*Sn(
                 n))) +...
```

```
66                  sinh(Km(m)*(d - h))*Km(m)*sinh(d*Sn(n))))/((h
                        +...
67                  sinh(h*Km(m))^2/om^2)^(1/2)*(Km(m)^2 - Sn(n)^2)
                        ) -...
68                  (2^(1/2)*(cosh(d*Sn(n))*om^2 - Sn(n)*sinh(d*Sn(
                        n)))*...
69                  (cosh(Sn(n)*(d - h))*sinh(Km(m)*(d - h))*Km(m)
                        -...
70                  cosh(Km(m)*(d - h))*sinh(Sn(n)*(d - h))*Sn(n)))
                        /...
71                  ((h + sinh(h*Km(m))^2/om^2)^(1/2)*(Km(m)^2 - Sn
                        (n)^2)) -...
72                  (2^(1/2)*sinh(Sn(n)*(d - h))*Sn(n)*(Km(m)*(sinh
                        (h*Km(m)) +...
73                  sinh(Km(m)*(d - h))*cosh(d*Sn(n))) - cosh(Km(m)
                        *(d - h))*...
74                  Sn(n)*sinh(d*Sn(n))))/((h + sinh(h*Km(m))^2/om
                        ^2)^(1/2)*...
75                  (Km(m)^2 - Sn(n)^2));
76
77
78              M1(m,n) = exp(-1i*Sn(n))* (Sn(n) + Km(m))* bmn(m,n)
                    ;
79              M2(m,n) = -exp(1i*Sn(n))* (Sn(n) - Km(m))* bmn(m,n)
                    ;
80              M3(m,n) = Sn(n)* bmn(m,n);
81              M4(m,n) = -Sn(n)* bmn(m,n);
82          end
83      end
84
85      % Last 4 rows
86      for n = 1:1:N+3
```

```
87
88      % 4th last
89      M5(n) = (om^2* cosh(Sn(n)*d)- Sn(n)*sinh(Sn(n)*d))*...
90          Sn(n)*sinh(Sn(n)*(h-d));
91      M6(n) = (om^2* cosh(Sn(n)*d)- Sn(n)*sinh(Sn(n)*d))*...
92          Sn(n)*sinh(Sn(n)*(h-d));
93
94      % 3rd last
95      M7(n) = exp(-1i*Sn(n))* (om^2* cosh(Sn(n)*d)- Sn(n)*
            sinh(Sn(n)*d))*...
96          Sn(n)*sinh(Sn(n)*(h-d));
97      M8(n) = exp(1i*Sn(n))* (om^2* cosh(Sn(n)*d)- Sn(n)*sinh
            (Sn(n)*d))*...
98          Sn(n)*sinh(Sn(n)*(h-d));
99
100     % 2nd last
101     M9(n) = Sn(n)*(om^2* cosh(Sn(n)*d)- Sn(n)*sinh(Sn(n)*d)
            )*...
102         Sn(n)*sinh(Sn(n)*(h-d));
103     M10(n) = -Sn(n)*(om^2* cosh(Sn(n)*d)- Sn(n)*sinh(Sn(n)*
            d))*...
104         Sn(n)*sinh(Sn(n)*(h-d));
105
106     % last
107     M11(n) = Sn(n)*exp(-1i*Sn(n))* (om^2* cosh(Sn(n)*d)- Sn
            (n)*sinh(Sn(n)*d))*...
108         Sn(n)*sinh(Sn(n)*(h-d));
109     M12(n) = -Sn(n)*exp(1i*Sn(n))* (om^2* cosh(Sn(n)*d)- Sn
            (n)*sinh(Sn(n)*d))*...
110         Sn(n)*sinh(Sn(n)*(h-d));
111 end
112
```

```
113 % Full matrix
114 M = [M1 M2; M3 M4; M5 M6; M7 M8; M9 M10; M11 M12];
115
116 % Known term vector
117 B = zeros(2*N+6,1);
118 B(1) = 2*a*1i/om* (1i*k*sin(k) - Km(1)*cos(k));
119
120 % Regularised matrix
121 MR = zeros(2*N+6,2*N+6);
122 for m = 1:1:(2*N+6)
123     for n = 1:1:(2*N+6)
124     MR(m,n) = M(m,n)/max(M(m,:));
125     end
126 end
127
128 % Regularised k.t. vector
129 BR = B/max(M(1,:));
130
131 % Solution
132 X = linsolve(MR,BR);
133
134 % Plate coefficients
135 An = X(1:N+3);
136 Bn = X(N+4:(2*N+6));
137
138 % Error check
139 ers = max(abs(M*X-B));
140 disp(['Numerical system solved with max error: ',num2str(
      ers)]);
141
142 clear X
143
```

```
144 %  - RT Coefficients -
145
146 % Initialise
147 Rm = zeros(N+1,1);
148
149 au1 = zeros(N+1,N+3);
150 cm = Rm;
151
152
153 for m =1:1:N+1
154     cm(m) = (h+om^(-2)*(sinh(Km(m)*h))^2)^(1/2)/sqrt(2);
155     for n = 1:1:N+3
156         au1(m,n) = ( An(n)* exp(-1i*(Sn(n)+Km(m)))+...
157             Bn(n)* exp(1i*(Sn(n)-Km(m))) )*bmn(m,n);
158     end
159
160     Rm(m) = (2*1i*a/om* cos(k)*kroneckerDelta(sym(0),sym(m
        -1))*...
161         exp(-1i*Km(m))+ sum(au1(m,:)))/cm(m);
162 end
163
164 clear au1 au2
165
166 % - Wave field -
167
168 prompt7 = {'Min x'' ','Max x'' ','Spacing along x'' '};
169 name7 = 'Insert wave field data';
170 defaultanswer7 = {'-100','100','0.025'};
171 answer7 = inputdlg(prompt7,name7,numlines,defaultanswer7,
    options);
172
173 xpmin = str2num(answer7{1});
```

```
174 xpmax = str2num(answer7{2});
175 dx = str2num(answer7{3});
176
177 Xp = xpmin:dx:xpmax;
178
179 X = Xp/Lp;
180
181 X1 = X(X <= -1);
182 X2 = X(X >= -1 & X <= 0);
183
184
185 % Free-surface elevation
186
187 au1 = zeros(N+1,length(X1));
188 au2 = zeros(N+3,length(X2));
189
190 eta1 = zeros(1,length(X1));
191 eta2 = zeros(1,length(X2));
192
193
194 % D1
195 for j = 1:1:length(X1)
196     for m = 1:1:N+1
197     au1(m,j) = Rm(m)*exp(-1i*Km(m)*X1(j))*Km(m)*sinh(Km(m)*
          h);
198     end
199     eta1(j) = 2/om^2*k*tanh(k*h)*cos(k*X1(j))+ 1i/om* sum(
          au1(:,j));
200 end
201
202 % D2
203 for j = 1:1:length(X2)
```

```
204       for n = 1:1:N+3
205           au2(n,j) = (An(n)*exp(1i*Sn(n)*X2(j))+ Bn(n)*...
206               exp(-1i*Sn(n)*X2(j)))*om^2*Sn(n)*sinh(Sn(n)* (h
                      -d));
207       end
208     eta2(j) = 1i/om* sum(au2(:,j));
209 end
210
211
212 % Plate displacement
213 w = zeros(1,length(X2));
214 aup = zeros(N+3,length(X2));
215
216 for j = 1:1:length(X2)
217       for n = 1:1:N+3
218           aup(n,j) = (An(n)*exp(1i*Sn(n)*X2(j))+ Bn(n)*...
219               exp(-1i*Sn(n)*X2(j)))* ( om^2*cosh(Sn(n)*d)+...
220               -Sn(n)*sinh(Sn(n)*d) ) *Sn(n)* sinh(Sn(n)* (h-d
                      ));
221       end
222     w(j) = 1i/om* sum(aup(:,j));
223 end
224
225 clear aup
226
227 % Power
228
229 wxx = zeros(1,length(X2));
230 aup = zeros(N+3,length(X2));
231
232 for j = 1:1:length(X2)
233       for n = 1:1:N+3
```

```
234             aup(n,j) = (-Sn(n)^2*An(n)*exp(1i*Sn(n)*X2(j))-Sn(n
                    )^2*Bn(n)*...
235                 exp(-1i*Sn(n)*X2(j)))* ( om^2*cosh(Sn(n)*d)+...
236                 -Sn(n)*sinh(Sn(n)*d) ) *Sn(n)* sinh(Sn(n)* (h-d
                        ));
237         end
238         wxx(j) = 1i/om* sum(aup(:,j));
239 end
240
241 P = om^2/2* trapz(X2,(abs(al*wxx/(ga* (1-1i*om*xi)))).^2 );
242
243 % Dimensional variables
244
245 % Coordinates
246 X1p = X1*Lp;
247 X2p = X2*Lp;
248 %X4p = X4*Lp;
249
250 % Free-surface elevation
251 Z1p = real(eta1)*Ap;
252 Z2p = real(eta2)*Ap;
253
254 % Plate displacement
255 Wp = real(w)*Ap;
256
257 % Extracted power
258 Pp = (Ap*g)^2/Lp* mup*Cp/Gp* P;
259
260 disp(' ')
261 disp('--- Power output ---')
262 disp(['Extracted power (W/m) = ',num2str(Pp)]);
263 disp(['Power density (W/m^2) = ',num2str(Pp/(2*Lp))]);
```

```
264 disp('  ')
265
266 % Plots
267 figure
268 plot(X1p,Z1p,X2p,Z2p)
269 hold on
270 plot(X2p,-dp+Wp)
271 axis equal
```

Appendix B

Bessho-Newman relation

Using the expressions for $\phi_{Lm}(x,z)$ ans $\phi_{Rm}(x,z)$ derived respectively in sections 5.2.1 and 5.2.2 and looking at Fig. B.1, let the bounding surface $\partial\Omega$ be divided into the free surface S_F, the bottom B_0, the body $S_B \cup B_B$ and a vertical circular cylinder S_∞ with an arbitrary large radius. Note that in two dimensions, I consider $S_\infty^{\pm}$ be two vertical lines at $x \sim \pm\infty$.

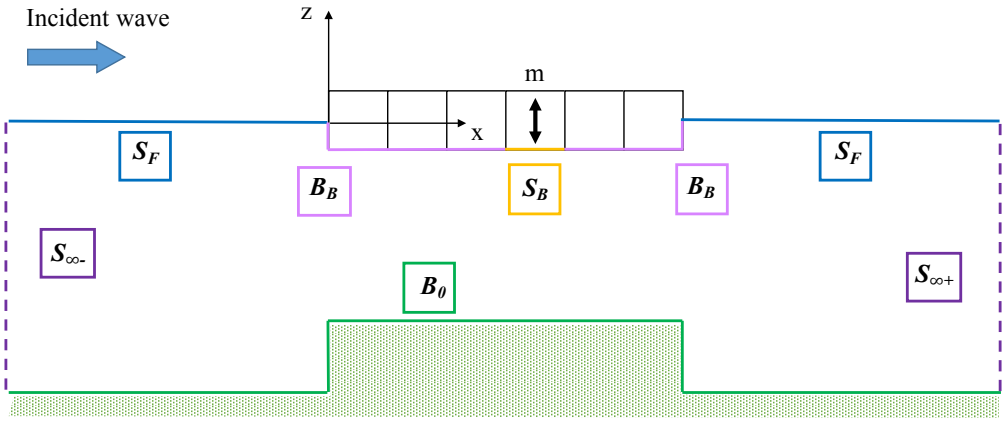

Figure B.1: Two-dimensional representation of the bounding surfaces of the FBWEC system as sum of the free surface S_F, the bottom B_0, the body $S_B \cup B_B$ and a vertical circular cylinder S_∞ with an arbitrary large radius.

The radiation problem (superscript R) for the system shown in Fig. B.1 is defined by

$$\nabla^2 \phi_m^R = 0 \qquad \text{in } \Omega, \tag{B.1}$$

$$\omega^2 \phi_m^R - g\phi_{mz}^R = 0 \qquad \text{in } S_F, \tag{B.2}$$

$$\frac{\partial \phi_m^R}{\partial n} = 0 \qquad \text{in } B_0 \cup B_B \tag{B.3}$$

and

$$\frac{\partial \phi_m^R}{\partial n} = 1 \qquad \text{in } S_B. \tag{B.4}$$

This yields the following asymptotic expressions for the radiation potentials:

$$\phi_m^R \sim a_{0m} e^{-ikx} Z_0(z), \qquad x \sim -\infty \tag{B.5}$$

and

$$\phi_m^R \sim b_{0m} e^{ik(x-L)} Z_0(z), \qquad x \sim \infty. \tag{B.6}$$

Similarly I can write the diffraction problem related to Fig. B.1:

$$\nabla^2(\phi^I + \phi^S) = 0 \qquad \text{in } \Omega, \tag{B.7}$$

$$\omega^2(\phi^I + \phi^S) - g(\phi^I + \phi^S)_z = 0 \qquad \text{in } S_F, \tag{B.8}$$

$$\frac{\partial(\phi^I + \phi^S)}{\partial n} = 0 \qquad \text{in } S_B \cup B_B \tag{B.9}$$

and

$$\frac{\partial(\phi^I + \phi^S)}{\partial n} = 0 \qquad \text{in } B_0, \tag{B.10}$$

where $\phi^I + \phi^S = \phi^D$ is the diffraction potential expressed as sum of the incident potential ϕ^I and the scattering potential ϕ^S. Solving the diffraction problem I obtain the asymptotic expressions (see [27]):

$$\phi^I + \phi^S = -\frac{igA_I}{\omega}\left(\frac{\cosh[k(z+h)]}{\cosh(kh)} e^{ikx} + RZ_0(z)e^{-ikx}\right), \qquad x \sim -\infty \tag{B.11}$$

and

$$\phi^I + \phi^S = -\frac{igA_I}{\omega} T Z_0(z) e^{ikx}, \qquad x \sim \infty, \tag{B.12}$$

where R and T are respectively the reflection and transmission coefficients and A_I is the amplitude of the incident wave. To obtain the Bessho-Newman relation for this problem, I shall apply Green's theorem to the radiation and diffraction problems set out above. For two twice-differentiable functions f and g, Green's theorem is

$$\int\int\int_\Omega (f\nabla^2 g - g\nabla^2 f)\,\mathrm{d}\Omega = \int\int_{\partial\Omega} \left(f\frac{\partial g}{\partial n} - g\frac{\partial f}{\partial n}\right)\mathrm{d}S, \tag{B.13}$$

where Ω is a closed volume, $\partial\Omega$ its boundary and $\mathbf{n}$ a unit normal to $\partial\Omega$ and outward from Ω, (see [27]). Let me choose $f = \phi^R - \phi^{R*}$ and $g = \phi^I + \phi^S$ where the $\cdot^*$ indicates the complex conjugate. Green's theorem becomes

$$\begin{aligned}\int\int\int_\Omega [(\phi^R - \phi^{R*})\nabla^2(\phi^I + \phi^S) - (\phi^I + \phi^S)\nabla^2(\phi^R - \phi^{R*})]\,\mathrm{d}\Omega = \\ \int\int_{S_{-\infty}\cup S_{+\infty}\cup S_F\cup S_B\cup B_0\cup B_B} \left[(\phi^R - \phi^{R*})\frac{\partial(\phi^I + \phi^S)}{\partial n} - (\phi^I + \phi^S)\frac{\partial(\phi^R - \phi^{R*})}{\partial n}\right]\mathrm{d}S.\end{aligned} \tag{B.14}$$

Using equation (B.1), its complex conjugate and (B.7), I get

$$\begin{aligned}&\int\int_{S_{-\infty}\cup S_{+\infty}} \left[(\phi^R - \phi^{R*})\frac{\partial(\phi^I + \phi^S)}{\partial n} - (\phi^I + \phi^S)\frac{\partial(\phi^R - \phi^{R*})}{\partial n}\right]\mathrm{d}S \\ &\quad + \int\int_{S_F} \left[(\phi^R - \phi^{R*})\frac{\partial(\phi^I + \phi^S)}{\partial n} - (\phi^I + \phi^S)\frac{\partial(\phi^R - \phi^{R*})}{\partial n}\right]\mathrm{d}S \\ &\quad + \int\int_{S_B} \left[(\phi^R - \phi^{R*})\frac{\partial(\phi^I + \phi^S)}{\partial n} - (\phi^I + \phi^S)\frac{\partial(\phi^R - \phi^{R*})}{\partial n}\right]\mathrm{d}S \\ &+ \int\int_{B_0\cup B_B} \left[(\phi^R - \phi^{R*})\frac{\partial(\phi^I + \phi^S)}{\partial n} - (\phi^I + \phi^S)\frac{\partial(\phi^R - \phi^{R*})}{\partial n}\right]\mathrm{d}S = 0.\end{aligned} \tag{B.15}$$

Using conditions (B.2-B.4) and (B.8-B.10), I obtain

$$\int\int_{S_{-\infty}} \left[(\phi^R - \phi^{R*})\frac{\partial(\phi^I + \phi^S)}{\partial n} - (\phi^I + \phi^S)\frac{\partial(\phi^R - \phi^{R*})}{\partial n}\right] \mathrm{d}S$$
$$+ \int\int_{S_{+\infty}} \left[(\phi^R - \phi^{R*})\frac{\partial(\phi^I + \phi^S)}{\partial n} - (\phi^I + \phi^S)\frac{\partial(\phi^R - \phi^{R*})}{\partial n}\right] \mathrm{d}S = 0. \quad \text{(B.16)}$$

Now I substitute the expressions for the radiation potentials ϕ^R, its complex conjugate and the diffraction potential $(\phi^I + \phi^S)$ at $x \sim \pm\infty$. Note that on $\pm\infty$, $\partial/\partial n = \pm\partial/\partial x$. Doing that I obtain the two-dimension Bessho-Newman relation that relates the unknown coefficients a_{0m} and b_{0m},

$$\frac{[h + g/\omega^2 \sinh^2(kh)]^{1/2}}{\sqrt{2}\cosh(kh)} a_{0m} + R a^*_{0m} + T b^*_{0m} = 0. \quad \text{(B.17)}$$

Appendix C

The basis functions

Following the method in [24], I choose the basis functions $p_n(z)$ such that they satisfy the physical requirement near the corner points A, B, C and D (see again Figg. 5.5 and 5.6). The edge conditions already stated in sections 5.2.1 and 5.2.2, tell me that the horizontal velocity of the fluid near the edge points has a cubic-root singularity. Also I seek functions such that the final forms of expressions occurring in the analysis become as simple as possible. Having said that, suitable basis functions for our problem can be chosen in terms of ultraspherical Gegenbauer polynomials $C_n^{1/6}(z)$ with weight function $(1-z^2)^{(-1/3)}$. They are characterised by the results

$$\int_{-1}^{1}(1-z^2)^{(-1/3)}C_n^{1/6}(z)\,\mathrm{d}z = \begin{cases} 0, & \text{for } n>0 \\ \frac{6\sqrt{\pi}\Gamma(\frac{2}{3})}{\Gamma(\frac{1}{6})}, & \text{for } n=0 \end{cases}. \tag{C.1}$$

In order to use the previous results I need to rewrite the integrals in equation (5.111) using ultraspherical Gegenbauer polynomials and changing variables to integrate in the interval $[-1,1]$. Therefore $p_n(u)$ and and $p_q(z)$ with $u, z \in [-h+c, -a]$ in (5.112) and (5.113) become respectively $p_n(v)$ and $p_q(w)$ with $v, w \in [-1,1]$ where

$$p_n(v) = (1-v^2)^{(-1/3)}C_n^{1/6}(v), \tag{C.2}$$

$$v = \frac{2u+h+a-c}{h-a-c} \qquad \text{and} \qquad w = \frac{2z+h+a-c}{h-a-c}. \tag{C.3}$$

Finally I can rewrite our approximated equation (5.111) as

$$\sum_{n=0}^{N} \alpha_{mn} \int_{-1}^{1} \int_{-1}^{1} (1-v^2)^{-1/3} C_n^{1/6}(v)(1-w^2)^{-1/3} C_n^{1/6}(w)$$
$$\mathcal{M}\left(\frac{v(h-a-c)-h-a+c}{2}, \frac{w(h-a-c)-h-a+c}{2}\right)\left(\frac{h-a-c}{2}\right)^2 \mathrm{d}v\,\mathrm{d}w =$$
$$\int_{-1}^{1} Z_0\left(\frac{w(h-a-c)-h-a+c}{2}\right)(1-w^2)^{-1/3} C_n^{1/6}(w)\left(\frac{h-a-c}{2}\right)\mathrm{d}w, \tag{C.4}$$

which can now be solved for the α_{mn}.

Appendix D

Diffraction

In the following chapter I formulate and solve the diffraction problem described in Fig. D.1. The FBWEC is now considered as a whole block and an incident wave is directed as the x-axis, see again Fig. D.1. Splitting the domain in three regions, let me define ϕ_L^D, ϕ^S and ϕ_R^D respectively spatial potential in region 1 (left), 2 (central), 3 (right) for the diffraction problem.

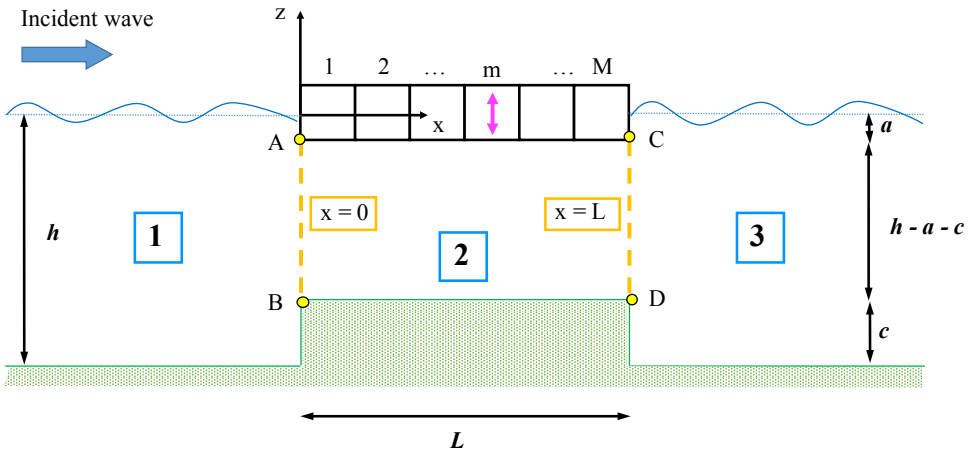

Figure D.1: Geometry of the FBWEC for the diffraction problem. Numbers 1, 2 and 3 denote respectively left, central and right regions in which I split the fluid domain to solve the problem.

In region 1 I have:

$$\nabla^2 \phi_L^D = 0, \qquad \text{in the fluid domain,} \tag{D.1}$$

$$\phi^D_{Lz} - \frac{\omega^2}{g}\phi^D_L = 0, \qquad z = 0, \tag{D.2}$$

$$\phi^D_{Lz} = 0, \qquad z = -h, \tag{D.3}$$

$$\phi^D_L \qquad \text{is outgoing}, \tag{D.4}$$

which yields

$$\phi^D_L(x,z) = \frac{igA_I}{\omega}\frac{\cosh[k(z+h)]}{cosh(kh)}e^{ikx} - \frac{igA_I}{\omega}RZ_0(z)e^{-ikx} + \sum_{p=1}^{+\infty} R_p Z_p(z)e^{k_p x}, \tag{D.5}$$

where $R = R_0$. Equations valid in the central region are

$$\nabla^2\phi^S = 0, \qquad \text{in the fluid domain}, \tag{D.6}$$

and

$$\phi^S_z = 0, \qquad z = -a, \qquad z = -h + c. \tag{D.7}$$

Following the same procedure used in section 5.1.2, I obtain

$$\phi^S_m(x,z) = G_0 x + H_0 + \sum_{p=1}^{+\infty}(G_p e^{-\tilde{k}_p x} + H_p e^{\tilde{k}_p x})\cos[\tilde{k}_p(z+h-c)]. \tag{D.8}$$

Finally, in region 3,

$$\nabla^2\phi^R_L = 0, \qquad \text{in the fluid domain}, \tag{D.9}$$

$$\phi^D_{Rz} - \frac{\omega^2}{g}\phi^D_R = 0, \qquad z = 0, \tag{D.10}$$

$$\phi^D_{Rz} = 0, \qquad z = -h, \tag{D.11}$$

$$\phi_R^D \qquad \text{is outgoing,} \tag{D.12}$$

which yields

$$\phi_R^D(x,z) = -\frac{igA_I}{\omega} T Z_0 e^{ik(x-L)} + \sum_{p=1}^{+\infty} T_p Z_p(z) e^{-k_p(x-L)}, \tag{D.13}$$

where $T \doteq T_0 e^{ikL}$. As I did in sections 5.2.1 and 5.2.2, I define the problem at the interface $x = 0$ and $x = L$ and I use a solution method based on the integral equations.

D.1 Interface $x = 0$

Looking again at Fig. D.1, at $x = 0$ I have:

$$\frac{\partial \phi_L^D}{\partial x} = 0, \qquad x = 0^-, \quad z \in (-h,\ -h+c), \quad z \in (-a,\ 0), \tag{D.14}$$

$$\phi_L^D = \phi^S, \qquad x = 0^-, \quad z \in (-h+c,\ -a), \tag{D.15}$$

$$\frac{\partial \phi_L^D}{\partial x} = \frac{\partial \phi^S}{\partial x}, \qquad x = 0, \quad z \in (-h+c,\ -a) \tag{D.16}$$

and

$$|\nabla \phi_L^D| = O(r^{-1/3}) \qquad \text{on A and B, see again Fig. D.1.} \tag{D.17}$$

Using the method in [24], let me now define

$$\frac{\partial \phi_L^D}{\partial x}(0^-, z) \doteq g_L(z), \qquad z \in (-h,\ 0). \tag{D.18}$$

Then (D.14) becomes

$$g_L(z) = 0, \qquad z \in (-h,\ -h+c), \quad z \in (-a,\ 0) \tag{D.19}$$

and (D.16) gives

$$g_L(z) = \left.\frac{\partial \phi^S}{\partial x}\right|_{x=0}, \qquad z \in (-h+c,\ -a). \tag{D.20}$$

Also, due to the edge condition described by (D.17), I must have the requirement that

$$g_L = O(|z+h-c|^{-1/3}), \qquad z \to -h+c \tag{D.21}$$

and

$$g_L = O(|z+a|^{-1/3}), \qquad z \to -a. \tag{D.22}$$

Substituting (D.5) in the definition (D.18) and rearranging, I get

$$\frac{kgA_I}{\omega} Z_0(z) \left[\frac{[h + \frac{g}{\omega^2}\sinh^2(kh)]^{1/2}}{\sqrt{2}\cosh(kh)} - R \right] + \sum_{p=1}^{+\infty} k_p R_p Z(z)_p = g_L(z). \tag{D.23}$$

Hence let me multiply by $Z_0(z)$, and integrate along z, to obtain

$$\frac{kgA_I}{\omega} \left[\frac{[h + \frac{g}{\omega^2}\sinh^2(kh)]^{1/2}}{\sqrt{2}\cosh(kh)} - R \right] = \int_{-h+c}^{-a} g_L(z) Z_0(z)\,\mathrm{d}z. \tag{D.24}$$

In the latter, condition (D.19) has been used and the orthogonality of the vertical modes Z_0 has been exploited. In addition, multiplying (D.23) by $Z_q(z)$, $q = 0, 1, 2...$ and integrating along z, yields

$$k_p R_p = \int_{-h+c}^{-a} g_L(z) Z_p(z)\,\mathrm{d}z. \tag{D.25}$$

Using the same method, conditions (D.15) and (D.20) yield respectively

$$G_p + H_p = \frac{2}{h-a-c} \left\{ \frac{-igA_I}{\omega} \Im_{0p} \left[\frac{[h + \frac{g}{\omega^2}\sinh^2(kh)]^{1/2}}{\sqrt{2}\cosh(kh)} + R \right] + \sum_{q=1}^{+\infty} R_q \Im_{qp} \right\} \tag{D.26}$$

and

$$H_p - G_p = \frac{2}{\tilde{k}_p(h-a-c)} \int_{-h+c}^{-a} g_L(z) \cos[\tilde{k}_p(z+h-c)]\,\mathrm{d}z, \tag{D.27}$$

where I exploited the orthogonality of cosines. In (D.26),

$$\Im_{0p} = \int_{-h+c}^{-a} Z_0(z) \cos[\tilde{k}_p(z+h-c)]\,\mathrm{d}z$$

and

$$\Im_{qp} = \int_{-h+c}^{-a} Z_q(z) \cos[\tilde{k}_p(z+h-c)]\,\mathrm{d}z.$$

Finally, the integral equations at the interface $x = 0$ can be obtained by substituting (D.5) and (D.8) in (D.16). This yields

$$\int_{-h+c}^{-a} g_L(u) \left\{ \frac{2}{h-a-c} \sum_{p=1}^{+\infty} \cos[\tilde{k}_p(u+h-c)] \cos[\tilde{k}_p(z+h-c)] - \sum_{p=1}^{+\infty} Z_p(u) Z_p(z) \right\} \mathrm{d}u + G_0 = Z_0(z) \frac{gkA_I}{\omega} \left\{ \frac{[h + \frac{g}{\omega^2}\sinh^2(kh)]^{1/2}}{\sqrt{2}\cosh(kh)} - R \right\}. \tag{D.28}$$

The amplitude coefficient G_0 can be determined by substituting (D.8) into (D.20) and integrating along z between $z = -h + c$ and $z = -a$:

$$G_0 = \frac{1}{h-a-c} \int_{-h+c}^{-a} g_L(z)\,\mathrm{d}z. \tag{D.29}$$

Now I substitute (D.29) in (D.28) and I get the integral equation:

$$\int_{-h+c}^{-a} G_L(u) \mathcal{M}(u,z)\,\mathrm{d}u = Z_0(z), \tag{D.30}$$

where

$$G_L(u) = \frac{g_L(u)}{\frac{gkA_I}{\omega} \left\{ \frac{[h + \frac{g}{\omega^2}\sinh^2(kh)]^{1/2}}{\sqrt{2}\cosh(kh)} - R \right\}} \tag{D.31}$$

and $\mathcal{M}(u,z)$ is real and symmetric in u and z and is expressed by (5.50).

D.2 Interface $x = L$

At the interface $x = L$ I have a similar problem to solve:

$$\frac{\partial \phi_R^D}{\partial x} = 0, \qquad x = L^+, \quad z \in (-h,\ -h + c), \quad z \in (-a,\ 0), \tag{D.32}$$

$$\phi_R^D = \phi^S, \qquad x = L^+, \quad z \in (-h + c,\ -a), \tag{D.33}$$

$$\frac{\partial \phi_R^D}{\partial x} = \frac{\partial \phi^S}{\partial x}, \qquad x = L, \quad z \in (-h + c,\ -a) \tag{D.34}$$

and

$$|\nabla \phi_R^D| = O(r^{-1/3}) \qquad \text{on C and D, see again Fig. D.1.} \tag{D.35}$$

Using again the method in [24], let me now define

$$\frac{\partial \phi_R^D}{\partial x}(L^+, z) \doteq g_R(z), \qquad z \in (-h,\ 0). \tag{D.36}$$

Then (D.32) becomes

$$g_R(z) = 0, \quad z \in (-h,\ -h + c) \quad \text{or} \quad z \in (-a,\ 0) \tag{D.37}$$

and (D.34) gives

$$g_R(z) = \left.\frac{\partial \phi^S}{\partial x}\right|_{x=0}, \qquad z \in (-h + c,\ -a). \tag{D.38}$$

Also, due to the edge condition described by (D.35), I must have the requirement that

$$g_R = O(|z + h - c|^{-1/3}), \qquad z \to -h + c \tag{D.39}$$

and

$$g_R = O(|z + a|^{-1/3}), \qquad z \to -a. \tag{D.40}$$

The integral equation at the interface $x = L$ is obtained following exactly the same procedure that I used at interface $x = 0$ as follows. Substituting (D.13) in the definition (D.36) and rearranging, I get

$$\frac{kgA_I}{\omega} T Z_0(z) - \sum_{p=1}^{+\infty} k_p T_p Z(z)_p = g_R(z). \tag{D.41}$$

Hence let me multiply by $Z_0(z)$, and integrate along z, to obtain

$$\frac{kgA_I}{\omega} T = \int_{-h+c}^{-a} g_R(z) Z_0(z)\, \mathrm{d}z. \tag{D.42}$$

In the latter, condition (D.37) has been used and the orthogonality of the vertical modes Z_0 has been exploited. In addition, multiplying (D.41) by $Z_q(z)$, $q = 0, 1, 2...$ and integrating along z, yields

$$-k_p R_p = \int_{-h+c}^{-a} g_L(z) Z_p(z)\, \mathrm{d}z. \tag{D.43}$$

Using the same method, conditions (D.33) and (D.38) yield respectively

$$G_p e^{-\tilde{k}_p L} + H_p e^{\tilde{k}_p L} = \frac{2}{h - a - c} \left[\frac{-igA_I}{\omega} T \Im_{0p} + \sum_{q=1}^{+\infty} T_q \Im_{qp} \right] \tag{D.44}$$

and

$$H_p e^{\tilde{k}_p L} - G_p e^{-\tilde{k}_p L} = \frac{2}{\tilde{k}_p (h - a - c)} \int_{-h+c}^{-a} g_R(z) \cos[\tilde{k}_p (z + h - c)]\, \mathrm{d}z, \tag{D.45}$$

where I exploited the orthogonality of cosines. In (D.44),

$$\Im_{0p} = \int_{-h+c}^{-a} Z_0(z) \cos[\tilde{k}_p (z + h - c)]\, \mathrm{d}z$$

and

$$\Im_{qp} = \int_{-h+c}^{-a} Z_q(z) \cos[\tilde{k}_p (z + h - c)]\, \mathrm{d}z.$$

Finally, the integral equations at the interface $x = L$ can be obtained by substituting (D.13) and (D.8) in (D.34). This yields

$$\int_{-h+c}^{-a} g_R(u)\Bigg\{\frac{2}{h-a-c}\sum_{p=1}^{+\infty}\cos[\tilde{k}_p(u+h-c)]\cos[\tilde{k}_p(z+h-c)] - \sum_{p=1}^{+\infty} Z_p(u)Z_p(z)\Bigg\}\,\mathrm{d}u + G_0 = Z_0(z)T\frac{gkA_I}{\omega}. \tag{D.46}$$

The amplitude coefficient G_0 can be determined by substituting (D.8) into (D.38) and integrating along z between $z = -h + c$ and $z = -a$:

$$G_0 = \frac{1}{h-a-c}\int_{-h+c}^{-a} g_R(z)\,\mathrm{d}z. \tag{D.47}$$

Now I substitute (D.47) in (D.46) and I get the integral equation:

$$\int_{-h+c}^{-a} G_R(u)\mathcal{M}(u,z)\,\mathrm{d}u = Z_0(z), \tag{D.48}$$

where

$$G_R(u) = \frac{g_R(u)}{\frac{gkA_IT}{\omega}} \tag{D.49}$$

and $\mathcal{M}(u,z)$ is real and symmetric in u and z and is expressed by (5.50). Note that in section D.1, I found G_0 using (D.38), therefore this yields a relation between $g_L(z)$ and $g_R(z)$ as below.

$$\int_{-h+c}^{-a} G_L(u)\mathcal{M}(u,z)\,\mathrm{d}u = Z_0(z) = \int_{-h+c}^{-a} G_R(u)\mathcal{M}(u,z)\,\mathrm{d}u, \tag{D.50}$$

which can be written as

$$\int_{-h+c}^{-a} [G_L(u) - G_R(u)]\mathcal{M}(u,z)\,\mathrm{d}u = 0. \tag{D.51}$$

The latter implies that $G_L(u) = G_R(u)$, therefore

$$\frac{g_L(u)}{\frac{gkA_I}{\omega}\left\{\frac{[h+\frac{g}{\omega^2}\sinh^2(kh)]^{1/2}}{\sqrt{2}\cosh(kh)} - R\right\}} = \frac{g_R(u)}{\frac{gkA_IT}{\omega}}. \tag{D.52}$$

Also, I have

$$\frac{1}{h-a-c}\int_{-h+c}^{-a} g_L(z)\,\mathrm{d}z = G_0 = \frac{1}{h-a-c}\int_{-h+c}^{-a} g_R(z)\,\mathrm{d}z, \tag{D.53}$$

from which I obtain

$$\int_{-h+c}^{-a} g_L(z)\,\mathrm{d}z = \int_{-h+c}^{-a} g_R(z)\,\mathrm{d}z. \tag{D.54}$$

Now let me integrate (D.52) along z between $z=-h+c$ and $z=-a$ to get a relation between transmission T and reflection R coefficients:

$$T = \frac{[h+\frac{g}{\omega^2}\sinh^2(kh)]^{1/2}}{\sqrt{2}\cosh(kh)} - R. \tag{D.55}$$

In the latter, condition (D.54) has been used. Now I can conclude that (D.52) and (D.54) imply that

$$g_L(z) = g_R(z). \tag{D.56}$$

D.3 Summary of equations and unknowns of the diffraction problem

Here I present a summary of equations and unknowns which describe the diffraction problem of Fig. D.1:

$$\frac{kgA_I}{\omega}\left[\frac{[h+\frac{g}{\omega^2}\sinh^2(kh)]^{1/2}}{\sqrt{2}\cosh(kh)} - R\right] = \int_{-h+c}^{-a} g_L(z)Z_0(z)\,\mathrm{d}z, \tag{D.57}$$

$$k_pR_p = \int_{-h+c}^{-a} g_L(z)Z_p(z)\,\mathrm{d}z, \tag{D.58}$$

$$G_p + H_p = \frac{2}{h-a-c}\left\{\frac{-igA_I}{\omega}\Im_{0p}\left[\frac{[h+\frac{g}{\omega^2}\sinh^2(kh)]^{1/2}}{\sqrt{2}\cosh(kh)} + R\right] + \sum_{q=1}^{+\infty} R_q\Im_{qp}\right\}, \tag{D.59}$$

$$H_p - G_p = \frac{2}{\tilde{k}_p(h-a-c)} \int_{-h+c}^{-a} g_L(z) \cos[\tilde{k}_p(z+h-c)] \, \mathrm{d}z, \tag{D.60}$$

$$G_0 = \frac{1}{h-a-c} \int_{-h+c}^{-a} g_L(z) \, \mathrm{d}z, \tag{D.61}$$

$$\int_{-h+c}^{-a} G_L(u) \mathcal{M}(u,z) \, \mathrm{d}u = Z_0(z), \tag{D.62}$$

$$G_L(u) = \frac{g_L(u)}{\frac{gkA_I}{\omega} \left\{ \frac{[h+\frac{g}{\omega^2}\sinh^2(kh)]^{1/2}}{\sqrt{2}\cosh(kh)} - R \right\}}, \tag{D.63}$$

$$\frac{kgA_I}{\omega} T = \int_{-h+c}^{-a} g_R(z) Z_0(z) \, \mathrm{d}z, \tag{D.64}$$

$$-k_p R_p = \int_{-h+c}^{-a} g_L(z) Z_p(z) \, \mathrm{d}z, \tag{D.65}$$

$$G_p e^{-\tilde{k}_p L} + H_p e^{\tilde{k}_p L} = \frac{2}{h-a-c} \left[\frac{-igA_I}{\omega} T \Im_{0p} + \sum_{q=1}^{+\infty} T_q \Im_{qp} \right], \tag{D.66}$$

$$H_p e^{\tilde{k}_p L} - G_p e^{-\tilde{k}_p L} = \frac{2}{\tilde{k}_p(h-a-c)} \int_{-h+c}^{-a} g_R(z) \cos[\tilde{k}_p(z+h-c)] \, \mathrm{d}z, \tag{D.67}$$

$$\int_{-h+c}^{-a} G_R(u) \mathcal{M}(u,z) \, \mathrm{d}u = Z_0(z), \tag{D.68}$$

$$G_R(u) = \frac{g_R(u)}{\frac{gkA_I T}{\omega}}, \tag{D.69}$$

$$T = \frac{[h+\frac{g}{\omega^2}\sinh^2(kh)]^{1/2}}{\sqrt{2}\cosh(kh)} - R, \tag{D.70}$$

$$g_L(z) = g_R(z). \tag{D.71}$$

D.4 Reflection coefficient

Once G_L is determined from the integral equation (D.62), g_L can be found by using (D.63) which yields

$$g_L = G_L(u)\frac{gkA_I}{\omega}\left[\frac{[h+\frac{g}{\omega^2}\sinh^2(kh)]^{1/2}}{\sqrt{2}\cosh(kh)} - R\right]. \tag{D.72}$$

Substituting the latter in (D.60) I obtain

$$H_p - G_p = \frac{2}{\tilde{k}_p(h-a-c)}\int_{-h+c}^{-a} G_L(z)\frac{gkA_I}{\omega}\left[\frac{[h+\frac{g}{\omega^2}\sinh^2(kh)]^{1/2}}{\sqrt{2}\cosh(kh)} - R\right] \cos[\tilde{k}_p(z+h-c)]\,\mathrm{d}z. \tag{D.73}$$

Now I sum (D.73) and (D.59) to obtain an expression for H_p:

$$H_p = \frac{1}{h-a-c}\left\{\frac{1}{\tilde{k}_p}\int_{-h+c}^{-a} G_L(z)\frac{gkA_I}{\omega}\left[\frac{[h+\frac{g}{\omega^2}\sinh^2(kh)]^{1/2}}{\sqrt{2}\cosh(kh)} - R\right] \cos[\tilde{k}_p(z+h-c)]\,\mathrm{d}z + \sum_{p=1}^{+\infty} R_p \Im_{pq} - \frac{igA_I}{\omega}\Im_{0p}\left[\frac{[h+\frac{g}{\omega^2}\sinh^2(kh)]^{1/2}}{\sqrt{2}\cosh(kh)} + R\right]\right\}. \tag{D.74}$$

In order to rewrite the latter as function of the only unknown R, I use (D.58) and (D.72) to get an expression for R_p:

$$R_p = \frac{1}{k_p}\int_{-h+c}^{-a} G_L(z)\frac{gkA_I}{\omega}\left[\frac{[h+\frac{g}{\omega^2}\sinh^2(kh)]^{1/2}}{\sqrt{2}\cosh(kh)} - R\right] Z_p(z)\,\mathrm{d}z, \tag{D.75}$$

therefore

$$H_p = \frac{1}{h-a-c}\Bigg\{\frac{1}{\tilde{k}_p}\int_{-h+c}^{-a} G_L(z)\frac{gkA_I}{\omega}\left[\frac{[h+\frac{g}{\omega^2}\sinh^2(kh)]^{1/2}}{\sqrt{2}\cosh(kh)} - R\right]$$
$$\cos[\tilde{k}_p(z+h-c)]\,\mathrm{d}z + \sum_{p=1}^{+\infty}\frac{1}{k_p}\int_{-h+c}^{-a} G_L(z)\frac{gkA_I}{\omega}\left[\frac{[h+\frac{g}{\omega^2}\sinh^2(kh)]^{1/2}}{\sqrt{2}\cosh(kh)} - R\right]$$
$$Z_p(z)\Im_{qp}\,\mathrm{d}z - \frac{igA_I}{\omega}\Im_{0p}\left[\frac{[h+\frac{g}{\omega^2}\sinh^2(kh)]^{1/2}}{\sqrt{2}\cosh(kh)} + R\right]\Bigg\}. \tag{D.76}$$

Note that $g_R(z) = g_L(z) = G_L(u)\frac{gkA_I}{\omega}\left[\frac{[h+\frac{g}{\omega^2}\sinh^2(kh)]^{1/2}}{\sqrt{2}\cosh(kh)} - R\right]$ and if I substitute this in (D.67), I obtain

$$H_p e^{\tilde{k}_p L} - G_p e^{-\tilde{k}_p L} = \frac{2}{\tilde{k}_p(h-a-c)}\int_{-h+c}^{-a} G_L(u)\frac{gkA_I}{\omega}\left[\frac{[h+\frac{g}{\omega^2}\sinh^2(kh)]^{1/2}}{\sqrt{2}\cosh(kh)} - R\right]$$
$$\cos[\tilde{k}_p(z+h-c)]\,\mathrm{d}z, \tag{D.77}$$

which I can sum to (D.66) to get another expression for H_p:

$$H_p = \frac{1}{e^{\tilde{k}_p L}(h-a-c)}\Bigg\{\frac{1}{\tilde{k}_p}\int_{-h+c}^{-a} G_L(z)\frac{gkA_I}{\omega}\left[\frac{[h+\frac{g}{\omega^2}\sinh^2(kh)]^{1/2}}{\sqrt{2}\cosh(kh)} - R\right]$$
$$\cos[\tilde{k}_p(z+h-c)]\,\mathrm{d}z + \sum_{p=1}^{+\infty} T_p\Im_{pq} - \frac{igA_I}{\omega}\Im_{0p}T\Bigg\}. \tag{D.78}$$

Now, (D.71), (D.58) and (D.65) imply that $R_p = -T_p$, therefore,

$$H_p = \frac{1}{e^{\tilde{k}_p L}(h-a-c)}\Bigg\{\frac{1}{\tilde{k}_p}\int_{-h+c}^{-a} G_L(z)\frac{gkA_I}{\omega}\left[\frac{[h+\frac{g}{\omega^2}\sinh^2(kh)]^{1/2}}{\sqrt{2}\cosh(kh)}-R\right]$$
$$\cos[\tilde{k}_p(z+h-c)]\,\mathrm{d}z - \sum_{p=1}^{+\infty}\frac{1}{k_p}\int_{-h+c}^{-a} G_L(z)\frac{gkA_I}{\omega}\left[\frac{[h+\frac{g}{\omega^2}\sinh^2(kh)]^{1/2}}{\sqrt{2}\cosh(kh)}-R\right]$$
$$Z_p(z)\Im_{pq}\,\mathrm{d}z - \frac{igA_I}{\omega}\Im_{0p}\left[\frac{[h+\frac{g}{\omega^2}\sinh^2(kh)]^{1/2}}{\sqrt{2}\cosh(kh)}-R\right]\Bigg\}. \tag{D.79}$$

In the latter I used (D.70) and (D.75). Finally I obtained two expressions for H_p, (D.76) and (D.79), which can be matched to obtain the reflection coefficient R as below:

$$\frac{1}{h-a-c}\Bigg\{\frac{1}{\tilde{k}_p}\int_{-h+c}^{-a} G_L(z)\frac{gkA_I}{\omega}\left[\frac{[h+\frac{g}{\omega^2}\sinh^2(kh)]^{1/2}}{\sqrt{2}\cosh(kh)}-R\right]\cos[\tilde{k}_p(z+h-c)]\,\mathrm{d}z+$$
$$\sum_{p=1}^{+\infty}\frac{1}{k_p}\int_{-h+c}^{-a} G_L(z)\frac{gkA_I}{\omega}\left[\frac{[h+\frac{g}{\omega^2}\sinh^2(kh)]^{1/2}}{\sqrt{2}\cosh(kh)}-R\right]Z_p(z)\Im_{qp}\,\mathrm{d}z - \frac{igA_I}{\omega}\Im_{0p}$$
$$\left[\frac{[h+\frac{g}{\omega^2}\sinh^2(kh)]^{1/2}}{\sqrt{2}\cosh(kh)}+R\right]\Bigg\} = \frac{1}{e^{\tilde{k}_p L}(h-a-c)}\Bigg\{\frac{1}{\tilde{k}_p}\int_{-h+c}^{-a} G_L(z)\frac{gkA_I}{\omega}$$
$$\left[\frac{[h+\frac{g}{\omega^2}\sinh^2(kh)]^{1/2}}{\sqrt{2}\cosh(kh)}-R\right]\cos[\tilde{k}_p(z+h-c)]\,\mathrm{d}z - \sum_{p=1}^{+\infty}\frac{1}{k_p}\int_{-h+c}^{-a} G_L(z)\frac{gkA_I}{\omega}$$
$$\left[\frac{[h+\frac{g}{\omega^2}\sinh^2(kh)]^{1/2}}{\sqrt{2}\cosh(kh)}-R\right]Z_p(z)\Im_{pq}\,\mathrm{d}z - \frac{igA_I}{\omega}\Im_{0p}\left[\frac{[h+\frac{g}{\omega^2}\sinh^2(kh)]^{1/2}}{\sqrt{2}\cosh(kh)}-R\right]\Bigg\}, \tag{D.80}$$

which I can be simplified to

$$\left(1-\frac{1}{e^{\tilde{k}_pL}}\right)\frac{k}{\tilde{k}_p}\frac{[h+\frac{g}{\omega^2}\sinh^2(kh)]^{1/2}}{\sqrt{2}\cosh(kh)}\int_{-h+c}^{-a}G_L(z)\cos[\tilde{k}_p(z+h-c)]\,\mathrm{d}z-$$
$$\left(1-\frac{1}{e^{\tilde{k}_pL}}\right)\frac{k}{\tilde{k}_p}R\int_{-h+c}^{-a}G_L(z)\cos[\tilde{k}_p(z+h-c)]\,\mathrm{d}z+\left(1+\frac{1}{e^{\tilde{k}_pL}}\right)k$$
$$\frac{[h+\frac{g}{\omega^2}\sinh^2(kh)]^{1/2}}{\sqrt{2}\cosh(kh)}\sum_{p=1}^{+\infty}\frac{\Im_{pq}}{k_p}\int_{-h+c}^{-a}G_L(z)Z_p(z)\,\mathrm{d}z-\left(1+\frac{1}{e^{\tilde{k}_pL}}\right)kR$$
$$\sum_{p=1}^{+\infty}\frac{\Im_{pq}}{k_p}\int_{-h+c}^{-a}G_L(z)Z_p(z)\,\mathrm{d}z-2i\Im_{0p}R=0 \quad \text{(D.81)}$$

and finally I can obtain the following expression for R:

$$R=\frac{\frac{[h+\frac{g}{\omega^2}\sinh^2(kh)]^{1/2}}{\sqrt{2}\cosh(kh)}\left\{\left(1-\frac{1}{e^{\tilde{k}_pL}}\right)\frac{k}{\tilde{k}_p}\int_{-h+c}^{-a}G_L(z)\cos[\tilde{k}_p(z+h-c)]\,\mathrm{d}z+\right.}{\left(1-\frac{1}{e^{\tilde{k}_pL}}\right)\frac{k}{\tilde{k}_p}\int_{-h+c}^{-a}G_L(z)\cos[\tilde{k}_p(z+h-c)]\,\mathrm{d}z+\left(1+\frac{1}{e^{\tilde{k}_pL}}\right)k}$$
$$\frac{\left.\left(1+\frac{1}{e^{\tilde{k}_pL}}\right)k\sum_{p=1}^{+\infty}\frac{\Im_{pq}}{k_p}\int_{-h+c}^{-a}G_L(z)Z_p(z)\,\mathrm{d}z\right\}}{\sum_{p=1}^{+\infty}\frac{\Im_{pq}}{k_p}\int_{-h+c}^{-a}G_L(z)Z_p(z)\,\mathrm{d}z+2i\Im_{0p}}. \quad \text{(D.82)}$$

References

[1] Carnegie's ceto. https://www.carnegiece.com.

[2] Ipcc: Climate change 2014: Synthesis report. contribution of working groups i, ii and iii to the fifth assessment report of the intergovernmental panel on climate change [core writing team, r.k. pachauri and l.a. meyer (eds.)]. ipcc, geneva, switzerland, 151 pp (2014).

[3] Ocean grazer http://www.oceangrazer.com.

[4] Owc pico power plant http://www.pico-owc.net.

[5] Seabased https://www.seabased.com.

[6] Aurelien Babarit. *Ocean Wave Energy Conversion: resource, technologies and performance*. ISTE Press - Elsevier, 1st edition, 2017.

[7] H Behera and T Sahoo. Hydroelastic analysis of gravity wave interaction with submerged horizontal flexible porous plate. *Journal of Fluids and Structures*, 54:643–660, 2015.

[8] P Bisegna, G Caruso, and F Maceri. Optimized electric networks for vibration damping of piezoactuated beams. *Journal of Sound and Vibration*, 289(4):908–937, 2006.

[9] Jared Lee Black, Chiang C Mei, and Michel Claude Gilbert Bray. Radiation and scattering of water waves by rigid bodies. *Journal of Fluid Mechanics*, 46(1):151–164, 1971.

[10] M. Brocchini. *Elementi di Idraulica*. 2010.

[11] F. Buriani and E. Renzi. Hydrodynamics of a flexible piezoelectric wave energy harvester moored on a breakwater. *EWTEC*, 2017.

[12] PG Chamberlain and D Porter. Scattering and near-trapping of water waves by axisymmetric topography. *Journal of Fluid Mechanics*, 388:335–354, 1999.

[13] WJ Choi, Yongbae Jeon, J-H Jeong, Rajendra Sood, and Sang-Gook Kim. Energy harvesting mems device based on thin film piezoelectric cantilevers. *Journal of Electroceramics*, 17(2-4):543–548, 2006.

[14] João Cruz. *Ocean wave energy: current status and future prespectives*. Springer Science & Business Media, 2007.

[15] Adrian de Andres, Andy MacGillivray, Owain Roberts, Raul Guanche, and Henry Jeffrey. Beyond lcoe: A study of ocean energy technology development and deployment attractiveness. *Sustainable Energy Technologies and Assessments*, 19:1–16, 2017.

[16] Olivier Doaré and Sébastien Michelin. Piezoelectric coupling in energy-harvesting fluttering flexible plates: linear stability analysis and conversion efficiency. *Journal of Fluids and Structures*, 27(8):1357–1375, 2011.

[17] A. Erturk and D.J. Inman. *Piezoelectric Energy Harvesting*. Wiley, 2011.

[18] EUCommission. Set plan – declaration of intent on strategic targets in the context of an initiative for global leadership in ocean energy. 2016.

[19] Kester Gunn and Clym Stock-Williams. Quantifying the global wave power resource. *Renewable Energy*, 44:296–304, 2012.

[20] Robert E Harris, Lars Johanning, and Julian Wolfram. Mooring systems for wave energy converters: A review of design issues and choices. In *3rd international conference on marine renewable energy, Blyth, UK*, pages 180–189, 2004.

[21] M King Hubbert et al. Nuclear energy and the fossil fuel. In *Drilling and production practice*. American Petroleum Institute, 1956.

[22] Abdulrahman Jbaily and Ronald W Yeung. Piezoelectric devices for ocean energy: a brief survey. *Journal of Ocean Engineering and Marine Energy*, 1(1):101–118, 2015.

[23] YB Jeon, R Sood, J-H Jeong, and S-G Kim. Mems power generator with transverse mode thin film pzt. *Sensors and Actuators A: Physical*, 122(1):16–22, 2005.

[24] Mridula Kanoria, DP Dolai, and BN Mandal. Water-wave scattering by thick vertical barriers. *Journal of engineering mathematics*, 35(4):361–384, 1999.

[25] Christopher M Linton and Philip McIver. *Handbook of mathematical techniques for wave/structure interactions*. CRC Press, 2001.

[26] Lucia Margheritini, Diego Vicinanza, and Peter Frigaard. Ssg wave energy converter: Design, reliability and hydraulic performance of an innovative overtopping device. *Renewable Energy*, 34(5):1371–1380, 2009.

[27] Chiang C Mei, Michael Stiassnie, and Dick K-P Yue. *Theory and Applications of Ocean Surface Waves: Linear aspects*, volume 23. World Scientific, 2005.

[28] Mehmet Melikoglu. Current status and future of ocean energy sources: A global review. *Ocean Engineering*, 148:563–573, 2018.

[29] Michael H Meylan and Malte A Peter. Water-wave scattering by submerged elastic plates. *The Quarterly Journal of Mechanics & Applied Mathematics*, 62(3):321–344, 2009.

[30] S. Michele, P. Sammarco, M. d'Errico, E. Renzi, A. Abdolali, G. Bellotti, and F. Dias. Flap gate farm: From venice lagoon defense to resonating wave energy production. part 2: Synchronous response to incident waves in open sea. *Applied Ocean Research*, 52:43 – 61, 2015.

[31] Sébastien Michelin and Olivier Doaré. Energy harvesting efficiency of piezoelectric flags in axial flows. *Journal of Fluid Mechanics*, 714:489–504, 2013.

[32] Hidemi MUTSUDA, Kenta KAWAKAMI, Masato HIRATA, Yasuaki DOI, Yoshikazu TANAKA, and Daisuke YANAGIHARA. Study on wave power

generator using flexible piezoelectric device. *Journal of Japan Society of Civil Engineers, Ser. B2 (Coastal Engineering)*, 66(1):1281–1285, 2010.

[33] JN Newman. Wave effects on deformable bodies. *Applied ocean research*, 16(1):47–59, 1994.

[34] IEEE Standard on Piezoelectricity. *Standards Committee of the IEEE Ultrasonics, Ferroelectrics, and Frequency Control Society*, IEEE, New York, 1987.

[35] Arthur Pecher and Jens Peter Kofoed. *Handbook of Ocean Wave Energy*. Springer, 2017.

[36] Andrei D Polyanin and Alexander V Manzhirov. *Handbook of integral equations*. CRC press, 1998.

[37] William H Press, Saul A Teukolsky, William T Vetterling, and Brian P Flannery. *Numerical recipes 3rd edition: The art of scientific computing*. Cambridge university press, 2007.

[38] Junuthula Narasimha Reddy. *Theory and analysis of elastic plates and shells*. CRC press, 2006.

[39] E. Renzi and F. Dias. Hydrodynamics of the oscillating wave surge converter in the open ocean. *European Journal of Mechanics - B/Fluids*, 41:1 – 10, 2013.

[40] Emiliano Renzi. Hydroelectromechanical modelling of a piezoelectric wave energy converter. In *Proc. R. Soc. A*, volume 472, page 20160715. The Royal Society, 2016.

[41] Emiliano Renzi and F. Dias. Resonant behaviour of an oscillating wave energy converter in a channel. *Journal of Fluid Mechanics*, 701:482–510, 2012.

[42] Matthew N.O. Sadiku. *Elements of electromagnetics*. Oxford university press, 2018.

[43] Dripta Sarkar, Emiliano Renzi, and Frederic Dias. Effect of a straight coast on the hydrodynamics and performance of the oscillating wave surge converter. *Ocean Engineering*, 105:25 – 32, 2015.

[44] Yoshikazu Tanaka, Takuya Oko, Hidemi Mutsuda, Rupesh Patel, Stewart McWilliam, Atanas A Popov, et al. An experimental study of wave power generation using flexible piezoelectric device. In *The Twenty-fourth International Ocean and Polar Engineering Conference*. International Society of Offshore and Polar Engineers, 2014.

[45] CD Wang, MH Meylan, and R Porter. The linear-wave response of a periodic array of floating elastic plates. *Journal of Engineering Mathematics*, 57(1):23–40, 2007.

[46] Jinmei Wang and Ke Wang. Multi-scale method for ill-conditioned linear systems. In *IOP Conference Series: Materials Science and Engineering*, volume 242, page 012100. IOP Publishing, 2017.

[47] CB Williams and Rob B Yates. Analysis of a micro-electric generator for microsystems. *sensors and actuators A: Physical*, 52(1-3):8–11, 1996.

[48] Nan Wu, Quan Wang, and XiangDong Xie. Ocean wave energy harvesting with a piezoelectric coupled buoy structure. *Applied Ocean Research*, 50:110 – 118, 2015.

[49] XD Xie, Q Wang, and N Wu. Energy harvesting from transverse ocean waves by a piezoelectric plate. *International Journal of Engineering Science*, 81:41–48, 2014.

[50] XD Xie, Q Wang, and N Wu. Potential of a piezoelectric energy harvester from sea waves. *Journal of Sound and Vibration*, 333(5):1421–1429, 2014.

[51] YH Zheng, YM Shen, and J Tang. Radiation and diffraction of linear water waves by an infinitely long submerged rectangular structure parallel to a vertical wall. *Ocean engineering*, 34(1):69–82, 2007.